Winter 12-15-2014

Tuning Electronic Correlation with Pressure

Gilberto Fernandes Lopes Fabbris
Washington University in St. Louis

WASHINGTON UNIVERSITY IN ST. LOUIS

Department of Physics

Dissertation Examination Committee:

James S. Schilling, Chair

Daniel Haskel, Co-Chair

Parag Banerjee

Erik Henriksen

Richard Loomis

Alexander Seidel

Tuning Electronic Correlation with Pressure

by

Gilberto Fernandes Lopes Fabbris

A dissertation presented to the

Graduate School of Arts and Sciences

of Washington University in

partial fulfillment of the

requirements for the degree

of Doctor of Philosophy

December 2014

St. Louis, Missouri

Contents

List of Figures

List of Tables

Acknowledgments

Financial support for the work contained in this dissertation was provided by the Advanced Photon Source, a U.S. Department of Energy (DOE) Office of Science User Facility operated for the DOE Office of Science by Argonne National Laboratory under Contract No. DE-AC02-06CH11357, by the National Science Foundation through grant DMR-11047402, and by the Carnagie/DOE Alliance Center (CDAC) through NNSA/DOE grant No. DE-FC52-08NA28554.

The work presented in this dissertation was only possible due to the invaluable help of several people. I would like to particularly thank:

Dr. Daniel Haskel, my graduate advisor, for his constant work on my development as a scientist, and his extreme patience over our scientific discussions. His knowledge and guidance were fundamental to the development of this dissertation. The late night calls to the beamline during experiments will certainly be missed.

Prof. James Schilling, my graduate co-advisor, for his unwavering support and guidance. I have acquired invaluable knowledge and experience during my experiments at the Washington University in St. Louis.

Dr. Wenli Bi and Dr. Narcizo Marques de Souza-Neto for their encouragement, and for guiding my first steps in high pressure research.

Dr. Markus Hücker for his vital help in the work on $La_{1.875}Ba_{0.125}CuO_4$.

The members of the Magnetic Materials Group at the Advanced Photon Source (APS), Argonne National Laboratory (ANL), for their support and discussions. Especially to Dave Gagliano and Mike McDowell for their prompt technical assistance whenever needed.

The past and current members of Prof. Schilling's group – Neda Foroozani, Narelle Hillier, Vikas Soni, Jing Song, and Matt Ferguson, for the discussions and support. In particular Jinhyuk Lim for his vital help in many of the experiments in this dissertation.

Dr. Sergey Tkachev from GSECARS at the APS, ANL, for his support on the loading of gas pressure media into the diamond anvil cells.

The group members of the HPCAT at the APS, ANL, for their support in many of the experiments of this dissertation. In particular Dr. Changyong Park, Dr. Dmitry Popov, and Curtis Kenney-Benson, for their technical support.

Dr. Anup Gangopadhyay for his support in preparing the Y(Gd) and Y(Tb) alloys.

All my friends in St. Louis for the many happy moments.

Frankie, Jessie, and Dustin, for their encouragement, support, and friendship.

Larissa and Zé for their support, patience, and help in many of the experiments in this dissertation.

My girlfriend Vrinda, for her love, constant support, and encouragement through even the most stressful times.

My parents Carlos and Marina, and my brother Eduardo, for the many years of permanent support, love, happiness. This achievement is primarily the result of their permanent investment on my education.

ABSTRACT OF THE DISSERTATION

Tuning Electronic Correlation with Pressure

by

Gilberto Fernandes Lopes Fabbris

Doctor of Philosophy in Physics

Washington University in St. Louis, 2014

Professor James S. Schilling, Chair

Professor Daniel Haskel, Co-Chair

Strongly correlated electron systems display some of the most exotic ground states in condensed matter. In this thesis high pressure is used to tune the degree of electron correlations in systems of current interest. Their electronic and structural properties were investigated at high pressure using x-ray spectroscopy and scattering as well as transport techniques in a diamond anvil cell. The interplay between short- and long-range structural order, one-dimensional charge ordering, and superconductivity was studied in $La_{1.875}Ba_{0.125}CuO_4$. At ambient pressure, this material displays charge ordering at the onset of a low temperature structural phase transition, resulting in strong suppression of superconductivity. The electronic ordering is shown here to be tightly coupled to short-range, rather than long-range, structural order. It is argued that persistence of charge order on a very short length scale is responsible for the marginal enhancement of superconductivity under pressure, being evidence of competing electronic correlations. The lanthanides Gd and Tb display an atomic-like partially filled 4*f* level at ambient pressure. Here, extreme pressure was used in an attempt to delocalize these 4*f* states. Instability in Tb's $4f^8$ level emerges through 4*f*-conduction band hybridization, triggering a Kondo effect in the Y(Tb) alloy. In contrast, the half-filled $4f^7$ level in Gd remains stable to at least 120 GPa. Tb

appears to become a strongly correlated Kondo lattice at high pressure, the properties of which are of great interest. Alkali metals display unexpected properties at high pressure which are suggested to be due to enhanced electronic correlation of the once nearly-free conduction electrons. In this thesis, the mechanisms leading to the low symmetry phases observed at high pressure in K, Rb, and Cs were investigated. These phases are suggested to develop from the pressure-induced localization of the conduction band, which triggers a Peierls-like distortion. Furthermore, stripe-like charge ordering is theoretically observed in Cs at high pressure, in close resemblance to $La_{1.875}Ba_{0.125}CuO_4$, including proximity of charge order to superconductivity.

Chapter 1

Introduction

The pressing demand for technological innovations is particularly aimed at the design of novel materials to optimize desired properties. The primary step in this process is the basic physical understanding of the phenomena of interest. For instance, the discovery of high-T_c superconductivity in 1986 led to a tremendous rush towards potential applications of a room temperature superconductor that, so far, has failed to materialize, at least in part due to the lack of understanding on how such high-T_c occurs [1]. Another remarkable example of the impact of fundamental discoveries in technology is the mere ~ 15 years span between the discovery of giant magneto-resistance [2,3] to its widespread use in computer hard drives.

Material properties are generally determined by electronic interactions. In an isolated atom, the electron state can be found by solving the Schrödinger equation (or Dirac equation for heavy elements). While for a single electron atom this equation can be analytically solved [4], the inclusion of multiple electrons leads to complex electron-electron interactions. This many-electron system can be approximately solved using the Hartree-Fock method, by converting the system into a single-electron problem submitted to an all-electron potential that is self consistently solved [5].

When isolated atoms are put into a condensed matter form the inner states do not interact with the neighbors, preserving their atomic-like behavior, and being well described by the Hartree-Fock formalism. While these inner states display filled orbitals, the semi-filled 4*f* and 5*f* states of lanthanides and heavy actinides also show strongly localized character, often being well described as atomic orbitals [6].

On the other hand, the outermost atomic electrons interact with neighboring atoms forming the valence band and losing their atomic character. The limit in which the outer electrons are mostly decoupled from the atomic cores is described by the nearly free electron model [7,8]. This model assumes that valence electrons weakly interact with the positive atomic cores and among themselves. Remarkably, this simple model found its real life realization in the alkali metals, in which Coulomb interaction between the positive core and the lone *s* valence electron is heavily shielded by the remaining atomic electrons. The same concept of weak electron-electron correlation is successfully applied to density functional theory (DFT) [5]. Here, the problem of many interacting electrons is solved by describing the collection of electrons in terms of its density [5]. Within the Kohn-Sham ansatz, the multi-electron problem can be turned into a one particle equivalent by writing every energy contribution in terms of electron density [9]. However, correlation between electrons cannot be exactly written as a function of electron density [5], therefore these are approximated in first (local density approximation – LDA) or second (generalized gradient approximation – GGA) order expansion. Despite difficulties, DFT is a widely used and very successful method to study the electronic ground state of materials.

Electrons situated between the atomic- and band-like regimes are studied in the strongly correlated electron field [10,11]. The great interest in this area comes from the many exotic properties displayed by materials in this regime, such as the unexpected electronic ground states displayed in the original high-T_c superconductor family $La_{2-x}Ba_xCuO_4$ [12,13]. In this thesis pressure was used to cleanly manipulate systems across strongly correlated electron regimes, while following their electronic and structural properties.

The high-T_c cuprate $La_{1.875}Ba_{0.125}CuO_4$ displays a yet poorly understood interplay between superconductivity and charge/spin ordering (stripe ordering) [13–16]. Pressure was used to tune

the balance between these ground states, while investigating the corresponding effect in the short (~5 Å) and intermediate (~100 Å) range structural and electronic order, using single crystal x-ray absorption fine structure and diffraction techniques [17]. In another set of experiments, pressure was used in an attempt to push the strongly localized 4*f* state in heavy lanthanides Gd and Tb away from its ambient pressure atomic-like character [18]. X-ray absorption near edge structure, x-ray emission, and the superconducting T_c pressure dependence in Y(Gd) and Y(Tb) alloys were used to monitor their electronic structure as these lanthanides were pushed across the abrupt atomic volume reduction (volume collapse transition) observed at high-pressure. Finally, the electronic structure of the heavy alkalis K, Rb and Cs was investigated. High-pressure is known to drive these "simple" metals into highly complicated states, displaying much enhanced resistivity [19–21] and remarkably low symmetry phases [22]. Pressure is argued to strongly increase electronic correlation by confining the conduction electrons to much reduced volumes [23–25]. Therefore the emergence of electronic correlations was investigated in these alkalis through x-ray absorption fine structure and x-ray diffraction measurements coupled to *ab initio* calculations.

The remaining of this thesis is organized as follows: in Chapter 2 the current knowledge on the three scientific cases listed above is expanded. Chapter 3 contains information about the experimental methods used, including details on the experiments performed. In Chapter 4, the results are presented and discussed. Finally, Chapter 5 contains a summary of the results obtained.

Chapter 2

Strongly Correlated Electron Systems

2.1 $La_{2-x}Ba_xCuO_4$

Superconductivity was discovered over 100 years ago [26–28], but still challenges scientists [1,29–34]. The first successful microscopic theory of superconductivity, by Bardeen-Cooper-Schrieffer (BCS) [35–37], was proposed only after 46 years of its discovery. In this model, superconductivity is described as an electronic superfluid formed by electron pairs (Cooper pairs). However, achieving electron-electron bonding is not trivial as the strong Coulomb repulsion tends to dominate their interaction. In the BCS model electron-phonon coupling is suggested to enable electron pairing. An electron travelling throughout the lattice will attract nearby ionic cores through electrostatic interaction. The heavy cores are much slower than the electron, thus as the later moves away, a positive local charge is formed, which in turn attracts a second nearby electron, effectively forming the electron-electron bound state. The BCS theory has been widely successful in explaining the superconducting properties of many materials [38]. Particularly, the suppression of the superconducting temperature (T_c) by an external magnetic field is explained by the energy cost of expelling the magnetic field from inside the sample (Meissner effect).

One of the first signs that BCS may not be a complete model for superconductivity emerged in the end of the 1970's with the discovery of the so-called heavy-fermion superconductors [39–41]. These materials are poor conductors with magnetically ordered phases arising in close proximity to superconductivity, thus challenging some of the basic premises of the BCS model.

However, the low transition temperature observed in this family (T_c < 3 K) led to limited interest on their properties. In 1986 superconductivity near 30 K was discovered by Bednorz and Müller in the Ba-doped $La_{2-x}Ba_xCuO_{4-y}$ family [42], a remarkable discovery considering that such high T_c occurs in a material whose undoped (parent) compound (La_2CuO_4) is an antiferromagnetic insulator. This discovery triggered an intensive effort towards studying Cu-based superconductors (cuprates) [34,43]; within a year the YBaCuO family was discovered with T_c above liquid nitrogen temperatures [44]. Despite the tremendous enthusiasm, the current transition temperature record, established 21 years ago in mercury-based cuprates, is "only" 153 K [45], being very far from the desired room temperature superconductor. It is widely accepted that the typical BCS, electron-phonon coupling, picture is unable to explain high-T_c superconductivity in cuprates [1,34]. Furthermore, in 2008 high-T_c superconductivity was discovered in Fe-based compounds which display many similarities to the cuprates, including the proximity to magnetic order [46].

After 28 years, the mechanism for superconductivity in cuprates is still a matter of intense debate [33,47–55]. This state emerges via electron- or hole-doping of a parent antiferromagnetic insulating material, as charge doping suppresses Cu's magnetic ordering and adds mobile carriers. The proximity between superconductivity and magnetic ordering triggered suggestions that antiferromagnetic fluctuations may act as the electron pairing mechanism [1,56,57]. In fact, stripe-like charge and spin order in the CuO_2 plane has been recently discovered in many cuprates (further discussed in next section), indicating that these may be a universal feature of high-T_c superconductors [49,54,58,59]. Understanding the relationship between these coexisting electronic ground states is argued to be of major importance in comprehending high-T_c superconductivity [1,60].

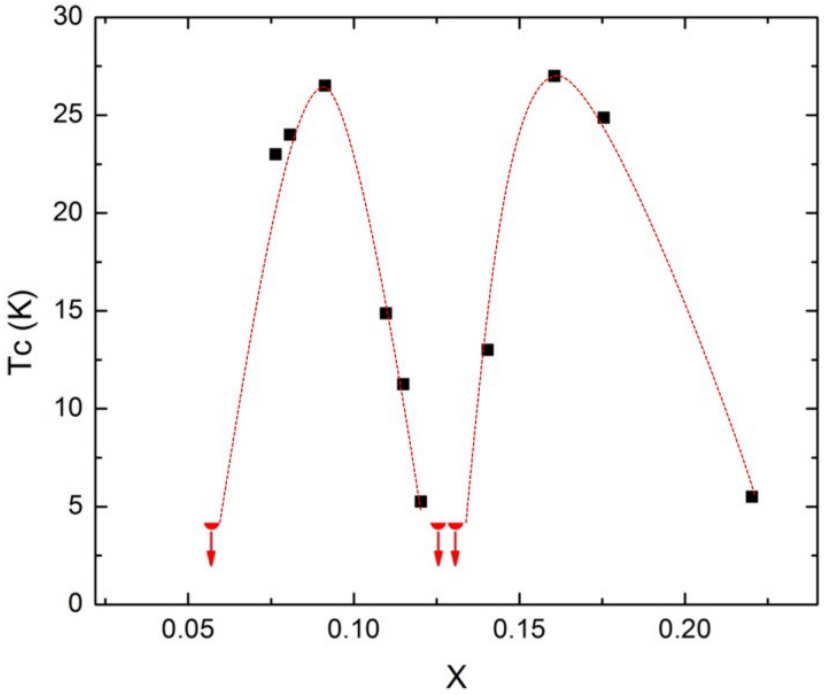

Figure 2.1: Superconducting transition temperature as a function of doping in $La_{2-x}Ba_xCuO_4$. Data extracted from Ref. [61].

2.1.1 Superconductivity, Structure and Stripes

Shortly after the discovery of high-T_c superconductivity, a systematic study of the superconducting transition of $La_{2-x}Ba_xCuO_4$ (LBCO) was performed by Moodenbaugh *et al.* [62]. The behavior of T_c above and below x~1/8 appears to indicate that a maximum should occur at x = 1/8; however, a large suppression is observed instead (Fig. 2.1).

A hint into understanding this exotic suppression comes from the structures adopted by the x=1/8 member of this family ($LBCO_{1/8}$) as a function of temperature, which are depicted in Fig. 2.2. These structures consist of CuO_2 and La(Ba)O layers, with the Cu atoms positioned inside a CuO_6 octahedra [48]. At room temperature, the CuO_2 planes are flat on average, yielding the high-temperature tetragonal (HTT) phase. At T = 235 K, the octahedra tilt around the [110]

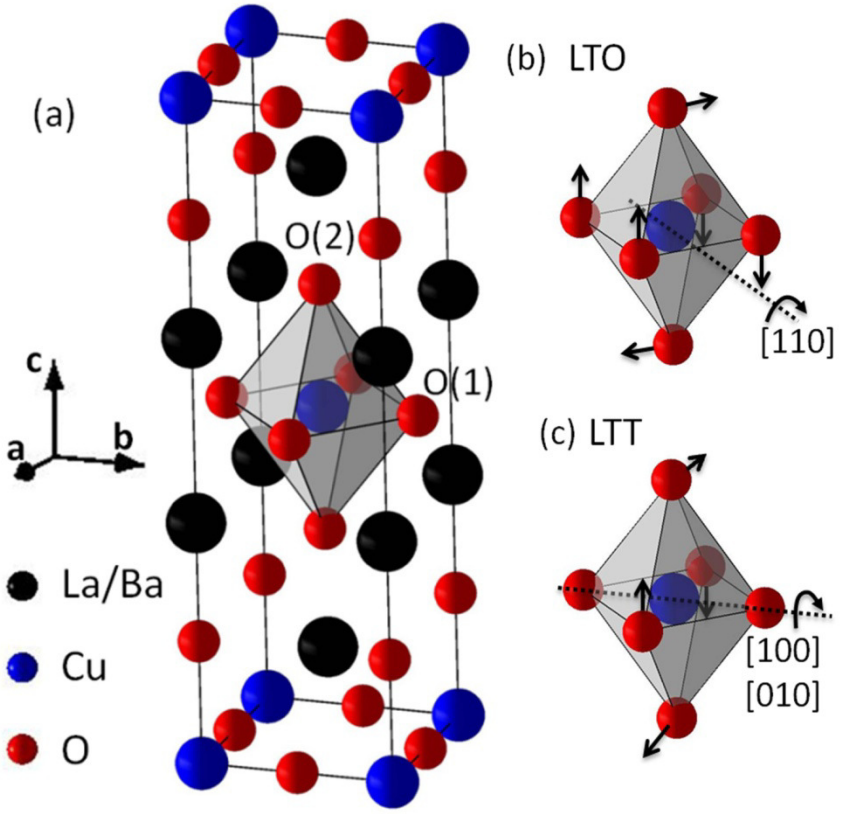

Figure 2.2: Structures displayed by $La_{2-x}Ba_xCuO_4$ [48]. (a) depicts the HTT phase unit cell. (b) and (c) shows the CuO_6 tilts that lead to the LTO and LTT phases respectively.

direction, buckling the all Cu-O-Cu bonds in the CuO_2 planes, and leading to a low temperature orthorhombic (LTO) phase. Finally, at T = 54 K, the octahedra tilt switches to the [100] direction, buckling half of the Cu-O-Cu bonds, and leading to the low temperature tetragonal phase (LTT). The LTO and LTT distortions result in a 45° rotation of the unit cell [48]. In this thesis, all $LBCO_{1/8}$ Bragg peaks are assigned using the unrotated HTT basis.

Remarkably, this sequence of temperature induced transitions is not detected by local structure probes (~10-20 Å). Both pair distribution function and x-ray absorption fine structure measurements observe persistent local LTT tilts above 54 K [63–65]. This apparent discrepancy is understood in terms of random buckling induced by thermal disorder [65]. Pickett *et al.* [66]

demonstrated that the LTT tilts correspond to a shallow minimum in the energy landscape, with the LTO and HTT average structures occurring due to thermally activated hopping between local minima.

Since the large Ba ion tends to destabilize the structure, the growth of good single crystal LBCO has only been achieved recently [67]. Similar T_c suppression and phase transitions are realized in the $La_{2-x-y}Sr_xRE_yCuO_4$ family (RE = rare earth), where Sr^{+2} is responsible for hole doping while RE^{+3} stabilizes the LTT structure [14,68]. Studying single crystal $La_{1.48}Sr_{0.12}Nd_{0.4}CuO_4$, Tranquada *et al.* demonstrated that charge (CO) and spin order (SO) emerged within the CuO_2 planes at low temperature concomitantly with the LTO-LTT phase transition [14]. This ordering occurs in the form of one dimensional charge/spin stripes along the unbuckled Cu-O-Cu bonds in the LTT phase (Fig. 2.3). The holes doped within the La(Ba)O plane move into the CuO_2 plane triggering a competition between kinetic energy, that is

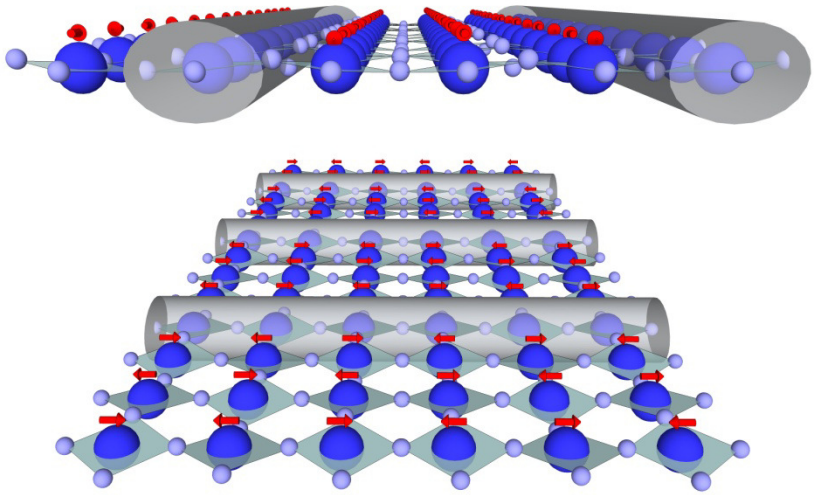

Figure 2.3: Stripe ordering in $LBCO_{1/8}$. Two consecutive CuO_2 planes are displayed. The Cu/O atoms are displayed in dark/light blue. Red arrows represent the direction of the local spin moment, while the gray cylinders represent the charge order.

minimized by delocalizing the hole, and exchange energy, that prefers local Cu moments to enable magnetic ordering. At the particular 1/8 doping, the balance between these competing interactions results in the segregation of charge stripes and spin stripes [14]. That the emergence of this electronic ordering matches the LTT onset does not seem to be an accident [69]. In fact, these stripes follow the direction of the unbuckled in plane Cu-O-Cu bonds, including the 90° rotation observed between consecutive planes (Fig. 2.3).

While the correlation between suppressed T_c and static stripe order points to a competition between these two electronic states, there have been many suggestions that dynamical stripes actually drive superconductivity in cuprates [1,56]. In fact, detailed transport measurements in $LBCO_{1/8}$ display a remarkable drop in resistivity within the *ab* plane at much higher temperatures than the onset of bulk superconductivity, indicating that even static stripes may induce 2D superconductivity [15,16]. The suppression of T_c is then argued to be due to reduced Josephson coupling along the *c* axis due to the 90° stripe rotation [16]. In fact the resistivity along this axis is enhanced at low temperature [15].

2.1.2 High-Pressure Phase Diagram of $La_{1.875}Ba_{0.125}CuO_4$

High-pressure seems to be unable to significantly change the behavior of the superconducting temperature in the LBCO family. At a doping level slightly away from 1/8, approximately 2 GPa is sufficient to enhance the suppressed T_c to near optimal values (~33 K) [61,70] (Fig. 2.4 (a)). However at x=1/8, T_c slowly recovers, even at ~15 GPa it reaches only ~18 K [70].

In an attempt to understand this problem, the crystal structure and stripe-order of $LBCO_{1/8}$ was recently measured at high pressure by Hücker *et al.* using single crystal diffraction [70] (Fig. 2.4(b)). While pressure suppresses both LTO and LTT phases at ~1.7 GPa, charge order persists to the maximum pressure measured (2.7 GPa), implying that charge order is able to exist in

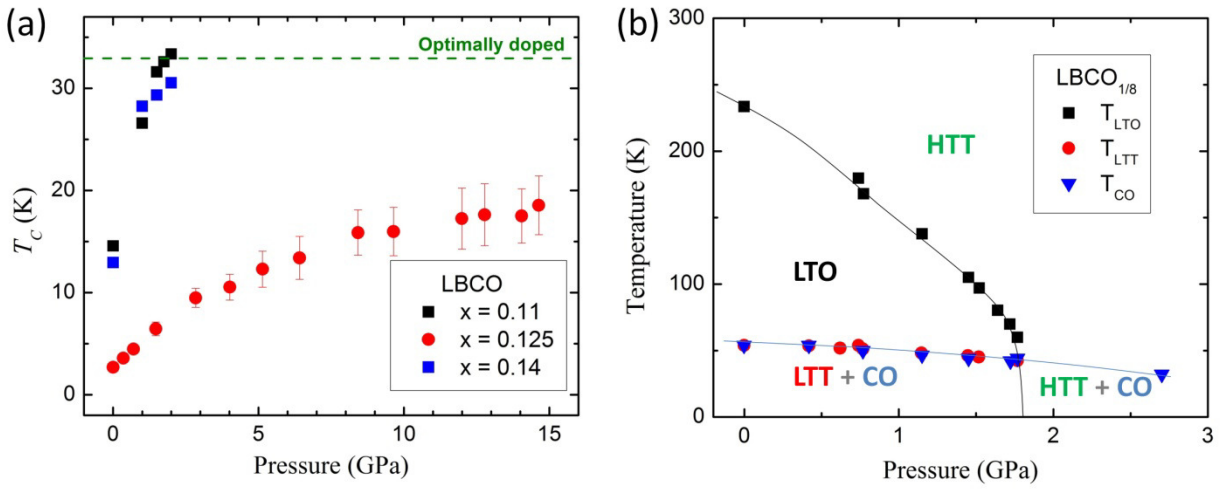

Figure 2.4: (a) Pressure dependence of T_c in LBCO around x = 1/8. Data extracted from [61,70]. (b) Phase diagram of $LBCO_{1/8}$. Data extracted from [70].

$LBCO_{1/8}$ without LTT order. Furthermore, no significant change in CO domains was observed; however, in this pressure range superconductivity is enhanced to only ~8 K, below the temperature used in that measurement (10 K).

Both stripe order and superconductivity display short correlation/coherence lengths (~100 Å [13] and ~10-20 Å, respectively) in $LBCO_{1/8}$. In fact, diffuse scattering was measured at the (1.5,1.5,2) peak, which is allowed in both LTO and LTT phases, indicating the presence of LTO or LTT domains with the same correlation length as CO within the high-pressure HTT phase [70]. This result, combined to the lack of correlation between the CO, superconductivity, and long range structure at high pressure (Fig. 2.4), indicates that the short range structure may be relevant in controlling the electronic ordering in $LBCO_{1/8}$.

In this thesis, the correlation between the structural and electronic order is investigated at the short and medium range scale. By using a combination of high-pressure single crystal extended x-ray absorption fine structure and x-ray diffraction techniques at low temperature, it will be

shown that the short range structure is in fact closely related to both electronic ground states observed in $LBCO_{1/8}$.

2.2 Lanthanides

The behavior of the semi-filled 4*f* shell in lanthanides is perhaps one of the most intriguing and thoroughly studied problems in the strongly correlated electron field [71,72]. The 4*f* wave function displays a narrow radial distribution lying very close to the atomic core (see Fig. 2.5). Such spatial confinement leads to a very large Coulomb repulsion between the electrons (> 3 eV) that splits the occupied and unoccupied 4*f* states, typically positioning the occupied levels well below the Fermi level (> 1 eV). The well defined electron orbits coupled to the sizable atomic number (Z) lead to a large spin-orbit coupling ($\propto Z^4$), that affects their ground state. The 4*f* level is then best described within a **L**.**S** coupling scheme, where **L** is the total angular momentum and **S** is the total spin. Consequently, their ground state can be determined by considering the total angular momentum $\mathbf{J} = \mathbf{L} + \mathbf{S}$ and Hund's rules. Crystal field interactions are typically much weaker due to screening by outer *spd* electrons, generally inducing only a small splitting of the $(2J + 1)$ degenerate states [73,74]. However, crystal fields are responsible for the single ion magnetic anisotropy in lanthanides [71], which is essential for the current permanent magnet technology, and it has been argued to be relevant for lighter lanthanides, leading to the lack of magnetic order in praseodymium above 1 K [75,76].

The conduction band of lanthanides at ambient pressure is dominated by *s* and *d* electrons, with a nominal $6s^2 5d^1$ occupation. Eu and Yb are exceptions, since they remain divalent ($4f^7$ and $4f^{14}$ respectively) in the elemental solid with $6s^2 5d^0$ occupation. The *lanthanide contraction* is the term used for the anomalously large reduction in atomic size observed across this series with increasing atomic number. It results from the larger nuclear charge being poorly screened by the

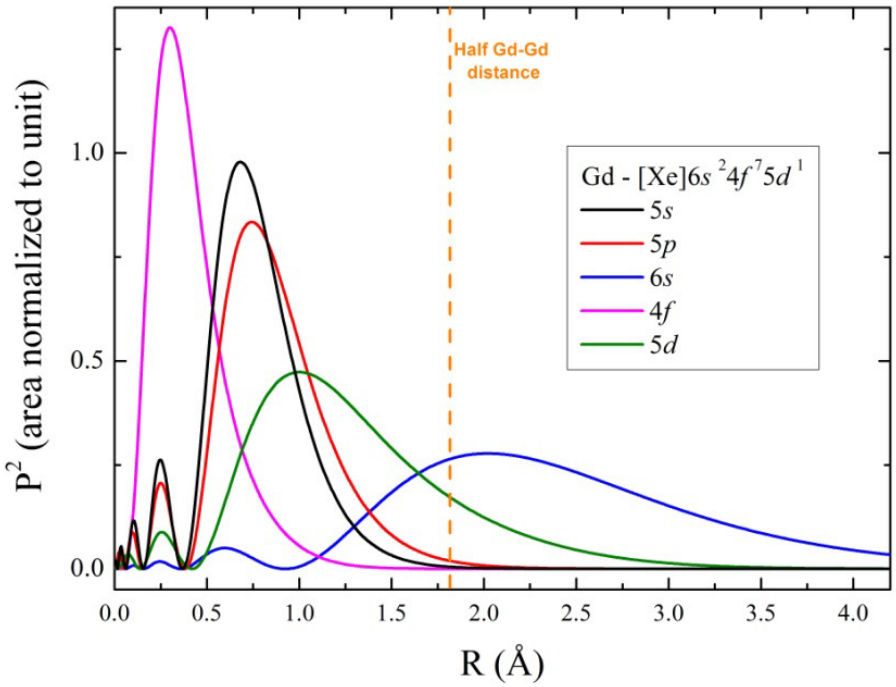

Figure 2.5: Radial distribution of atomic states in gadolinium. The orange dashed line marks half of the Gd-Gd distance at ambient pressure. Data extracted from Refs. [77,78].

extra 4*f* electron which reduces the radial size of the 6*s* level, leading to a further reduction of the atomic size. Such 6*s* level contraction is also manifested in the lowering of its energy position with respect to the Fermi level. As shown by Duthie and Pettifor [79], the observed phases for the different lanthanides can be explained by the differing number of 5*d* electrons. The lower 6*s* energy position with increasing 4*f* atomic number leads to a reduced 6*s* to 5*d* overlap, hence reduced charge transfer. Thus the heavy lanthanides (Gd to Lu) have less 5*d* electrons and order in the hcp structure; moving towards the lighter lanthanides the increased 5*d* occupation leads to the stabilization of α-Sm, dhcp and fcc phases. Compression also leads to 6*s*→5*d* charge transfer and a very similar set of phase transitions is observed in most lanthanides [80].

At ambient pressure, the nearest neighbor distance in lanthanides is larger than the 4*f* radial extent, preventing any direct 4*f*-4*f* interaction (half neighbor distance ≈ 1.8 Å, see Fig. 2.5).

Nevertheless, a strong exchange interaction occurs locally between the 4*f* level and the conduction band. In fact, an indirect 4*f*-4*f* coupling known as RKKY (after Ruderman, Kittel, Kasuya, Yosida) [81–83] is achieved through a second order interaction, where the local 4*f* moment spin polarizes the conduction band, which in turn interacts with the next 4*f* neighbor, leading to long range magnetic order.

The 4*f*-conduction band exchange interaction is strongly influenced by their hybridization. Without 4*f*-conduction electron mixing their wave functions are orthogonal and the exchange integral is positive, leading to their ferromagnetic coupling [73]. On the other hand, as Kondo first described in 1962 [84], when the localized magnetic moment hybridizes with the conduction band, the electronic wave functions mix and become non orthogonal, leading to a negative exchange. Such negative exchange was used by Kondo to explain the resistance minimum observed at low temperatures in paramagnetic metals doped with magnetic impurities [85]. Qualitatively, at low temperatures the Kondo interaction creates a cloud of antiferromagnetically spin polarized electrons around the magnetic impurity. This process can be understood as an effective localization of the conduction band that increases the resistivity at low temperatures. The Kondo model for magnetic impurities was heavily studied in the 60's and 70's and it is a well established model [86]. Recent advances in atomic microscopy probes have re-attracted attention to the Kondo problem, especially regarding the spatial extent of the interaction [87].

The Kondo model has since been expanded into the concept of a Kondo lattice as introduced by Doniach [88]. The Kondo lattice consists of a system where Kondo interaction happens at each lattice point. Such a system displays strongly correlated states that hybridizes with the conduction band. This electronic system lies somewhere in between an atomic-like and free-electron-like models and is one of the most challenging problems in condensed matter physics,

thus the properties of the Kondo lattice are still a matter of theoretical and experimental investigations [89–91]. The competition between magnetic ordering and Kondo screening, as the Kondo temperature (T_K, see below) is increased, is of particular interest. The magnetic order (T_o) scales with the 4*f*-conduction band exchange integral (I) [82] as

$$T_0 \propto N(E_F)|I|^2 \tag{2.1}$$

where $N(E_F)$ is the density of states at the Fermi level, while for the Kondo temperature (T_K) [92–94]

$$T_K \propto e^{-\frac{1}{N(E_F)|I|}} \tag{2.2}$$

. Consequently a quantum phase transition from magnetic-ordered to Kondo-screened phases is expected with increasing $|I|$ [88,90]. Magnetic fluctuations in proximity to quantum phase transitions are believed to be the source of exotic phenomena such as high-T_c superconductivity [29,95] and topological insulators [96,97]; in particular, the Kondo lattice theory is believed to be related to the behavior of heavy fermions [98] and shown to be capable of promoting superconductivity [99,100].

In the heavy lanthanides, the 4*f* moment is stable at ambient pressure, and robust RKKY-type magnetic ordering is observed, with no signs of Kondo interactions. However, the breakdown of such stability is expected to take place as the atoms are closely packed under extreme pressure. Our goal in this study was to probe the pressure dependence of such possible breakdown in gadolinium and terbium, by investigating the atomic volume discontinuity (volume collapse transition) observed in many lanthanides.

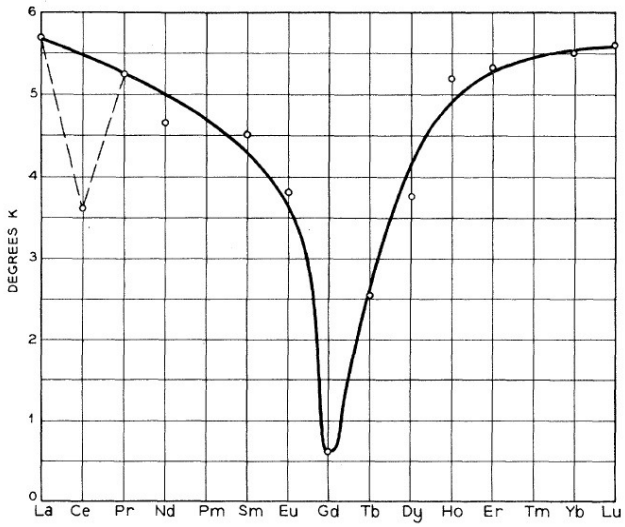

Figure 2.6: Superconducting temperature of La(1 at. % RE) alloys. Figure extracted from [101].

2.2.1 Investigating the 4*f*-Conduction Band Exchange Interaction

An effective method to study the nature of the 4*f*-conduction band exchange interaction is to alloy dilute amounts of the magnetic ion into a superconducting host. An early study by Matthias *et al.* [101] used lanthanum as a superconducting host alloyed with 1 at.% of each lanthanide. Superconductivity is suppressed in these alloys by the exchange interaction between the 4*f* level and the conduction band. In fact, when this exchange is positive, Abrikosov and Gor'kov (AG) developed universal functions to describe the T_c suppression in BCS-type superconductors [102,103]

$$\ln\left(T_c/T_{c0}\right) = \psi(1/2)\,\psi(1/2 + 0.14\alpha T_{c0}/T_c) \tag{2.3}$$

where ψ is the digamma function, T_c is the superconducting transition of the alloy, T_{c0} is the superconducting transition of the pure host, and α is given by

$$\alpha = 4\gamma n N(E_F) I^2 S(S+1)/k_b T_{c0} \tag{2.4}$$

where n is impurity concentration, k_b the Boltzmann constant, γ is the Euler's constant, and S the impurity spin. As seen in Fig. 2.6, the suppression of T_c strongly depends on impurity spin. In fact, expression 2.3 has been shown to nicely reproduce the doping dependence of $La_{1-x}Gd_xAl_2$ alloys [104], demonstrating a positive 4*f* – conduction band exchange interaction.

The one observed discrepancy is La(Ce), for which T_c is much lower than expected. In fact, the AG theory is unable to explain the Ce doping dependence of T_c [105]. This discrepancy occurs due to the covalent mixing between the 4*f* level and the conduction band in Ce, in a Kondo interaction picture. In fact, Müller-Hartmann and Zittartz (MHZ) [106–108] showed that the inclusion of Kondo interaction leads to the same expression 2.3, but with

$$\alpha = \frac{nS(S+1)}{0.56k_bN(E_F)T_{c0}\{[\ln(T/T_K)]^2+\pi^2S(S+1)\}} \tag{2.5}$$

where T_K is the Kondo temperature. The MHZ theory successfully describes the behavior of T_c in alloys with magnetic impurities that display Kondo interactions, including the remarkable re-entrant normal state observed in $La_{1-x}Ce_xAl_2$ alloys [109].

2.2.2 Cerium and the 4*f*-Driven Volume Collapse Models

Cerium's isostructural γ→α phase transition exhibits the largest (16%) and most thoroughly studied volume collapse of any lanthanide [110–112]. This volume collapse happens at ~0.7 GPa at room temperature [112], a pressure low enough to enable many different experimental tools. In particular, magnetic susceptibility measurements found a large (80%) and abrupt drop in magnetization across the transition [113], demonstrating that 4*f* electrons must be involved. This finding triggered a lot of interest on understanding the origin of this large volume collapse, which led to different proposed theories, some of which are outlined here (see Fig. 2.8):

a) Promotional model [114] – In this scenario, pressure moves the localized 4*f* level across the Fermi level, donating its electron to the conduction band. The loss of the 4*f*

electron increases the number of valence (binding) electrons, reducing the atomic size.

b) Mott model [115] – Here the pressure-induced reduction in atomic size leads to 4*f*-4*f* overlap which turns the localized state into a band. Such 4*f* band is formed across the Fermi level, adding binding energy to the system, and leading to the volume collapse.

c) Kondo model [116] – It is known that the Kondo temperature in Ce is largely dependent on its atomic volume, substantially increasing upon volume reduction [117]. Thus pressure enhances the covalent mixing between the 4*f* level and the conduction band. Such 4*f*-conduction band bond contributes to the binding energy of the system; it was shown that when the mixing reaches a critical value the volume collapse occurs.

To our knowledge these represent the most used models for cerium's volume collapse in the literature. However, recent results also point to the importance of lattice dynamics in Ce's volume collapse [118].

Despite the large body of experimental data, the origin of the volume collapse in cerium, hence the character of its 4*f* state at high pressure, is still under debate. The observation of near integral 4*f* occupation through many different experimental probes across this transition is inconsistent with the promotional model [115,119]. Thus, most of the still ongoing debate is centered on the Mott and Kondo models [118,120,121].

Perhaps the clearest evidence in favor of a Kondo-driven volume collapse in Ce comes from the deep minimum of T_c observed in La(Ce) alloys around 0.7 GPa (Fig. 2.7) [103], exactly the pressure of Ce's volume collapse [112]. The occurrence of this minimum is expected in a MHZ picture with increasing T_K, with the maximum suppression expected to occur at $T_K \sim 10T_{c0}$. In fact, the Kondo temperature in Ce is known to the volume dependent [117]. The recovery of T_c at pressures above the volume collapse is understood in terms of screening of the impurity moment due to the Kondo interaction. That the maximum suppression of T_c occurs around the volume

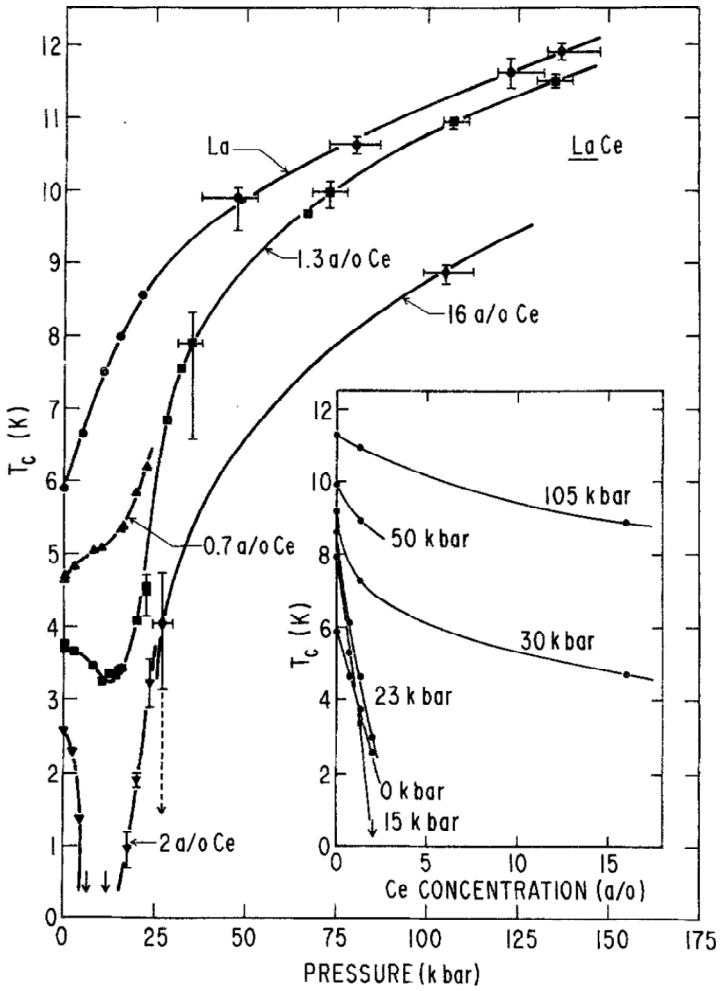

Figure 2.7: Pressure dependence of T_c in La(Ce) alloys. Figure extracted from [103].

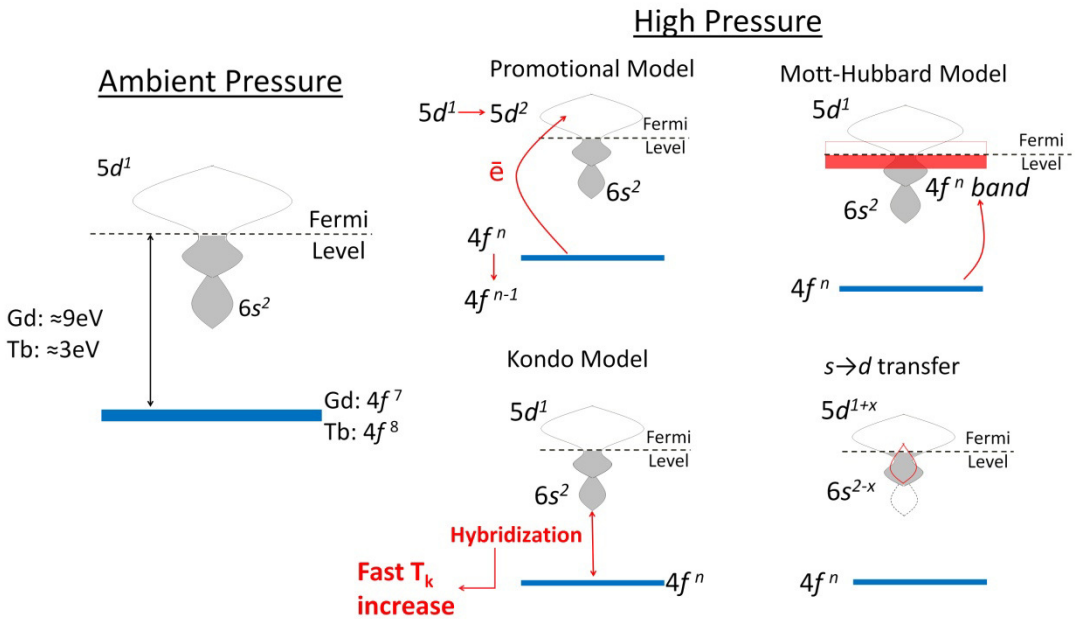

Figure 2.8: Pictorial representation of Gd and Tb electronic structure at ambient pressure and the proposed changes for each model.

collapse is strong evidence that this transition in Ce is Kondo driven [116].

2.2.3 Gadolinium, Terbium and the Volume Collapse in Yttrium

At ambient pressure, the 4*f* state of both gadolinium ($4f^7$ configuration, S = 7/2, L = 0, J = 7/2) and terbium ($4f^8$ configuration, S = 3, L = 3, J = 6) lie well below the Fermi level, ~ -9 eV and ~ -3 eV respectively [6]. The significant difference in 4*f* energy position for Gd and Tb is due to the added Coulomb repulsion arising from having two electrons occupying the same orbital in Tb (l = 3). Despite Tb's 4*f* lying closer to the Fermi level, in both metals the 4*f*-conduction band exchange integral is positive, and RKKY type magnetic order is observed.

Under pressure, both display the typical lanthanide series of structural phase transitions [122,123]: hcp → Sm-type → dhcp → dfcc, with Gd displaying an fcc phase between

dhcp and dfcc. This set of phase transitions is well explained by the pressure induced $s \rightarrow d$ transfer, as shown in Duthie and Pettifor's work [79]. For both Gd and Tb the dfcc phase is followed by a monoclinic structure at 59 GPa and 53 GPa, respectively [122,123]. A volume collapse of 5% happens across this transition for both metals.

While there had been no previous study on Tb's electronic structure across the volume collapse, Gd has been the target of x-ray spectroscopic studies [124,125]. X-ray absorption spectroscopy showed that no valence transition takes place across the volume collapse, and that $s \rightarrow d$ transfer is indeed active [124]. X-ray emission spectroscopy showed a continuous increase in the $4f^8$ component with pressure (~ 15 % of $4f^8$ at 113 GPa), and persistent local $4f$ level across the volume collapse [125]. These results indicate that the promotional and Mott models cannot account for Gd's volume collapse. Furthermore, the increased $4f^8$ hybridization was interpreted as evidence that this transition is Kondo driven [125].

Contrary to Ce, there is no clear evidence that the volume collapse in Gd and/or Tb is related to $4f$ interactions. Volume collapses are observed in several compounds that lack $4f$ electrons, such as the alkali metals (see section 4.3.1.4) [22], and the rare-earths Sc [126] and Y [127]. In fact, Y is known to have a very similar conduction band to the heavy lanthanides, and display the same set of pressure induced phase transitions, including the same volume collapsed phase. It is then important to consider that the volume collapse may be described by an "$s \rightarrow d$ transfer model", where a first order phase transition is simply driven by the increasing $5d$ occupation (Fig. 2.8).

As will be shown in this thesis, x-ray spectroscopy results show that, as for Gd [124,125], Tb's volume collapse cannot be explained by the promotional or Mott models. On the other hand, the behavior of T_c in Y(0.5 at.% Gd) and Y(0.5 at.% Tb) at high pressure indicate that

Kondo interaction is triggered across Tb's volume collapse, but not across Gd's. This result is understood in terms of the much more stable $4f^7$ level in Gd. It is suggested that Tb becomes a Kondo lattice above its volume collapse. The magnetic ordering in such exotic phase is currently being investigated [128].

2.3 Alkali metals

Alkali metals constitute the first column in the periodic table, displaying closed shell ionic cores with one extra *s* electron. In a solid, this lone *s* electron weakly interacts with the heavily shielded ionic core, leading to weak metallic bonds, low density, and a very broad (delocalized) conduction band at ambient pressure. This picture of the alkali metals was first suggested by Wigner and Seitz in 1933 within the so-called nearly free electron model (NFE) [7,8], in which the conduction electrons are treated as free electrons susceptible to a small periodic potential at the ionic position. Originally applied to sodium, this model has been extensively studied as an approximation to the electronic structure of metals, but the alkalis remain its best realization, as it has been very successful in describing their physical and chemical properties at ambient pressure [129].

2.3.1 Electronic Properties at High Pressure

High-pressure is expected to lead to the broadening of electronic bands, since as the atoms are forced closer together, the overlap of electronic wavefunctions increases, triggering a combination of Pauli exclusion principle and electron-electron Coulomb repulsion, that delocalizes the electronic state. Consequently, one would expect that pressure would render the alkalis even better metals, without fundamentally changing their properties.

Figure 2.9: Pictorial representation of the pressure-induced localization of conduction electrons in alkali metals.

This scenario was challenged by Neaton and Ashcroft [23]. They argued that while pressure strongly reduces the interatomic distances due to the weak metallic bonds, the ionic core is largely unperturbed. These cores are impenetrable to conduction electrons due to Coulomb repulsion and orthogonality of the wave functions. The experimentally accessible pressures (< 200 GPa) are sufficient to make the cores touch, forcing the conduction electrons to the interstitial sites (Fig. 2.9). Such electronic localization turns the alkalis into strongly correlated systems, significantly altering their electronic properties. In fact, marked deviation from NFE behavior is seen in the pressure dependence of plasmon excitations measured by inelastic x-ray scattering [130]. Furthermore, Li becomes a semiconductor in the range ~80-120 GPa [20,131] and Na turns into an insulator above ~200 GPa [21]. Although a resistivity increase has been observed in some high-pressure phases of Rb and Cs [132–136], the departure from the metallic state has not been seen in these alkalis. This is likely due to the emergence of *d* character in their conduction band at high pressure [137], which can penetrate the *sp* ionic cores more efficiently, and the more extended wavefunctions of the valence electrons for the heavier alkalis.

At ambient pressure Li is the only alkali able to superconduct due to their low density of states at the Fermi level which originates from their broad conduction band. Under pressure, only Cs is known to become a superconductor. Li's superconductivity increases rapidly for P > 20 GPa [138,139], reaching ~14 K at 30 GPa. There is evidence for reentrant superconductivity above the semiconducting phase (>120 GPa) [131]. While electron-phonon coupling within the Bardeen-Cooper-Schrieffer (BCS) theory is generally accepted to describe superconductivity in Li [140–142], it has recently been argued that plasmons may contribute to pairing [143]. Furthermore, recent isotope effect measurements seem to suggest a potentially more complex coupling scheme [144]. In Cs the superconducting transition temperature reaches only ~1.4 K at ~12-15 GPa [135,136], and is also postulated to emerge from conventional electron-phonon interaction [140]. However, while theoretical calculations can reasonably reproduce the pressure dependence of Li superconductivity, they fail to describe that of Cs [140]. Additionally, the same theoretical approach predicts superconducting phases in Na, K, and Rb which have not been experimentally observed [140,141,145–147]. Consequently, further understanding of the electronic structure is needed.

Finally, the pressure-enhanced DOS at the Fermi level in alkalis has been recently suggested to lead to a Stoner instability, thus the potential emergence of band ferromagnetism [148]. In fact, DFT calculations were used to search for possible ferromagnetic ground states in alkalis [148]. While no stable magnetic structures for Li and Na was found, Rb and Cs displayed magnetic phases close to stability, and a ferromagnetic ground state was predicted for K for ~17-22 GPa. Interestingly, the structures predicted to be magnetic are not found at room temperature.

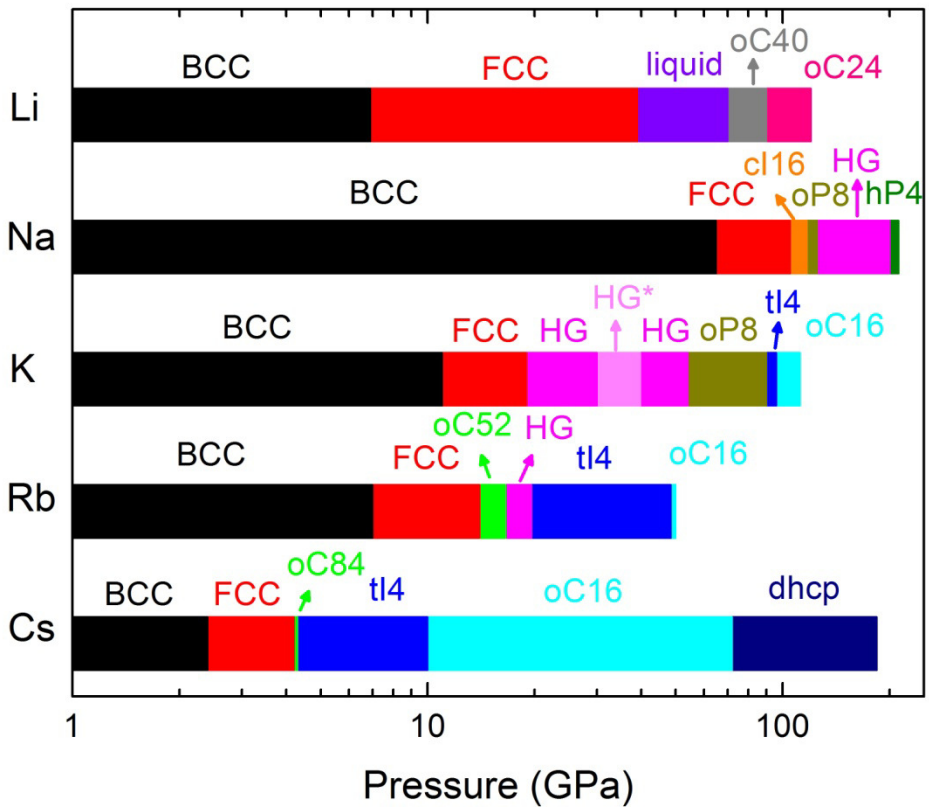

Figure 2.10: Phase transition of alkali metals at room temperature according to diffraction [22,149–160]. HG corresponds to the host/guest structure, in which two incommensurate structures are present. Note that resistivity data suggest that the melting curve of Li remains above room temperature in the ~30-60 GPa range [161].

2.3.2 High-Pressure Phase Transitions

The known phase transitions occurring at room temperature in the alkalis are displayed in Fig. 2.10. All alkalis order in the bcc phase at ambient pressure, and compression leads to the emergence of the fcc phase. The post-fcc phases are different for each alkali, but all exhibit remarkably low symmetry. Furthermore, the emergence of these low symmetry phases coincides with a strong reduction in their melting temperatures, indicating bond frustration; in Li, after

reaching ~ 520-550K around 10-15 GPa [159,161], the melting temperature displays a minima between 39 and 70 GPa, in the range of 200-310 K as seen by diffraction [159] and resistivity [161] respectively. Therefore, understanding the driving forces behind these remarkable transitions is of great interest [162–167].

Compression is known to shift the energy of different orbitals by different amounts. This effect is particularly obvious in the lanthanides, as discussed in section 2.2.3, where $6s \rightarrow 5d$ charge transfer explains the sequence of phases observed both within the series and at high pressure. Consequently, such electronic transfer has also been expected to occur in the alkalis, with emergent *p* character for Li and Na, and *d* character for K, Rb, and Cs. As for the lanthanides, the increase in the occupation of the more *pd* orbitals is expected to yield dense-packed structures in alkalis [168], contrary to the open structures observed in the alkalis.

The low symmetry, open structures of alkalis can be seen as a consequence of the balance between electronic kinetic energy and core–conduction electron interaction [23,25]. The core-electron shielding of the nucleus is very effective in alkalis since there is only one extra electron other than the noble gas electronic configuration. Consequently, even though the net ionic charge leads to a weak conduction electron–core attraction, the outer electrons shielding expels the conduction electrons from the core. At low density the cores occupy a small fraction of the metal's volume; hence the conduction electrons can efficiently avoid them. Compression dramatically changes this scenario. As the ionic cores are largely incompressible, they occupy an increasingly larger relative volume. As the cores start overlapping, the conduction electrons are pushed into the interstitial sites, thus forcing their localization. However, such electronic localization is very costly to the kinetic energy. This problem is then minimized by distorting the structure so that some ionic cores get closer, generating open pockets where the valence

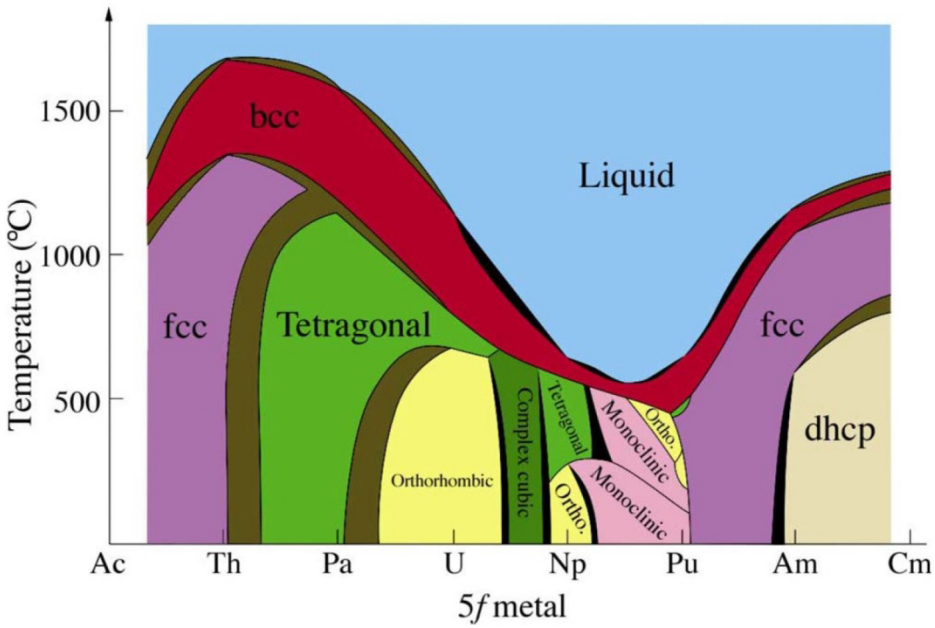

Figure 2.11: "Pseudobinary" phase diagram of actinide metals. Figure extracted from Ref. [169].

electrons reside. In particular, this process has been shown to lead to nearly full conduction band localization in Li [20,23] and Na [21,24], as evident by their semiconducting and insulating high-pressure state respectively.

An alternative view of the emergence of low symmetry phases is the so-called Fermi surface – Brillouin zone (FS-BZ) interaction [163,170–172]. In the FS-BZ process, as pressure drives the NFE spherical Fermi surface closer to the Brillouin zone, the electronic energy is minimized by adopting a structure in which the Fermi sphere filling of the Brillouin zone is maximized, as the electronic energy is lowered near a BZ boundary. This is generally possible by adopting very low symmetry phases, and it has been used in an attempt to explain some of the observed phases, such as phase III of Li (cI16 at low temperature [159]), Na, Rb, and Cs, and oC16 structure seen in K, Rb, and Cs [171]. However, it appears to fail at describing other phases such as the tI4, host/guest, oP8, and hP4 [167,172], where an unlikely transfer of an electron from the core to the

valence band would be needed. Furthermore, the FS-BZ model is particularly distinct by requiring preservation of a spherical Fermi surface at high-pressure, thus within this model, the conduction band nearly free electron behavior is preserved.

An interesting similarity occurs between the structural behaviors of alkalis under pressure to that in the actinide metals. In the actinide series a remarkable set of phases is observed (Fig. 2.11), with a melting temperature minimum occurring for materials displaying low symmetry phases. From heavier to lighter actinides, the phases transform from high-symmetry to low-symmetry, and then back to high-symmetry. The exact same behavior is seen in alkalis under compression [159,161,173,174] (Fig. 2.10). In actinides, this behavior has been postulated to emerge from a competition between Madelung and Peierls contribution [175]. In the later, electronic energy is gained by bringing the ionic cores closer, leading to the reduction in structural symmetry. This process opens a gap (or pseudo-gap) that increases the density of occupied states at lower energy at the expense of states at the Fermi level. Consequently, this process leads to enhanced electronic localization at the Fermi energy. In actinides, the degree of hybridization between the 5*f* states and the broad *spd* conduction band, as well as the width of the 5*f* states, is believed to dominate the strength of the Peierls contribution [175].

In this thesis the ground state properties in heavy alkalis are investigated at high pressure using a combination of experimental (x-ray absorption spectroscopy) and theoretical (DFT and real-space multiple-scattering) techniques. The phase transitions observed at room temperature are mostly reproduced at 10 K. The emergence of low symmetry phases is shown to be generally inconsistent with a FS-BZ mechanism, but the opening of a pseudo-gap point to an electronically driven transition. While the observed structural phases of K suggest the lack of the predicted magnetic ordering, a remarkable charge ordering is theoretically suggested to emerge in Cs at

high-pressures. Such charge order is remarkably similar to that observed in $La_{1.875}Ba_{0.125}CuO_4$, even occurring at the boundary of the observed superconductivity. The possible proximity of charge ordering and superconductivity in a pure elemental solid is an exciting possibility that needs to be experimentally verified.

Chapter 3

Methods

3.1 Diamond Anvil Cell

Diamond anvil cells (DAC) are today a widely used method to generate very high static pressure. In a DAC, pressure is generated by pressing the sample between two diamonds, the hardest material known. Since pressure depends on the inverse of the load, application of moderate forces (< 0.5 ton) generates pressures equivalent to those at the earth's core (~360 GPa). Despite the simple concept, the specific design of pressure cells depends largely on the experiment performed. While some of the general aspects of a DAC are discussed below, specific details for each experiment are described separately in subsequent sections. Further aspects of high-pressure methods can be found in many reviews and books on the subject (see for instance [176,177]).

All DACs used in this work are variations of the piston-cylinder design [177]. Pressure is increased by either tightening the screws connecting the cylinder and piston or by the use of a membrane driven by pressurized He gas. Membrane areas are typically a few cm^2, hence He pressure from commercial bottles is sufficient to generate the required forces. The use of membranes can be particularly advantageous in low temperature measurements, since pressure can be rather easily increased *in situ* by feeding He gas into the membrane through thin capillaries. Alternatively, a gear box can be used to mechanically tighten the screws in the cell at low temperature [177], however this typically increases the thermal mass inside the cryostat, resulting in less efficient cooling of DACs. Furthermore, low temperature DACs are typically

made of CuBe alloy to facilitate cooling, but using this alloy makes machining more complicated due to the poisonous Be. Therefore, one of the DACs used in this thesis is made of stainless steel.

The sample is contained on the tip of the diamonds in a chamber drilled in the center of a gasket. Generally a good gasket material will be hard enough so that the sample chamber is stable at high pressure, but also malleable enough to be able to deform without cracking. Therefore the gaskets used are typically hard metals; the most commonly used materials in this thesis are rhenium and non-magnetic stainless steel.

Compression in DACs occurs along the diamonds axis, thus pressure medium is often used to generate hydrostatic pressure acting on the sample. The degree of hydrostaticity is mostly determined by the type of pressure media and the sample/pressure media ratio. Typically hydrostaticity is favored by using pressure media that remains in its gas/liquid state within the experimental conditions. Besides, amorphous solid pressure media, such as 4:1 methanol:ethanol mixture, lead to better hydrostaticity than single crystal ones. Therefore, the choice of pressure media is experiment-specific. For instance, helium is the most hydrostatic pressure media available, since it is very light, chemically inert, and freezes only at ~ 25 GPa at room temperature. However, the small molecular size makes loading He into the sample chamber a complex procedure [178]. Its large compressibility leads to a severe reduction in the chamber volume (typically more than a factor of 4) at low pressures (< 5 GPa), increasing the sample/pressure media ratio, thus reducing the degree of hydrostaticity.

Finally, the diamond anvil design is selected according to the experiment (Fig. 3.1). Primarily, the culet (diamond tip) diameter is chosen to be small enough so that the required pressure is reached, but large enough to maximize the sample chamber volume. The shape of the

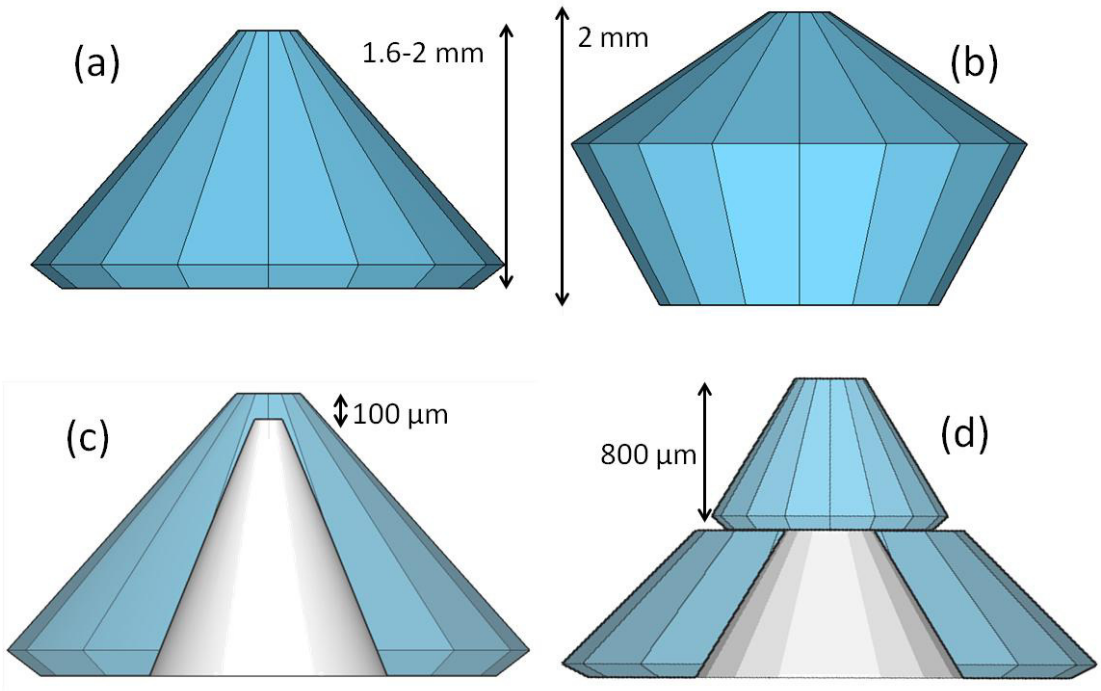

Figure 3.1: Diamond designs used in this thesis. (a) Regular anvil, (b) Boehler-Almax, (c) partially perforated anvil, (d) mini (top) and fully perforated (bottom) anvils.

diamond can also be relevant. In x-ray techniques, the photons usually travel through the diamond before reaching the sample, potentially distorting the experimental data. To minimize such distortion, fully perforated, partially perforated, and mini anvils can be used [179]. Additionally, the Boehler-Almax diamond cut is used in single crystal diffraction experiments to maximize the pressure cell angular clearance [180].

3.1.1 Pressure Calibration

In a DAC the sample pressure typically cannot be determined by *ex situ* measurement. Therefore, pressure is measured using a manometer placed in the sample chamber. The choice of manometer depends on the experimental setup available. In this thesis four different methods

were used: ruby fluorescence, diamond anvil Raman, x-ray diffraction, and x-ray absorption fine structure.

Ruby is composed of Cr doped Al_2O_3. The Cr (Al) ion is located inside a distorted oxygen octahedra, leading to a crystal field split high-spin $3d^3$ ground state [181]. Green or blue laser excites this ground state with red (~ 694 nm at ambient pressure) photons being emitted in the relaxation process [181]. Compression leads to a well calibrated shift of the fluorescence spectra to larger wavelength [181,182], which is largely used as a manometer. The popularity of the ruby fluorescence in pressure calibration comes from the relatively simple setup required. The pressure induced spectral shift is large enough that regular spectrometers can achieve < 0.1 GPa resolution. Furthermore, due to the strong fluorescence intensity, simple optics and low laser power (< 10 mW) are typically sufficient. The measurements done here make use of a revised ruby scale by Chijioke *et al.* [182]. Pressure enhances the crystal field splitting, making the excitation with green laser less efficient above ~ 40 GPa, and with blue laser above ~ 100 GPa [181].

An optical laser can also be used to calibrate pressure by measuring the diamond Raman spectrum [183]. The Raman technique consists of measuring the electron-phonon interaction by studying the inelastic scattering of light [184]. In diamond the very robust carbon sp^3 bonding leads to a single vibrational mode, commonly referred to as the diamond vibron. Hanfland and Syassen [183] showed that pressure linearly shifts the vibron mode of diamond anvils, allowing its use as a pressure calibrant. The vibron position has been calibrated to nearly 400 GPa, being a particularly useful method above 100 GPa where the ruby fluorescence becomes very weak. However, the weak vibron intensity demands a much enhanced optical system when compared to one for ruby fluorescence.

Finally, pressure can be calibrated by measuring the manometer's equation of state using x-ray powder diffraction. In this case, ideal manometers display simple structures with no phase transitions in the pressure range of interest. Consequently, heavy transition metals such as silver and gold are commonly used [185]. The equation of state can also be measured using x-ray absorption fine structure (see section 3.4). This method is unconventional due to its complex data analysis and limited spatial accuracy (about 0.01 Å for high pressure experiments), but it was used in some of the present measurements, where other options were impractical.

3.2 Resistivity

Electrical resistivity is an intrinsic measure of the resistance exerted by a material to the flow of electrons. It is generally controlled by the material's Fermi surface and the scattering of conduction electrons with (quasi) particles. Consequently, resistivity is sensitive to a plethora of phenomena such as lattice vibration and magnetic order. A striking property of a superconductor is absence of measurable resistivity. Hence such strong suppression makes measuring the superconducting transition temperature (T_c) rather straightforward in a resistivity experiment.

Electrical resistivity is typically probed through a resistance measurement. The relationship between resistance and resistivity is controlled by geometrical aspects of the measurement, such as shape of the sample and position of wires. However, the exceedingly small sample (~ 30x30x10 μm^3 in this work) used in high pressure measurements prevents the reliable determination of the geometrical factor, hence resistivity. Nevertheless, since the geometrical factor is temperature independent, it simply contributes as a scaling factor in R(T), which does not affect the measurement of T_c.

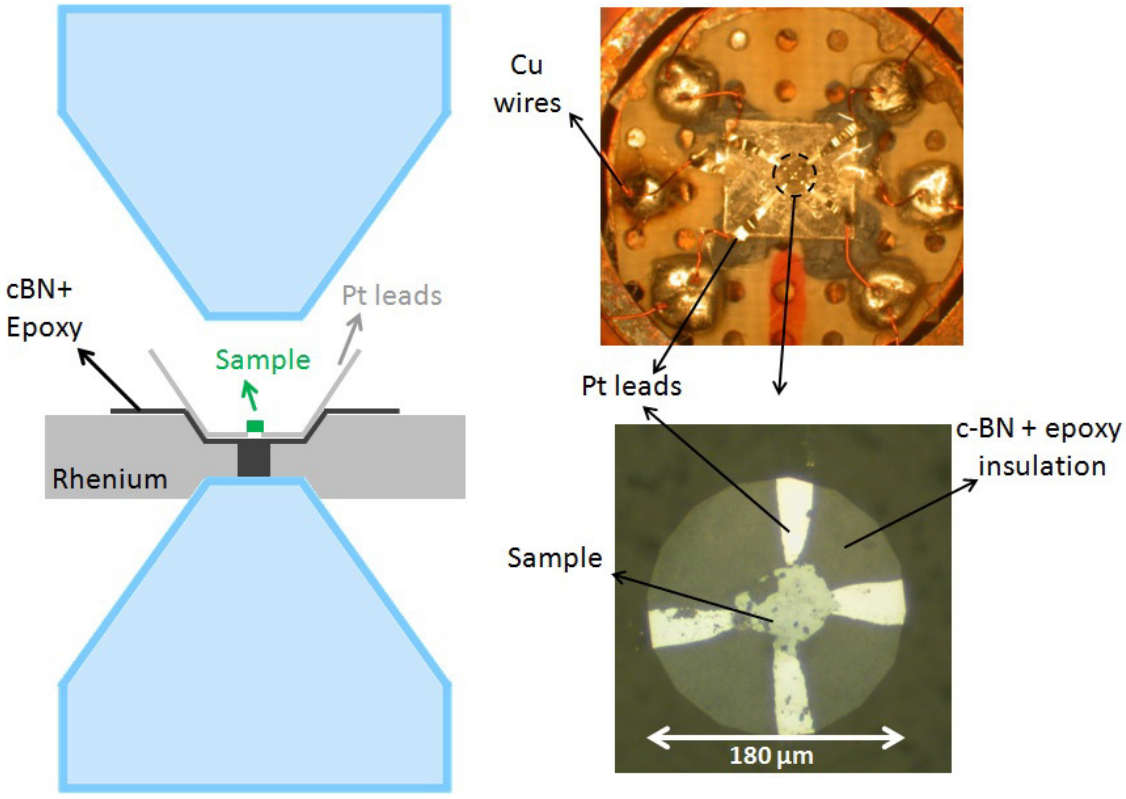

Figure 3.2: High pressure resistance setup. Left: DAC diagram. Right: pictures of setup, the gasket mounted in the DAC is shown on top, and a zoom on the diamond culet showing the Pt wires and sample on bottom.

3.2.1 Electrical Resistance Measurement on Y(RE) Alloys

DC electrical resistance was measured using the four points method (Fig. 3.2), which eliminates the wire and sample-wire contact resistances by using two points for the current flow and two separate for voltage measurement. A CuBe DAC was outfitted with regular diamond anvils and a Re gasket. The metallic gasket was insulated using c-BN + epoxy mixture. Four Pt strips are cut from a 5 µm thick foil and manually placed on the insulated indented area to serve as leads. Their placement is a critical and technically challenging task, as ideally these will be the

closest the possible without touching, typically < 20 μm apart from each other, in order to reduce the pressure gradient measured along the sample, which is significant in this non-hydrostatic measurement. The leads are also required to sit flat on the culet so the sample can be placed on top. Electrical contact is made by pressing the sample into the leads using the top anvil. This method is depicted in Fig. 3.2. The fragile Pt leads are connected to Cu wires, the later routed out of the cell. Note that the c-BN + epoxy mixture also serves as a non-hydrostatic pressure media. Furthermore, the gasket insulation can be damaged at extreme pressures, potentially resulting in lead-gasket contact. Two extra leads are directly connected to the gasket in order to verify this possibility *in situ*.

The assembled DAC was cooled with an Oxford He flow cryostat that features an electrical feedthrough to route the leads into the measurement electronics. A constant current was generated using a Keithley 220 source, and voltage was measured using a Keithley 182 voltmeter connected to a data acquisition computer. The severe temperature gradient along the Cu wires leads to a thermovoltage that is corrected by measuring the resistance with the current flowing in two opposite directions, with the resistance being the average of the two measurements.

3.3 X-ray Diffraction

An incident photon with wavevector $\vec{k}_i$ can elastically scatter from an electron, reaching a final wavevector $\vec{k}_f$ such as $|\vec{k}_i| = |\vec{k}_f|$. When more than one electron is present, the difference in path length between the photons scattered from each electron leads to interference and carries information on the electronic distribution [186]. The x-ray diffraction technique makes use of this interference to retrieve the density of electrons [186]. Since most electrons in a material are tightly bound to the atomic core, this method is widely used to investigate materials structure. Despite its primary use in structural studies, charge order of valence electrons can also be

detected [13,187], a property that is used here to investigate stripe order in $LBCO_{1/8}$ (see section 4.1.4).

If a material displays crystaline order, diffraction peaks occur when the sample is oriented with respect to the x-ray beam so that an atomic plane (Bragg plane) obeys Bragg's law [186]

$$\lambda = 2dsin\theta \tag{3.1}$$

where λ is the x-ray wavelength, d the interplanar distance, and θ the Bragg angle (see Fig. 3.3). This scattering process can also be understood in momentum space, where the momentum transfer, $\vec{Q} = \vec{k}_f - \vec{k}_i$, is a reciprocal lattice vector (Bragg peak) (Fig. 3.3). In this picture, the Bragg planes are described by their Miller indices (h k l) such as

$$Q_x = \frac{2\pi}{a}h;\ Q_y = \frac{2\pi}{b}k;\ \ Q_z = \frac{2\pi}{c}l \tag{3.2}$$

where a, b, c are the lattice parameters.

The structure of a crystal is fully determined by the knowledge of the lattice parameters and unit cell basis [186]. According to equation 3.1, θ is related to the interatomic spacing, which can be parameterized in terms of the lattice constants obtained by measuring the position of several diffraction peaks. On the other hand, the basis is mostly determined from the relative peak intensity, being proportional to the structure factor

$$F_{hkl} = \sum_n f_n e^{2\pi i(hx_n+ky_n+lz_n)} \tag{3.3}$$

where n is each atom in the unit cell, x_n, y_n, z_n are the fractional atomic positions inside the unit cell, and f_n is the atomic scattering amplitude [186]. Therefore, the relative intensity of diffraction peaks is related to the atomic positions inside the unit cell.

X-ray diffraction is a well established technique, branching through many different applications and methods (see for instance [186,188]). In the sections below single crystal and powder diffraction methods used in this thesis are discussed in more detail.

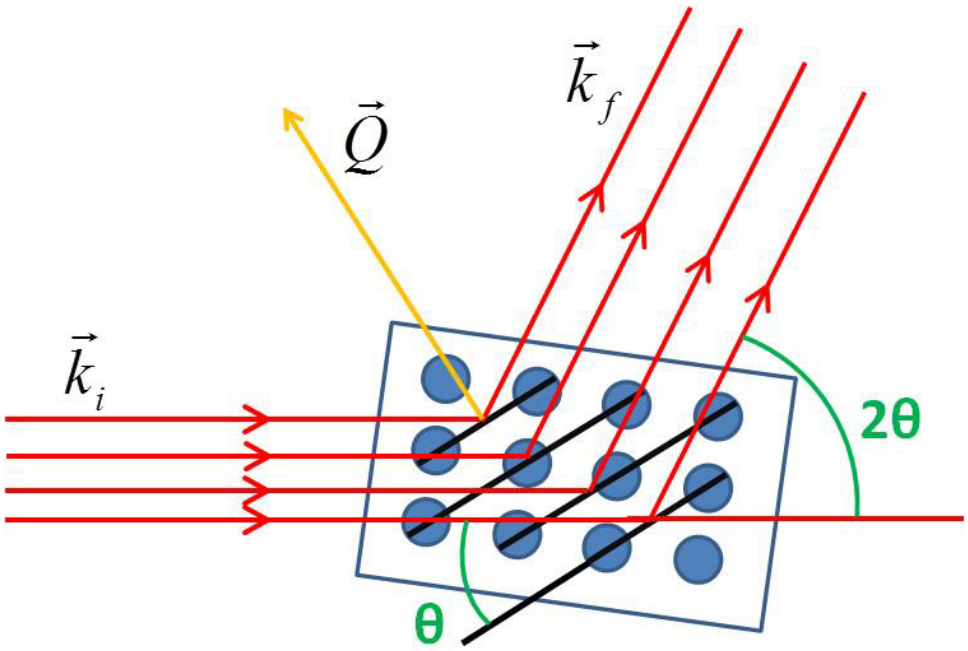

Figure 3.3: Sketch of x-ray diffraction by a single crystal.

3.3.1 High-Pressure Single Crystal Diffraction

Single crystal diffraction was measured with a monochromatic incident x-ray, using a vertical scattering plane (i.e. the plane formed by $\vec{k}_i$ and $\vec{k}_f$). In this geometry, the sample is rotated to bring the orientation of $\vec{Q}$ into the scattering plane and its magnitude into the Bragg condition (equation 3.1).

3.3.1.1 - Single Crystal Diffraction on $LBCO_{1/8}$

The experiments were performed at the 4-ID-D beamline of the Advanced Photon Source (APS), Argonne National Laboratory (ANL). In single crystal diffraction mode, the beamline optics consists of a double crystal Si (111) monochromator, a Pd focusing toroidal mirror, and a Si/Pd flat mirror (Fig. 3.4). The focused beam size at the sample position is ~ 100x200 μm^2,

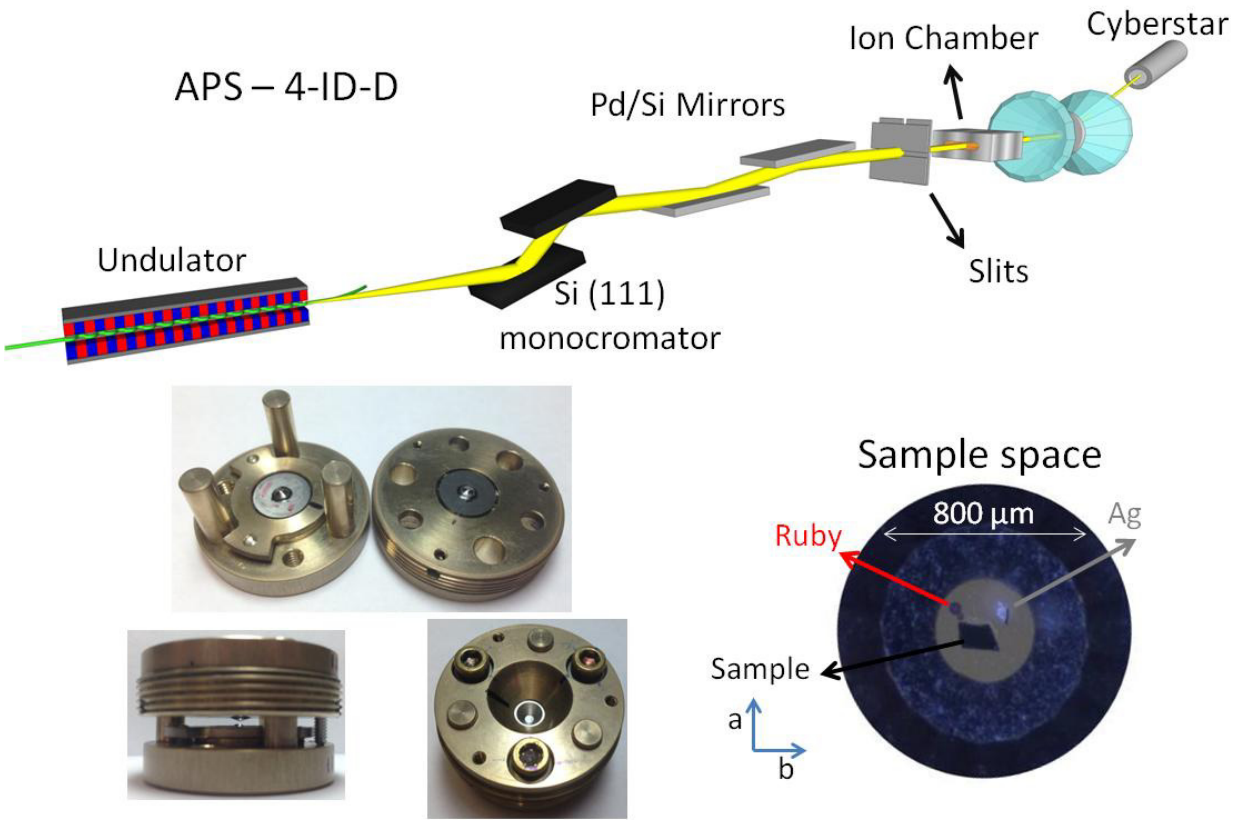

Figure 3.4: Top: Scheme of the single crystal diffraction setup at 4-ID-D. Bottom: Pictures of the DAC and sample space can be seen on left and right panel, respectively.

which can be further reduced the use of slits to ~ 50x50 μm^2. The DAC was cooled using a He closed cycle cryostat mounted to an eight circle Huber diffractometer.

High-pressure was generated using a DAC designed and machined at University of Chicago (see Fig. 3.4). Laue diffraction geometry was used, in which x-rays diffract while transmitting through the sample (as well as the diamond anvils). The DAC angular apertures limit the accessible Bragg peaks. This cell features Boehler-Almax diamond anvils, in which the anvil is embedded into the seat, increasing the angular aperture to ~ 60°. Furthermore, the scattering angle (θ in equation 3.1) can be reduced by increasing the x-ray energy (reducing λ), enabling

the access of more Bragg reflections. Pressure was controlled at low temperature using a He driven membrane and calibrated by measuring diffraction from an Ag polycrystalline foil placed in the sample chamber, and using the tabulated Ag equation of state [185].

Two different single crystal diffraction experiments were performed on $LBCO_{1/8}$. Firstly, diffraction from (1 0 0), (2 0 0), and (0 0 6) peaks was collected concomitantly with polarized x-ray absorption fine structure measurements (see section 3.4.1.1) to align selected crystalline axis with the x-ray horizontal electric field and to investigate the LTT-HTT transition. This experiment was performed at 38.89 keV (λ = 0.3188 Å). In the second experiment which focused on the relationship between local LTT domains and CO, a similar setup as described above was used, albeit the use of 20 keV (λ = 0.6199 Å) photons to enable x-ray focusing through a Pd toroidal mirror (cutoff energy ~ 21 keV), and crystal cut displaying the $\hat{a}$ and $\hat{b}$ axis perpendicular to the beam was used to allow detection of the CO peak. Guided by previous findings [70], LTT and LTT/LTO domains were probed by measuring the (1 0 0) and (1.5 1.5 2) peaks respectively, while incommensurate CO was monitored through the (2-2δ 0 0.5) peak with $\delta \approx x = 0.125$.

The greatest advantage in using single crystal diffraction is the much larger diffraction intensity when compared to its powder counterpart (see next section). When coupled to the setup at 4-ID-D, this method is capable of detecting weak Bragg peaks that are around 10^7-10^8 times weaker than strong lattice peaks, thus enabling the measurement of the very weak diffraction peaks such from stripe charge order (note that only a small number of doped charges contribute to CO).

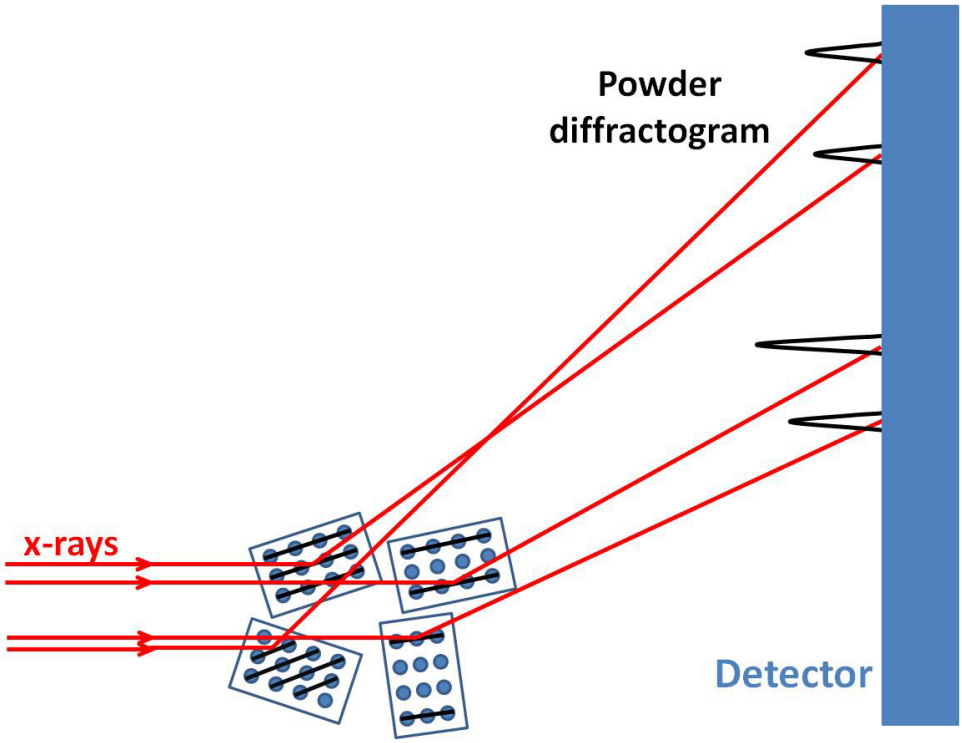

Figure 3.5: Powder diffraction from a collection of crystallites.

3.3.2 High-Pressure Powder Diffraction

Diffraction from randomly oriented powder is also able to yield a material's structure. If the number of grains is large enough, for a given photon energy there will always be crystals oriented properly so that equation 3.1 is satisfied for every allowed diffraction peak (Fig. 3.5). The random orientation leads to a diffraction cone (Debye-Scherrer cone) with an angle θ (or 2θ as commonly used). Such averaging of angular information may prevent solving unknown or complex structures. Powder diffraction is usually analyzed using the Rietveld refinement method [189], in which intensities and peak positions of all available Bragg peaks are simultaneously fit. However, experimental difficulties, such as poor powder averaging, can particularly hamper the ability of parametrizing the intensities. Therefore, the Le Bail method is

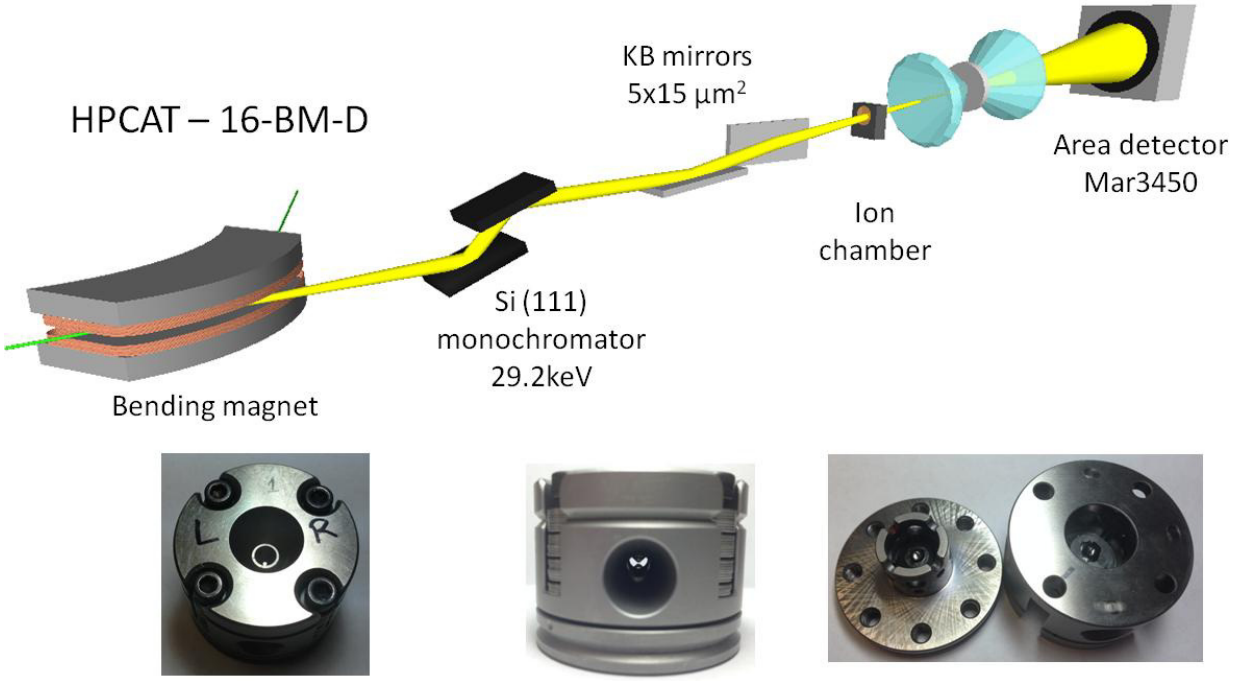

Figure 3.6: Top: Scheme of the 16-BM-D beamline. Bottom: Symmetric cells used on powder diffraction, Tb L_3 XANES (section Chapter 1), and Tb Lγ XES (section 3.5.1).

sometimes used [190] in which the peaks intensity and shape are not correlated to the structure, and only lattice parameters are obtained from the fitted peak positions.

3.3.2.1 - X-Ray Powder Diffraction on Alkalis

High pressure powder diffraction was measured at HPCAT's 16-BM-D beamline at the APS, ANL (see Fig. 3.6). Photon energy is selected using a double crystal Si (111) monochromator. A set of Kirkpatrick-Baez mirrors is used to focus the beam to a ~5x15 μm^2 spot at the sample position. The diffraction pattern is measured using a MAR345 image plate. The radius of the circular 2D data is converted into 2θ by measuring a CeO_2 standard. The 2D diffractogram is radially integrated using the program Fit2D [191], leading to a 1D intensity vs. 2θ graph.

The 16-BM-D beamline setup is optimized to be used with the symmetric cell produced by the Princeton shops (Fig. 3.6). In order to maximize the measurable 2θ range, the diamond facing the detector is glued to an x-ray transparent boron carbide seat. High energy x-rays (29.2 keV, 0.4246 Å) are used to collapse the reciprocal space (reduce θ in equation 3.1), hence enabling the measurement of a larger number of peaks. This stainless steel pressure cell was cooled using a He flow cryostat. Pressure was applied by turning the cell's screws through a gearbox located inside the cryostat. Ruby fluorescence was used to calibrate pressure *in situ*. The small sample volume (~0.001 to 0.04 mm^3) required to achieve high-pressures in a DAC typically leads to poor powder averaging, thus Rietvield refinements are commonly unfeasible. Data analysis was performed using GSAS [192] through the EXPGUI interface [193].

3.4 X-Ray Absorption Fine Structure

In the x-ray regime, the atomic photon-electron cross section is dominated by the photoelectric effect [194]. Discontinuities in the absorption coefficient (absorption edge) are observed when the incident photon energy is tuned across the binding energy of a core electron state. At energies larger than the absorption edge, the core electron is excited to a state above the Fermi level. The scattering of this photoelectron from neighboring atoms leads to oscillations in the absorption coefficient (Fig. 3.7), which are measured and studied with the x-ray absorption fine structure (XAFS) technique [195,196]. Since the absorption edge energy is atom specific and the ejected photoelectron has a small mean free path ($\lesssim$ 10 Å), the XAFS technique is an element specific local environment probe [195,196]. The absorption coefficient ($\mu(E)$) is typically measured in transmission geometry by monitoring the x-ray intensity before ($I_0(E)$) and after the sample ($I(E)$) as the x-ray energy is scanned through the absorption edge. Using Beer's law

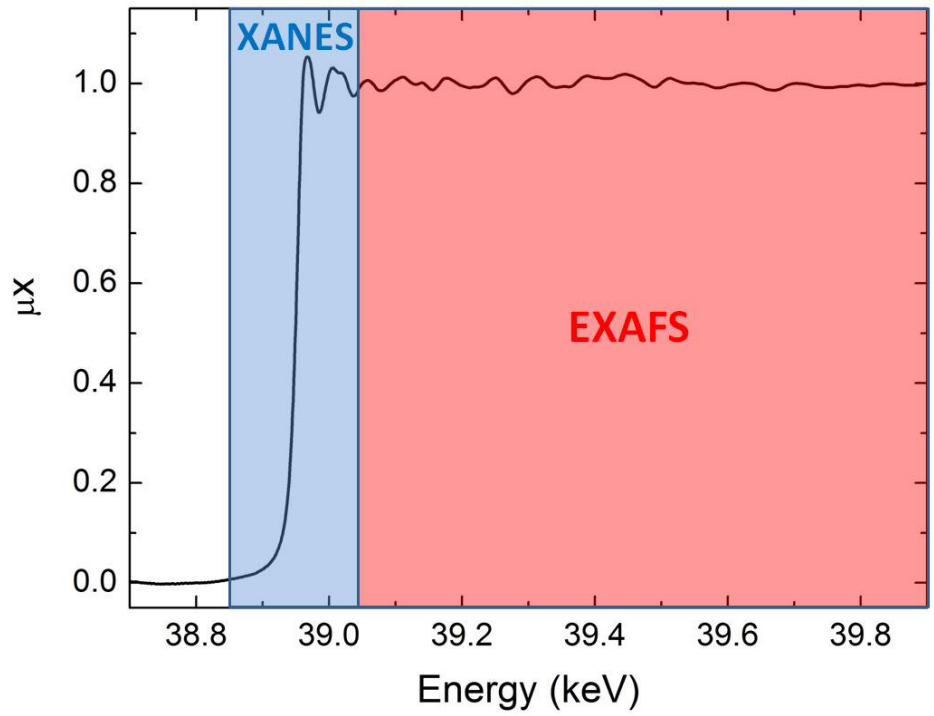

Figure 3.7: La K absorption edge in $LBCO_{1/8}$.

$$I(E) = I_0(E)e^{-\mu(E)x} \rightarrow \mu(E)x = ln(I_0(E)/I(E)) \tag{3.5}$$

where x is the sample thickness and μx is the absorbance. Alternatively, the $\mu(E)$ can be measured by detecting the emitted (fluorescence) photons generated when the excited atom decays to its ground state [195]. In this case

$$\mu(E) = I_F(E)/I_0(E) \tag{3.6}$$

where I_F is the fluorescence intensity.

XAFS can be divided into two separate regimes (Fig. 3.7), the x-ray absorption near edge structure (XANES) region and the extended x-ray absorption fine structure (EXAFS) region. The former corresponds to ~ 30 eV above the absorption edge, while the later spans from ~30 eV to ~1500 eV [197]. The critical difference between these regimes is the kinetic energy of the ejected photoelectron ($E-E_0$ where E_0 is the absorption edge energy). In the XANES region, the

photoelectron has low kinetic energy, thus scattering from outer (valence) electrons is more relevant, giving sensitivity to details of the interatomic potential, and containing information such as valence state and hybridization [196]. On the other hand, the high energy photoelectron in the EXAFS region leads to scattering from inner electrons, with the resulting interference pattern interpreted in terms of local structure information [195,196].

The cross section (σ) for the XAFS process can be formulated by treating the photon-electron interaction as a perturbation within the Fermi golden rule [198,199]

$$\sigma \propto \sum_f \left|\langle f|\vec{A}|i\rangle\right|^2 \tag{3.7}$$

where i and f are the initial and final multi-electron state, and $\vec{A}$ is the photon field operator. While the initial electronic state can be well calculated using ground state methods such as density functional theory (DFT), calculating the final (excited) state is difficult [196]. As shown in the following sections, while good approximations can be made when treating the EXAFS region, the low photoelectron energy of the XANES counterpart makes it more difficult to interpret.

In a high-pressure XAFS measurement the x-ray beam typically transmits through the diamond anvils to reach the sample. However, contrary to diffraction, the resonant character of XAFS restricts the incident x-ray energy. As any other material, diamonds interact with the x-rays by absorption and diffraction, both potentially distorting the data. A typical regular diamond anvil used in this thesis is ~ 1.7 mm tall (Fig. 3.1), at the Tb L_3 edge (7.514 keV), for instance, the diamonds alone will reduce the beam intensity by a factor of 2000. Furthermore, since incident energy is scanned in a measurement, a diamond Bragg peak may be reached, removing x-rays from the incident or transmitted beam, and distorting the data. The short energy range of the XANES region can be typically be cleaned from diamond Bragg peaks by rotating the DAC,

however this is much harder to accomplish for the the extended range of EXAFS making it a complicated technique to implement in a DAC. To minimize these issues, the use of perforated and mini anvils is essential (Fig. 3.1). Furthermore, the recently developed nanocrystaline diamond anvils have been adopted with success [200].

3.4.1 Extended X-Ray Absorption Fine Structure

The EXAFS can be well described by treating the absorption cross section as a sum of different scattering paths for the ejected electron (Fig. 3.8), within the so called multiple scattering approach [196]. This scenario is mathematically described by approximating the interatomic potential as muffin-tins, in which the potential is spherically symmetric at the atomic position and constant in the interstitial region.

The final state is then expanded in terms of number of scattering events. This expansion is quickly convergent, being typically truncated in the fourth order. Therefore, the oscillations can be theoretically parameterized [198,199,201] leading to the EXAFS equation:

$$\chi(k) = \sum_i \frac{N_i S_0^2}{kR_i^2} e^{-2\sigma_i^2 k^2} e^{-2R_i \lambda_k^{-1}} \left| f_{eff}(k) \right| \sin(2kR_i + \Phi_k) \qquad (3.8)$$

where i corresponds to the different scattering paths, and the energy scale is converted into the photoelectron wavelength ($k = \sqrt{2m/\hbar^2 (E - E_0)}$, E_0 is the absorption edge energy). The remaining terms can be split into two categories: electronic and structural. The former is composed of the amplitude reduction factor (S_0^2), mean free electron path (λ), effective scattering amplitude (f_{eff}), and scattering phase shift (Φ). Since the EXAFS region is not very sensitive to details of the valence electrons the muffin tin approximation can accurately calculate these parameters, as implemented in the *ab initio* FEFF8 code [202]. The structural terms can

then be adjusted to the experimental data. These are: the degeneracy of the path (N), half of the path lenght (R), and the Debye-Waller factor (σ) (structural disorder).

Data manipulation and fitting was performed using the IFEFFIT/HORAE package [203,204]. From equation 3.8 it can be seen that the oscillatory EXAFS function has "k" wavelength, and 2R frequency. Therefore data analysis is often performed in real space by Fourier transforming the data (Fig. 3.9), with the resulting spectra being a pseudo radial distribution function [196,198,199,201]. This also implies that the EXAFS spatial resolution is connected to the k-range by

$$\Delta R \sim \frac{\pi}{2k_{max}} \tag{3.9}$$

. Ideally, the larger k_{max} leads to better spatial resolution, however the Debye-Waller factor exponential dependence on k^2, together with the decrease of $|f_{eff}(k)|$ at high k, typically limits k_{max} to ~ 15 $Å^{-1}$, therefore ΔR is usually larger than 0.1 Å.

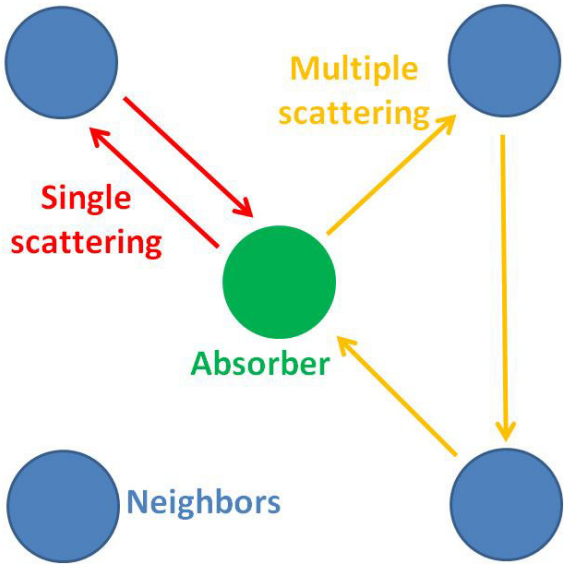

Figure 3.8: Example of single and multiple photoelectron scattering from neighboring atoms.

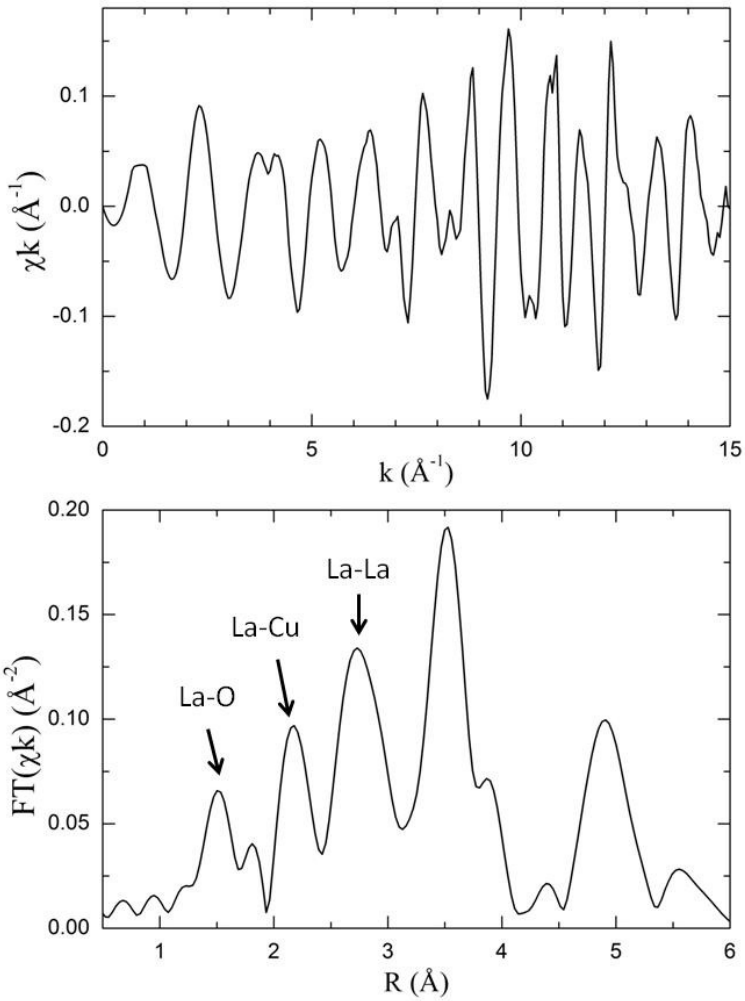

Figure 3.9: La K-edge EXAFS on $LBCO_{1/8}$. Top: χ(k) EXAFS spectra. Bottom: Fourier transform of χ(k). The resulting function is a pseudo-radial distribution function.

In a single crystal the EXAFS is sensitive to the scalar product of the x-ray polarization and the scattering path direction. Therefore, by exploiting the linear horizontal polarization of synchrotron x-rays, the polarized EXAFS method is particularly useful to investigate materials with anisotropic local structures [64,65]. The polarization dependence is included in the calculation of the f_{eff} term, and can be non-trivial for multiple scattering terms. For single scattering paths and K-absorption edge (1*s* excitation), it is simply given by the square of the cosine of the angle between the horizontal polarization and the bond direction. This factor can be

understood as an enhanced probability of having the electron ejected along the x-ray electric field. In this thesis this polarization dependence was exploited to solve the local structure in layered (anisotropic) $La_{1.875}Ba_{0.125}CuO_4$.

3.4.1.1 - Concomitant Polarized EXAFS and Single Crystal Diffraction on $LBCO_{1/8}$

Concomitant polarized EXAFS and single crystal diffraction experiments were performed at the undulator beamline 4-ID-D of the APS, ANL. The experimental setup is very similar to the one depicted in Fig. 3.4. Polarized EXAFS at the La K-edge (38.95 keV) was measured in order to enhance the sensitivity to detecting local CuO_6 tilts (see section 4.1.1). The incident x-ray intensity was monitored using an Ar filled ion chamber. EXAFS was measured in transmission mode using a Kr filled ion chamber, and diffraction was detected using a NaI (Cyberstar)

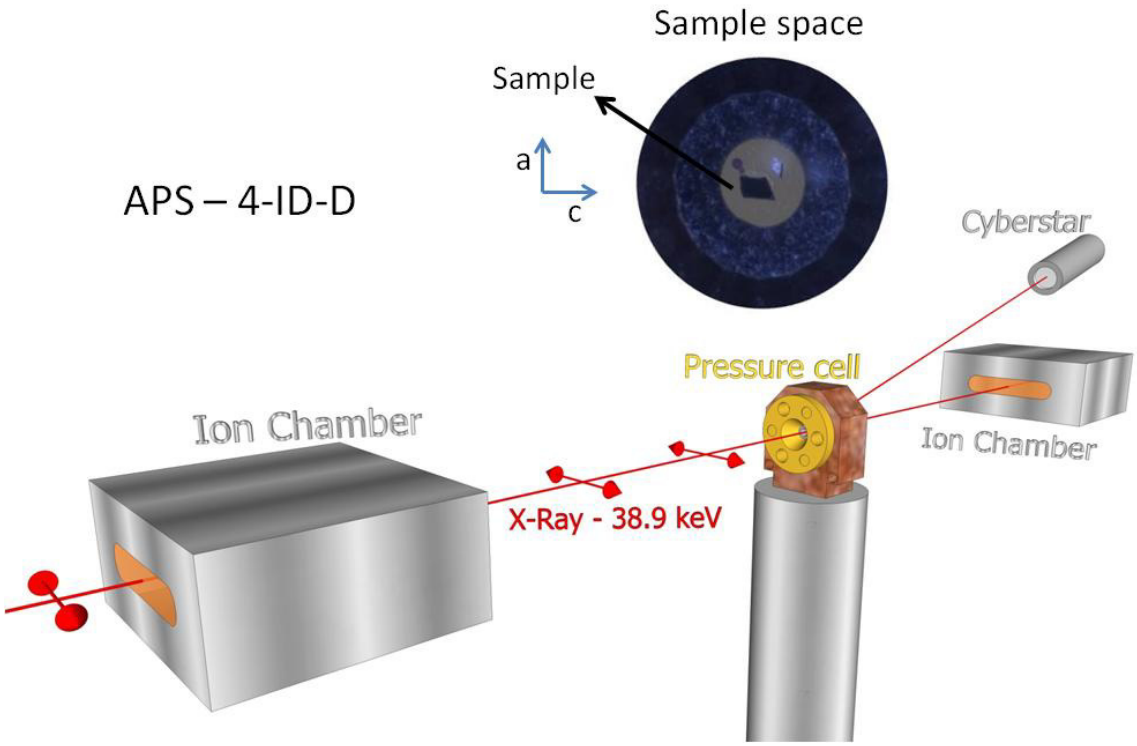

Figure 3.10: Polarized EXAFS setup.

scintilator detector (Fig. 3.10).

The experiments were performed using a membrane driven DAC (Fig. 3.2). Boehler-Almax full diamonds with 800 μm culet diameter were initially used, but diffraction from the anvils introduced several glitches in the XAFS data. This problem was mitigated by using a 600 μm culet diameter partially perforated anvil paired with a set of fully perforated and mini anvils (Fig. 3.1). Stainless steel gaskets were used; holes of half the culet size were electrically drilled and used as sample chamber. The low pressure range of this experiment (up to ~5 GPa) makes Methanol:ethanol (4:1) mixture an overall superior pressure media as it prevents the reduction of the sample to pressure media volume ratio. Both diffraction and EXAFS were measured in transmission geometry. Diffraction was confined to the vertical scattering plane. The sample chamber was loaded with a small $LBCO_{1/8}$ single crystal oriented with $\hat{a}$ and $\hat{c}$ axis perpendicular to the incident x-ray direction (Fig. 3.10). The DAC was mounted in a He closed cycle cryostat, assembled in an eight circle Huber diffractometer.

EXAFS measurements were done with the horizontal x-ray linear polarization oriented along $\hat{a}$ and $\hat{c}$ axis by rotating the crystal about the incident wavevector and into the (006) or (200) Bragg peaks, respectively. The crystal alignment was done at each pressure. The LTT-HTT structural transition was concomitantly measured by probing the LTT-only (100) peak. Polarized XAFS data was collected to ~860 eV (k ~ 15 $Å^{-1}$) above the edge.

3.4.1.2 - Characterization of Y(RE) Alloys

The Y(RE) alloys were prepared by arc-melting. In order to verify the absence of the dopant clustering, EXAFS measurements were performed at the 4-ID-D beamline of the APS, ANL. Data was collected at the L_3 edges of Pr (5.964 keV), Gd (7.243 keV), and Tb (7.514 keV). The low concentration of dopants prevents transmission mode measurements [195]. Therefore,

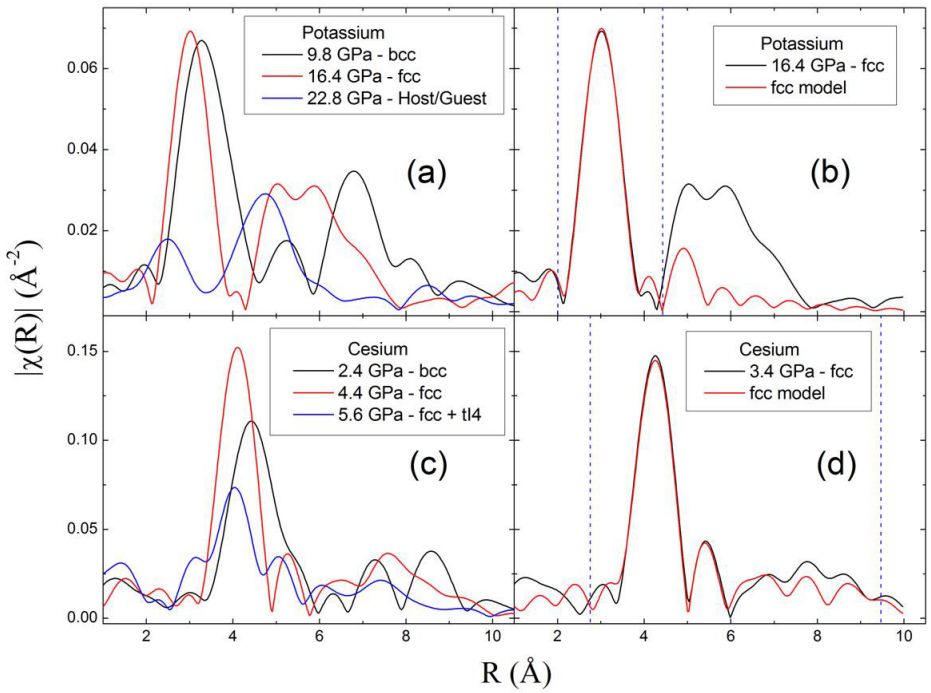

Figure 3.11: K K-edge (a,b) and Cs-L_3 edge (c,d) EXAFS used for pressure calibration

EXAFS was collected in fluorescence using energy dispersive, four element silicon drift diode detector.

3.4.1.3 - Pressure Calibration on XANES Measurements of K and Rb

Alkali metals are very soft (see Fig. 4.28), thus despite the limited spatial accuracy in EXAFS (~ 0.05 Å for these experiments), the large change of interatomic distances with pressure allows for reliable pressure calibration. Furthermore, the change in symmetry across the phase transitions is clearly seen in the data (Fig. 3.11) corroborating the obtained pressure.

Despite the use of two partially perforated anvils, large harmonic contamination in the x-ray beam still distorts the K EXAFS data (odd multiples of the incident energy is transmitted by the Si monochromator). Such contamination also distorts the EXAFS region, particularly its

amplitude. Nevertheless, the obtained distances, hence pressures, are in excellent agreement with the observed phase transitions.

Finally, while Cs displays a rather symmetric tI4 structure at high-pressure, K-III is very complex. Thus for K, the pressures above 19 GPa were obtained by extrapolating the linear behavior of the membrane pressure vs. sample pressure.

3.4.2 X-ray Absorption Near Edge Structure

The theoretical treatment of XANES is much more complex than EXAFS, being commonly interpreted by comparing with either *ab initio* simulations or experimental standards [196]. Different approaches can be used to simulate the XANES spectra. In this thesis the full multiple scattering formalism implemented in FEFF8 [197] and the finite difference method as implemented in FDMNES [205] were used.

In the XANES region the low energy of the photoelectron enables several orders of multiple scattering paths, thus, opposed to the EXAFS regions, truncating the multiple scattering expansion leads to severe deviations (see section 3.4.1) [196]. Consequently, the XANES is simulated using the full multiple scattering approach, in which all orders of scattering are solved for a finite cluster [196]. The limitation in this method is the muffin-tin description of the interatomic potential. While this approximation works well in the EXAFS region, it is much less successful in the XANES region due to larger sensitivity to details of the electronic potential.

In order to avoid the muffin-tin approximation, another approach to solving equation 3.6 needs to be taken. An alternative is the finite difference element method, in which the calculation cluster is split into a grid; the final state of the photoelectron is calculated for every point of this grid, and equation 3.6 is then solved. This method is much more computationally demanding than the full multiple scattering approach. However, it has the significant advantage of allowing

the use of an interatomic potential with arbitrary shape. Therefore, the program allows the use of potentials from the well established density functional theory, both through an internal code, or by importing calculations done with the WIEN2k program [206].

Given its difficult theoretical treatment, the qualitative comparison to experimental standards is commonly used in data analysis. Particularly in this thesis, such an approach was taken in the Tb L_3 data analysis. In lanthanides the L_3 edge energy position is well known to be strongly dependent on the number of 4*f* electrons [207–210]. Furthermore, due to the dipole selection rules, the $2p_{3/2}$ core electron is excited to one of the nine 5*d* empty states, leading to a large peak at the absorption edge (white line) which area is proportional to the 5*d* occupation.

3.4.2.1 - Tb L_3

High pressure Tb L_3 XANES experiments were performed at room temperature at the PNC/XSD 20-BM beamline of the APS, ANL. This beamline features a double crystal Si (111) monochromator coupled to a pair of Kirkpatrick-Baez mirror, generating a ~ 3 x 5 μm^2 beam at the sample position. XANES was collected in transmission mode using two N_2 filled ion chambers to detect the incident and transmitted intensities (Fig. 3.12). A symmetric cell was prepared with diamonds of 300 μm beveled to 180 μm culet diameter. A regular anvil was paired to a partially perforated anvil to improve counting statistics. A rhenium gasket was pre-indented to 30 μm; an 80 μm diameter hole was laser drilled in the center of the indentation to produce the sample chamber. The chamber was loaded with a piece of Tb foil (Alfa Aesar, 99.9% purity), ruby balls (manometer), and neon gas pressure media. Pressure was applied by tightening the DAC screws.

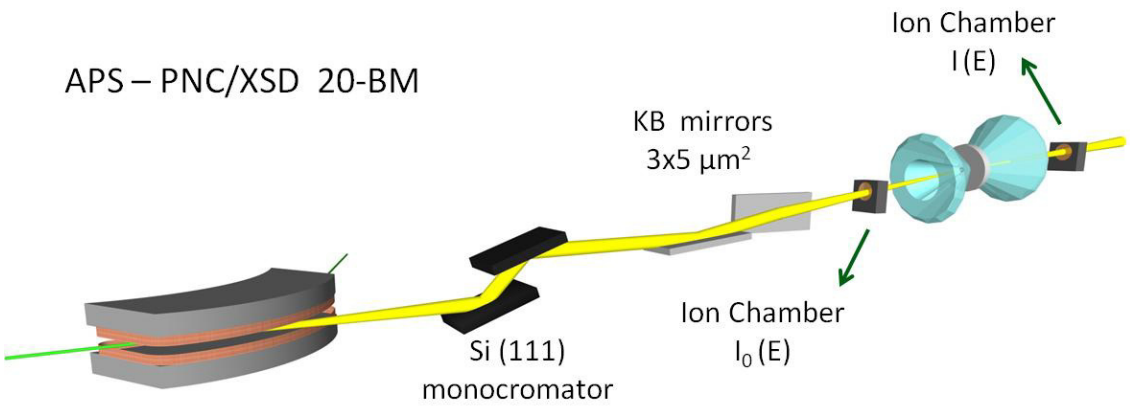

Figure 3.12: XANES setup at beamline 20-BM.

3.4.2.2 - Heavy Alkali Metals

High pressure XANES measurements were performed at the K K-edge (3.608 keV), the Rb K-edge (15.2 keV) and the Cs L_3-edge (5.012 keV) at beamline 4-ID-D of the APS, ANL. For Rb, a membrane driven CuBe DAC was prepared with a partially perforated diamond paired with a mini anvil glued on top of a fully perforated diamond. Ruby fluorescence was used to calibrate pressure. The same pressure cell was used for K and Cs, but the low energy of their absorption edges demanded the use of two partially anvils to reduce absorption by the diamonds. However, these anvils are opaque to visible light, thus for K and Cs pressure was determined by measuring their EXAFS, which contains information on the short range distances, and the obtained distances were compared to the equation of state measured in this thesis by diffraction. Diamonds with culet diameter of 300, 450 and 600 μm were used for K, Rb, and Cs respectively. Rhenium gaskets were used in K's and Rb's experiments, and stainless steel in Cs's. For Rb the gasket was pre-indented to ~1/6 of the culet diameter. Due to large sample absorption, the gaskets for K and Cs were pre-indented to ~15 μm. X-ray powder diffraction was measured in

the sealed pressure cells prior to the XANES measurement to verify the sample integrity. The experiment was performed at 1.6 K using a He flow cryostat; the temperature was increased to 15 K during pressure increase. A set of a Pd toroidal and Pd/Si flat mirror was used to focus the x-rays to a spot of ~ 150 μm diameter, the beam size was then further reduced using slits. These mirror also served to reduce the harmonic contamination, and additional suppression was achieved by detuning the monochromator. For Rb's experiment, the intensity of the x-rays before and after the sample was measured using photodiodes, while for K's and Cs's, the incident intensity was measured with a He filled ion chamber, and the transmitted photons were detected with an photodiode located inside the cryostat, preventing further absorption from the cryostat's Be windows and air which is particularly important for K. XANES data was processed using the IFEFFIT/Horae package [203,204].

XANES simulations were performed using the FEFF8 [197] and FDMNES/WIEN2k software [205,206]. FEFF calculations were performed in full multiple scattering mode using clusters of ~ 300 atoms. In FDMNES, the finite difference method was used in a cluster of ~100 atoms. DFT calculations were performed using the WIEN2k code using PBE exchange correlation potential with 10000 k-points for the bcc and fcc phases, and 2000 for Rb-III and Cs-IV. In all calculations the experimental lattice constants at the corresponding pressures were used. FDMNES/DFT was not performed in the K-III structure due to its very low symmetry structure.

3.5 Non-Resonant Lγ X-Ray Emission Spectroscopy

Immediately following the x-ray absorption process, the atom is left in an excited state, with a hole in an inner core state. This is the initial state in the x-ray emission process (Fig. 3.13). The atom returns to its ground state by transferring an outer electron into the core hole. The

difference in energy between the outer and core state is released by either emitting valence electrons (Auger process), or by emitting photons; in the hard x-ray regime ($\gtrsim$ 2 keV), the later is more likely [211]. The cross section of this process can be formally described in a similar way as the absorption process (equation 3.6). The energy of the emitted x-rays corresponds to the difference in energy between the initial (hole in 2*p* level) and final (hole in 4*d* level) states, therefore it is dependent on the final state hole level (Fig. 3.13); different final states lead to different transition probabilities.

In this thesis, Tb's Lγ emission line was investigated, corresponding to a $4d^9$ final state (Fig. 3.13). This line is of particular interest because its final state displays a total angular momentum different from zero. Its spatial overlap with the semi-filled 4*f* level leads to an exchange splitting of the final state, which is experimentally observed. The Lγ line splitting is directly related to details of the 4*f* level; therefore, it has been used to investigate pressure induced 4*f* level changes in Ce [120] and Gd [125]. Similarly, measurements of the $K\beta_1$ emission in Fe have demonstrated the sensitivity of the x-ray emission method to high-low spin transitions under pressure [212,213].

3.5.1 Tb Lγ

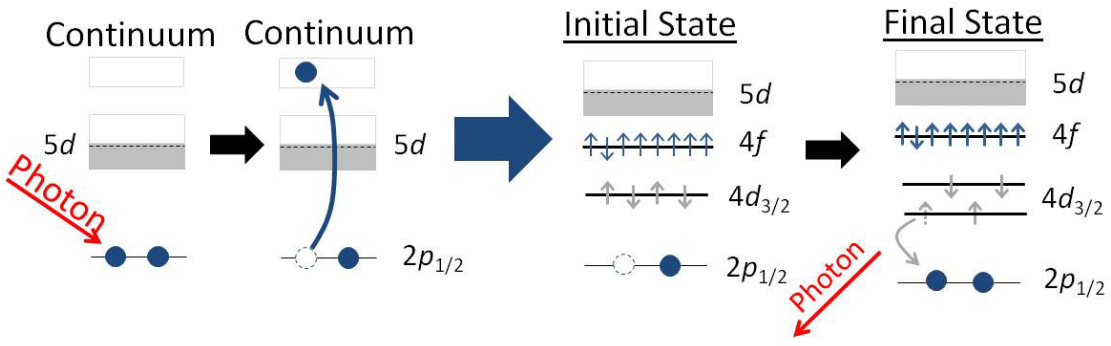

Figure 3.13: Scheme of the Lγ XES process.

The high pressure non-resonant Tb L_γ x-ray emission experiment was performed at room temperature at the HPCAT 16-ID-D beamline of the APS, ANL. Photon energy was selected to 11.3 keV using a Si (111) monochromator. The x-ray was focused to ~ 40x60 μm^2 using a set of Kirkpatrick-Baez mirrors. A symmetric cell was prepared with regular 300 μm culet diameter diamond anvils. In the geometry used, the emitted photons were detected perpendicularly to the x-ray direction using a Si(444) crystal energy analyzer coupled to a scintillator detector (Fig. 3.14), thus an x-ray transparent Be gasket was used. The requirement of reaching relatively high pressures (~70 GPa) using a soft Be gasket is challenging. The Be gasket was indented to ~ 50 μm, and its whole culet area was replaced by a pressed c-BN/epoxy mixture. A ~100 μm hole diameter was laser drilled in the center of the c-BN/epoxy insert and used as sample chamber. A piece of Tb foil (Alfa Aesar, 99.9% purity) and ruby spheres were loaded into the sample chamber, the later used for pressure calibration [182].

3.6 Samples

3.6.1 $La_{1.875}Ba_{0.125}CuO_4$

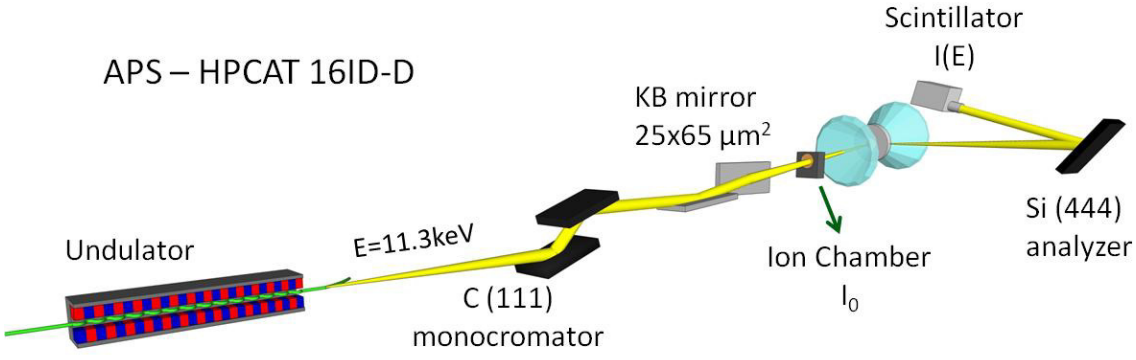

Figure 3.14: Tb Lγ experimental setup at 16-ID-D.

The $La_{1.875}Ba_{0.125}CuO_4$ single crystal was grown with the traveling-solvent floating-zone technique at Brookhaven National Laboratory by Dr. Genda Gu [70]. The sample slab was cut into small pieces and polished to achieve the desired thickness.

3.6.2 Y(RE) Alloys

Y(RE) alloys (RE = Pr, Gd, and Tb) were prepared at Washington University in St. Louis via arc-melting stoichiometric amounts of Y and RE (Y, Pr, Tb – 99.9% pure, Material Preparation Center of the Ames National Laboratory, Gd – 99.9% pure, Alfa Aesar). The alloys were re-melted several times to ensure dopant homogeneity with less than 0.1% of total mass loss.

3.6.3 Alkali Metals

Heavy alkali samples (99.95% pure) were obtained from Sigma-Aldrich. The samples were shipped in vacuum ampoules which were broken inside an argon filled glovebox where it was kept during the pressure cell loading. Between experiments the samples were stored in a vaccum chamber. The alkalis are very soft and reactive, thus samples used in the experiment were cut from the ingots, and promptly loaded into the pressure cells. Comparison between the use of commercial and distilled samples has shown that these display the same high pressure behavior [156].

Chapter 4

Results and Discussion

4.1 $La_{1.875}Ba_{0.125}CuO_4$

The emergence of static charge and spin ordered stripes in $LBCO_{1/8}$ is widely believed to trigger the strong T_c suppression observed at this doping. Such electronic ordering appears to be driven by electron-lattice coupling in the LTT phase [14]. A recent high-pressure experiment challenges this view as static stripe order is seen to persist to pressures higher than the required to induce the LTT to HTT structural transition [214]. We carried out high-pressure single crystal La K-edge polarized EXAFS and diffraction measurements in $LBCO_{1/8}$ in a diamond anvil cell to probe the relationship between the long range order, charge order, local CuO_6 tilts, and superconductivity. The majority of the results presented here are published in Ref. [17].

4.1.1 Polarized EXAFS and Local CuO_6 Tilts

The EXAFS technique measures the distances between the absorbing atom and its neighbors [65,215] (section 3.4.1). In $LBCO_{1/8}$, the three known structures (LTT, LTO, HTT) consist of different rigid rotations of the CuO_6 octahedra, leading to small changes in the Cu-O distances. On the other hand, CuO_6 rotations strongly distort the four in plane La-O distances (~0.15-0.2 Å) (Fig. 4.1), because the apical oxygens in the octahedra (O(2)) are located in the LaO_2 plane. However, La's first coordination shell displays nine different La-O bonds. XAFS measurements on powder samples average over all first neighbors La-O, reducing the sensitivity to the different tilt patterns. On the other hand, polarized EXAFS can be used to selectively

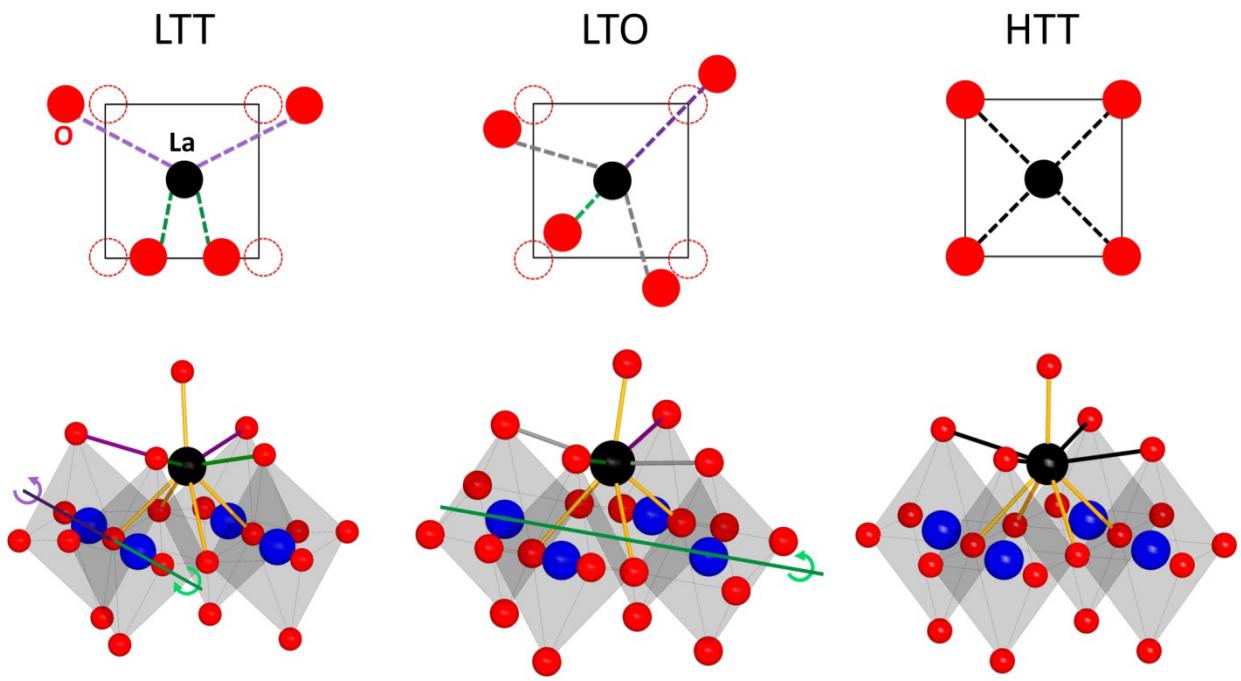

Figure 4.1: Local La environment in the different $LBCO_{1/8}$ phases. The CuO6 buckling along Cu-Cu (LTO) and Cu-O (LTT) directions (lower panels) distort the in plane La-O bonds (upper panels).

probe the in/out of plane components, leading to a large sensitivity to the nature of local tilts as previously demonstrated at ambient pressure [65].

4.1.2 Polarized EXAFS Modeling

Modeling the EXAFS data consists of assigning variable structural parameters to the different scattering paths. Despite the concomitant fitting of both polarizations, the exceedingly large number of scattering paths necessitates the use of constrains to reduce correlation between the parameters. Technically, the number of independent points in the spectra is taken as an upper limit for the number of parameters to be used [195]. The applied constrains to the modeling of each structure is discussed below.

4.1.2.1 - LTT Model

In the LTT structure, the nine first neighbor La-O bonds are split into six non-degenerate distances (Fig. 4.1): one La-O(2) bond that connects two LaO_2 planes (only seen in $\hat{c}$-polarized EXAFS), four in plane La-O(2) bonds split into two different distances (only seen in $\hat{a}$-polarized EXAFS) (see Fig. 4.1), two degenerate La-O(1) bonds and two different La-O(1') bonds (seen in both $\hat{c}$-and $\hat{a}$-polarizations). A single Debye-Waller factor parameter was assigned for all La-O bonds. The La-O(2) non-degenerate distances were varied independently (three in total). The CuO_2 plane is buckled around the [100] direction, splitting La-O(1/1') distances, these distances can be described as one average distance (two degenerate bonds), and two symmetric distortions about this average, leading to two parameters. The La-O(1) splitting at ambient pressure is ~ 0.05 Å, smaller then the EXAFS resolution in this experiment (~ 0.1 Å). Therefore, this splitting was set to its ambient pressure value.

4.1.2.2 - LTO Model

For the LTO model, the in-plane La-O(2) bonds display three non-degenerate distances, and the La-O(1) bonds two (Fig. 4.1). An average La-O(2) distance was set to the two degenerate bonds, and variable distortion of same amplitude but opposite sign was set for the remaining two distances. The La-O(1) bonds split by ~ 0.07 Å at ambient pressure, thus this splitting was irresolvable, and kept constant. A single Debye-Waller factor parameter was used for all La-O bonds.

4.1.2.3 - HTT Model

The HTT phase displays only three different La-O distances: one out of plane La-O(2), one in plane La-O(2) (four bonds), and one La-O(1) (four bonds) (Fig. 4.1). Thus one distance

parameter was used for each. Again, a single Debye-Waller factor parameter was fitted for all La-O distances.

4.1.3 Pressure Dependence of the Local Structure

The ambient pressure local structure is described by an LTT model (Fig. 4.2), as previously reported [63,65]. By monitoring the (100) superlattice Bragg peak intensity associated with the LTT structure, an LTT-HTT phase transition was observed around 1.7 GPa confirming previous findings that the long range symmetry above 1.7 GPa is HTT (Fig. 4.3).

Figure 4.4 displays fits to the 2.7 GPa data using the LTT, LTO, and HTT models. As previously discussed, the $\hat{e}||\hat{a}$ data is highly sensitive to the different CuO_6 tilting in the LTT and

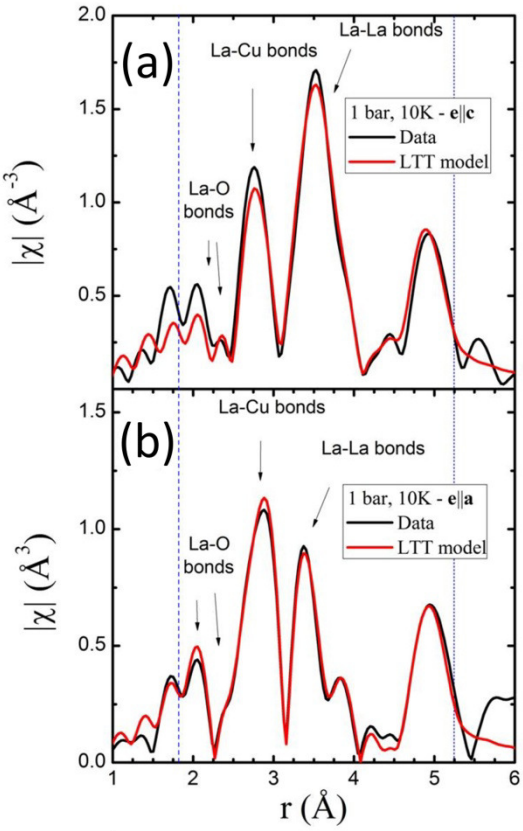

Figure 4.2: Fourier transform of the EXAFS spectra with the x-ray electric field align to the *c* axis (a) and *a* axis (b), and their modeling.

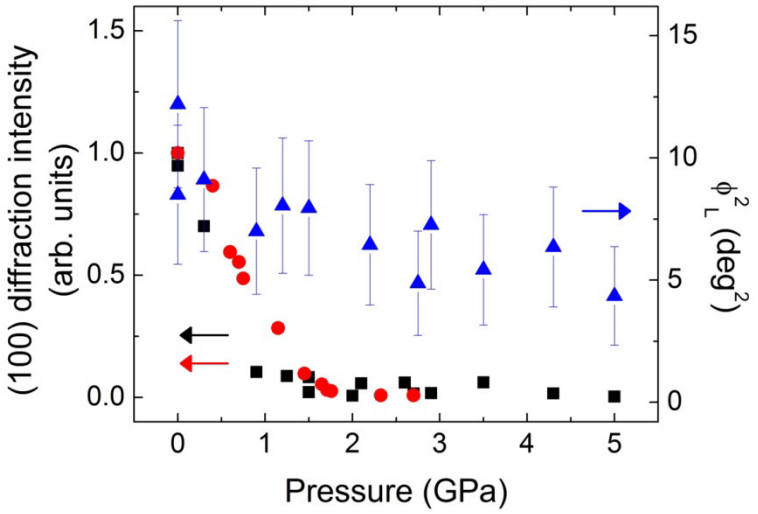

Figure 4.3: (100) intensity from this experiment (black) and previous results (red) [214]. In blue is the square of the CuO_6 tilt angle as measured by EXAFS.

LTO structures. It is clearly seen that the LTT model best describes the experimental data at 2.7 GPa, a pressure in which the long range structure displays HTT order. Furthermore, in the $\hat{e}||\hat{a}$ data the R-factor (misfit) for the La-O bonds is 4.3% for the LTT model, 8.9% for the LTO, and 13.6% for the HTT. The improved fit quality with the LTT model is best visualized by plotting the back Fourier transform of the $\hat{e}||\hat{a}$ data containing La-O(2) bonds (Fig. 4.4). Besides yielding worse fits, the LTO and HTT models lead to unphysical structural parameters, the former leading to a factor of two increase in the La-O(2) splitting, and the later resulting in a abrupt ~ 10 fold increase in the Debye-Waller factor (Fig. 4.5). All attempts of modeling the local structure with LTT/LTO/HTT mixtures failed, our results pointing to over 95% of LTT phase.

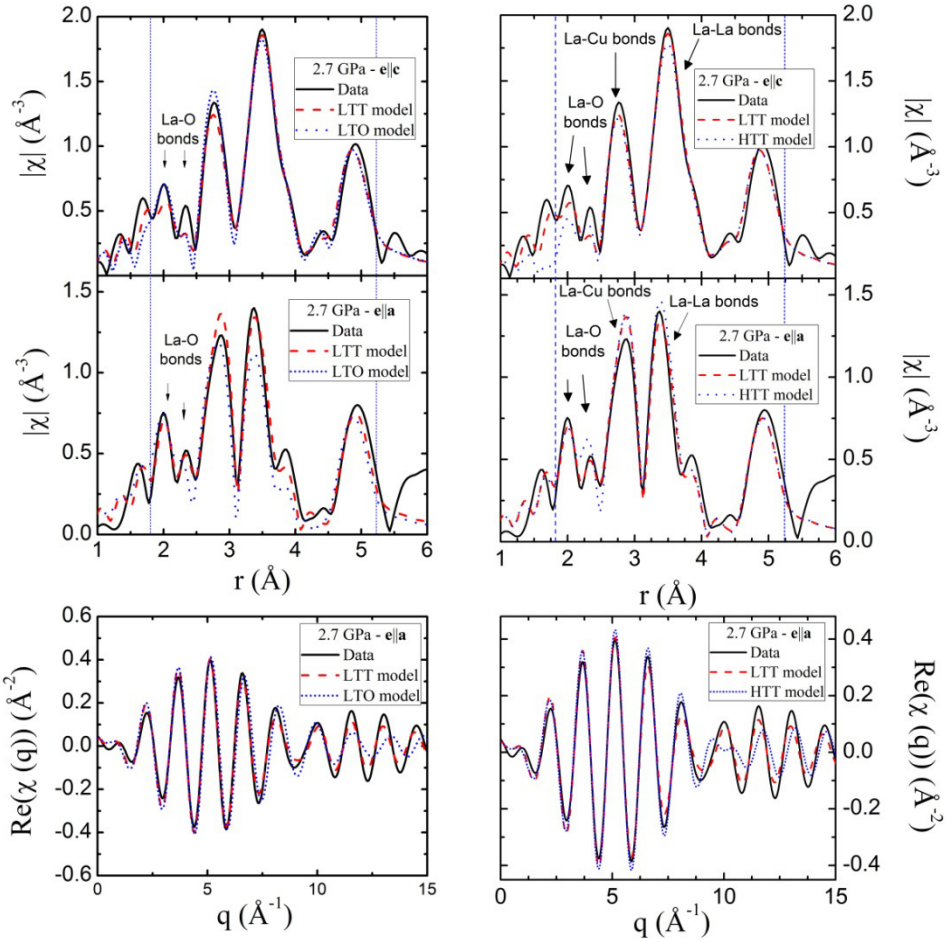

Figure 4.4: Fourier transform of the EXAFS data at 2.7 GPa. The LTT and LTO models are compared on the left, while the LTT and HTT are on the right. The back Fourier transform is displayed in the bottom.

The pressure dependence of the in plane La-O(2) distances in the LTT model is displayed in Fig. 4.6. Noticeably, the average of these distances measured by EXAFS and by diffraction (from lattice parameters) agrees remarkably well, being further evidence that the $LBCO_{1/8}$ high pressure local structure is properly described by the LTT model.

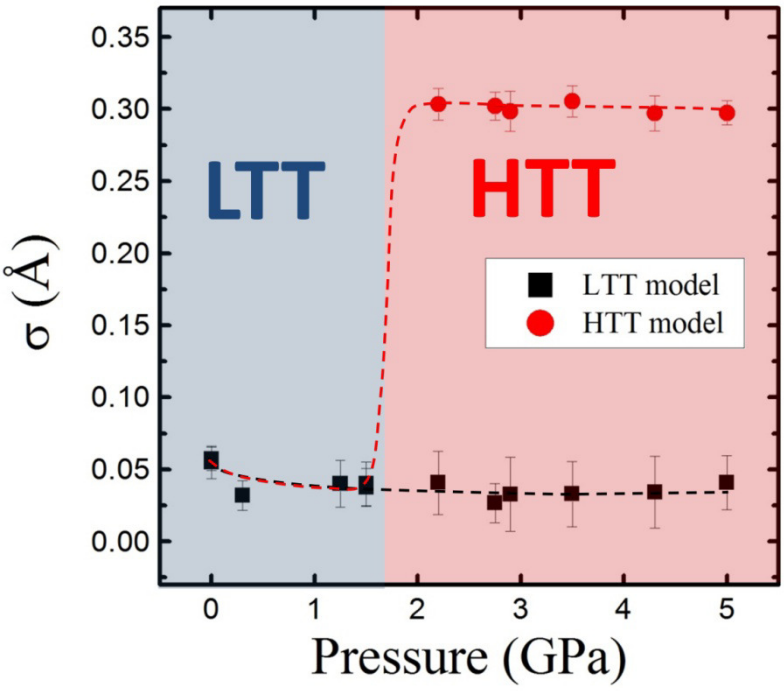

Figure 4.5: Debye Waller factor for La-O bonds obtained in fittings of LTT and HTT models.

Although present to the highest pressure measured (5 GPa), the LTT splitting reduces as a function of pressure (Fig. 4.6). While we cannot rule out local distortions other than rigid tilts causing the reduced La-O(2) splitting due to the limited spatial resolution in our experiment, previous high-pressure powder diffraction work on $La_{1.48}Nd_{0.4}Sr_{0.12}CuO_4$ (LNSCO) suggests a rigid reduction of the tilt angle with pressure driven by the larger compressibility of the rocksalt LaO_2 layer relative to that of the CuO_2 layer [216]. In fact, diffraction from (200) and (006) Bragg peaks points to a larger compressibility of the *a* axis (2.0(1) 10^{-3} GPa^{-1}) compared to the *c* axis (1.3(1) $10^{-3}GPa^{-1}$) (Fig. 4.7) as also found in LNSCO; thus a rigid rotation is likely to also take place in $LBCO_{1/8}$. It is known that the intensity of the (100) peak scales with the square of the macroscopic tilt angle, φ^2 [13,216–218]. Figure 4.3 shows that the reduction of the local φ^2_L

is not proportional to the (100) intensity. This is consistent with the presence of an order-disorder component to the pressure-induced LTT-HTT phase transition (i.e. $\varphi^2 \neq \varphi^2_L$).

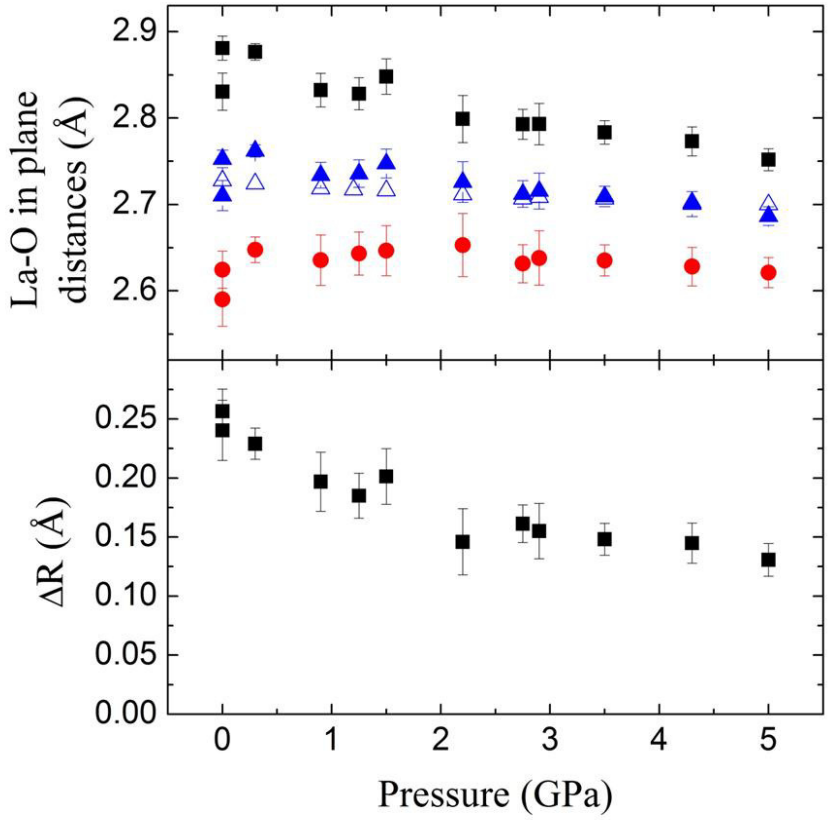

Figure 4.6: Top: Pressure dependence of in-plane La-O(2) distances (black and red). The average in plane La-O(2) distance measured by EXAFS (full triangles) is compared to the results derived from diffraction (open triangles). Bottom: Difference between La-O(2) distances as a function of pressure.

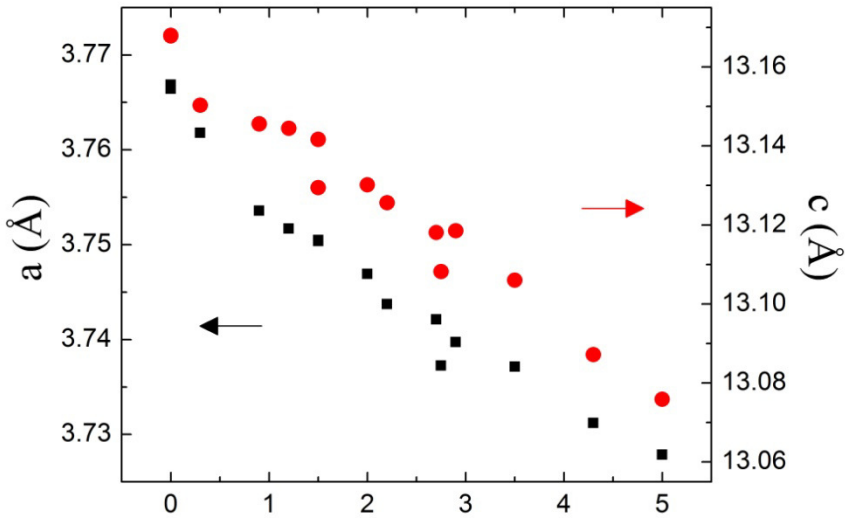

Figure 4.7: Lattice parameters determined by measuring (200) and (006) Bragg peaks

4.1.4 High Pressure LTT and Charge Order Domains

The relationship between the local LTT tilts and charge order (CO) was investigated at high pressure using single crystal diffraction. The (1.5 1.5 2) peak is allowed by both LTT and LTO phases. Its pressure dependence (Fig. 4.8) points to a suppression of intensity to ~ 1.7 GPa (note break in vertical scale), in agreement with the weaker (100) peak findings (Fig. 4.3). However, while the (100) intensity drops below the detection limit at the onset of the HTT phase, the (1.5 1.5 2) remains measurable. In agreement with previous findings, the LTT-HTT transition is followed by a severe broadening of the (1.5 1.5 2) peak. In fact, its correlation length matches that of the CO at high-pressure (~ 80 Å) as seen by the comparable peak width (Fig. 4.8 (b)). The presence of local LTT tilts, seen by EXAFS, is strong evidence that these domains display LTT symmetry. Further increase in pressure suppresses LTT and CO domains concomitantly (Fig. 4.8(c)). These results point to an intrinsic relationship between these two types of domains, indicating that CO is pinned by local LTT order.

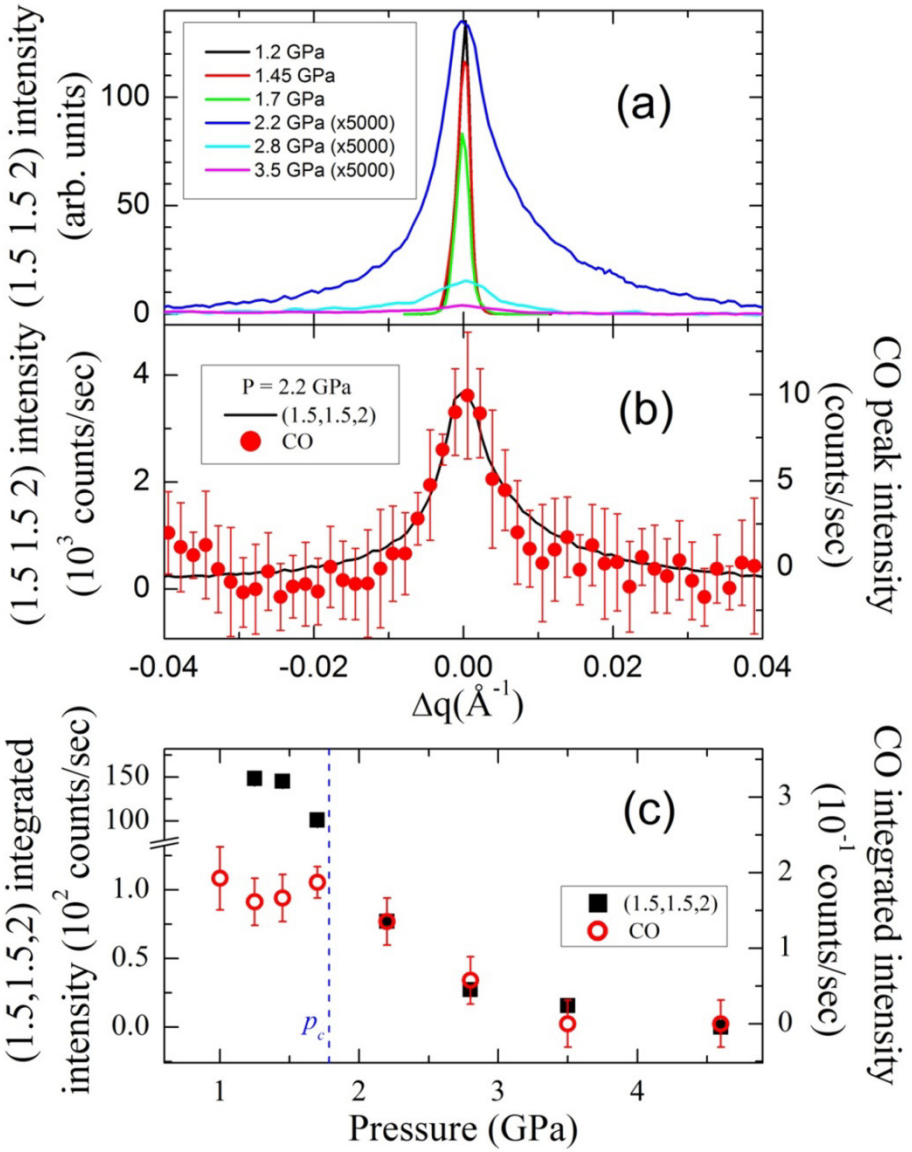

Figure 4.8: (a) (1.5 1.5 2) Bragg peak as a function of pressure. (b) The peak width (inversely proportional to the correlation length) of (1.5 1.5 2) and CO peaks match in the high pressure HTT phase. (c) The CO and (1.5 1.5 2) Bragg peak intensity display similar pressure dependence above the LTT-HTT transition.

4.1.5 Phase Diagram and T_c Pressure Dependence

Our measurements have established the presence of local LTT domains within the macroscopic high-pressure HTT phase. These results require an updated phase diagram (Fig. 4.9), which explicitly shows the intrinsic relationship between local LTT order and CO domains found here.

The simultaneous occurrence of LTT and CO domains with similar correlation lengths shows that local LTT order is sufficient to pin stripes. However, this result does not address the origin of the LTT tilts. The small LTT domains may persist by pinning at defects or due to small non-hydrostaticity, enabling CO to exist in the macroscopic HTT phase. On the other hand, the EXAFS data indicates that the local structure is mostly unchanged at the LTT-HTT structural boundary. Therefore, it is conceivable that CO forces the quenched LTT disorder to remain

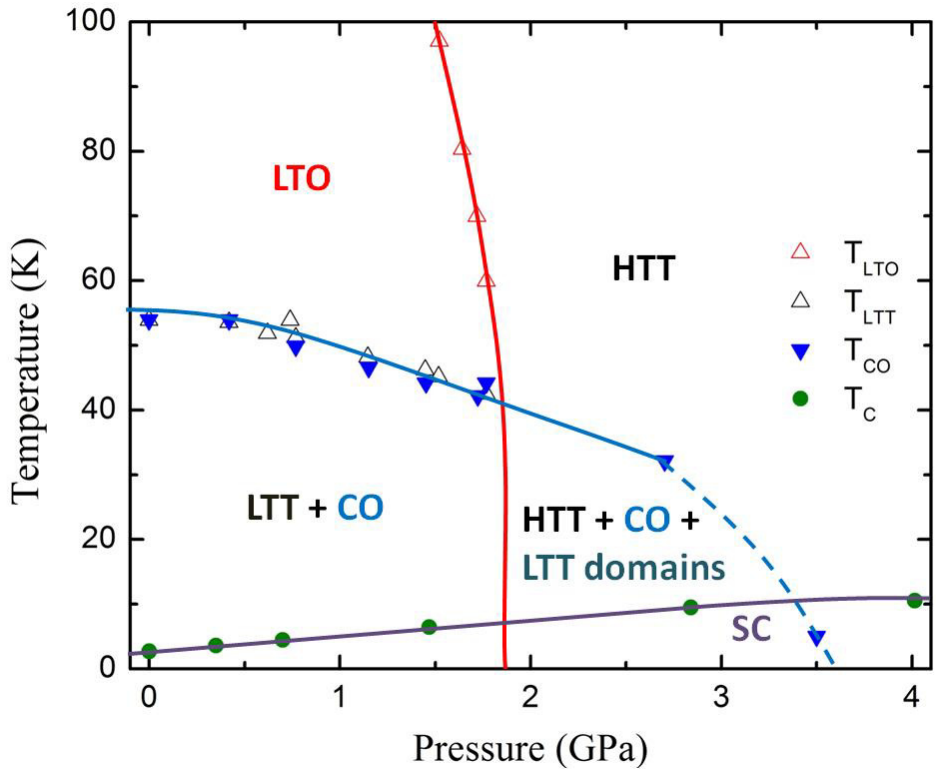

Figure 4.9: Updated phase diagram of $LBCO_{1/8}$. Includes data from Ref. [70].

present. In this scenario, the suppression of CO at high-pressure would drive the disappearance of LTT domains. Noticeably, the CO suppression starts at a similar pressure at which the sample becomes superconducting at 5 K (Fig. 4.9). Therefore, competition between CO and superconductivity may be responsible for such electronically driven suppression of LTT domains. This indicates the necessity of tracking the CO and LTT domains ordering temperature under pressure in order to understand their relationship with the emergent superconducting state.

At ambient pressure, the suppression of T_c at 1/8 doping is attributed to a frustrated Josephson junction coupling along the c axis [15,16,219]. While small pressure (< 3 GPa) increases the T_c of samples slightly away from 1/8 to nearly optimal values (T_c ~ 32 K), at 1/8 it remains suppressed to at least 15 GPa [214]. The current results indicate that, similarly to CO, superconductivity is unaffected by the LTT-HTT phase transition (Fig. 4.10), demonstrating that these electronic states are insensitive to the details of the long range structure. The suppression of

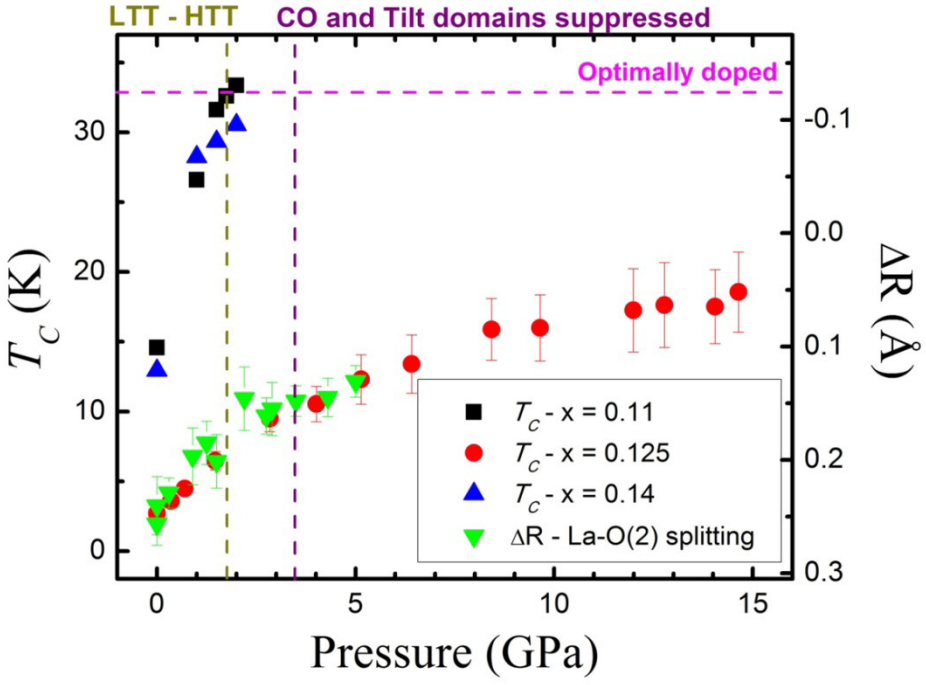

Figure 4.10: Relationship between T_c, La-O(2) splitting, and the suppression of CO.

measurable static CO domains is also insufficient to accelerate the enhancement of superconductivity. Remarkably, the T_c is observed to scale with the La-O(2) splitting (Fig. 4.10). Given the strong correlation between CO and LTT domains observed, the short ranged LTT tilt correlation appears to be sufficient to pin local CO, which locally retains the frustrated Josephson coupling, therefore controlling T_c(P). Similar measurements on dopings away from 1/8 are necessary to investigate the accuracy of this scenario.

4.1.6 Final Remarks

In this work, pressure was used to tune the electronic ground state of $LBCO_{1/8}$ while probing its structural and electronic ordering in the short and long range. It was demonstrated that the macroscopic structural order is decoupled to both CO and superconductivity, as these electronic states are unaffected by the long range LTT-HTT transition. On the other hand, CO is shown to be tightly bound to the presence of local LTT domains of same correlation length, and superconductivity appears to scale with the local LTT distortion. This result indicates that superconductivity and charge ordering observed in many cuprates are connected to the short/medium structural order, pointing to the necessity of investigating the structural motif at the appropriate length scale.

Finally, the proximity of magnetic ordering and superconductivity in high-T_c compounds has triggered many suggestions that electron pairing in these materials is driven by magnetic fluctuations, such as stripes [1,56]. Both EXAFS and diffraction are femtoseconds probes. Therefore, the current result is unable to determine the timescale of the CO, LTT domains, and local LTT tilts in the high-pressure phase $LBCO_{1/8}$. Investigating the evolution of spin fluctuations with pressure and its relationship with the emergent superconductivity is desired.

4.2 Lanthanides

The 4*f* level in heavy lanthanides is atomic-like at ambient pressure. It contributes to Fermi surface properties by spin polarizing the conduction electrons via exchange interaction [71]. Upon increased pressure, the reduced volume is expected to broaden the 4*f* states and bring them closer to the Fermi level. The enhanced interaction between the 4*f* level and the Fermi surface is theoretically challenging, and expected to trigger a plethora of novel ground states [41,91,220]. In particular, the high-pressure volume collapse observed in many lanthanides may signal the onset of 4*f*-conduction electron hybridization (Kondo interaction) and/or direct 4*f*-4*f* interaction. In this work a combination of x-ray spectroscopies and transport measurements on pure lanthanide metals, and their dilute magnetic alloys with Y are used to investigate the volume collapse transition in Gd (59 GPa [221,222]) and Tb (53 GPa [123]). Most of the results presented here are published in Ref. [18].

4.2.1 On the Promotional, *s*→*d* Transfer and Mott Models

Both promotional model and *s*→*d* transfer models explain the volume collapse through changes in electronic occupation (4*f* and 5*d* respectively) (see section 2.2.2). Consequently, these models can be investigated by XANES L_3 measurements. In Fig. 4.11 the pressure dependence of the Tb L_3 edge XANES is displayed, while similar Gd data is available in the literature [124]. This absorption edge is dominated by the dipolar $2p_{3/2}$→5*d* excitation, thus the observed pressure-induced suppression of the white line (main peak above the absorption threshold) observed in both lanthanides indicate a concomitant increase in *d* occupation in both cases (absorption edge depends on density of empty 5*d* states, see section 3.4.2). On the other hand, a change in 4*f* occupation would result in a shift of the L_3 absorption edge by ~ 10 eV [207–209].

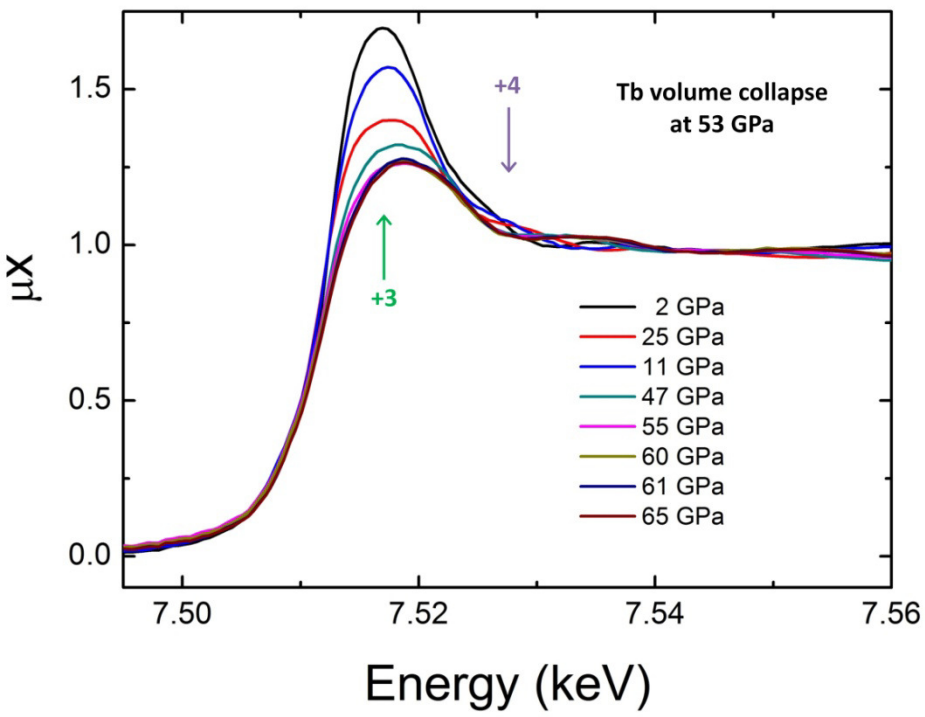

Figure 4.11: Pressure dependence of the Tb L_3 XANES. The +3 and +4 arrows correspond to the position of the white line for the different valence states.

This would be marked by a shift into location of the 4+ arrow shown in Fig. 4.11, which clearly does not occur to the highest pressure measured. Therefore, the XANES data for both Gd and Tb are inconsistent with the promotional model. Our data is in agreement with the continuous pressure induced *s*→*d* transfer that takes place under pressure in these lanthanides, that is known to be responsible for their multiple high pressure structural phase transitions [79]. Noticeably, Tb's white line stops changing after the volume collapse (Fig. 4.11), in contrast with the apparent continuous suppression seen in Gd [124]. Although the L_3 edge data are consistent with an *s*→*d* electron transfer volume collapse picture, there is no clear evidence that this mechanism is the only one possible.

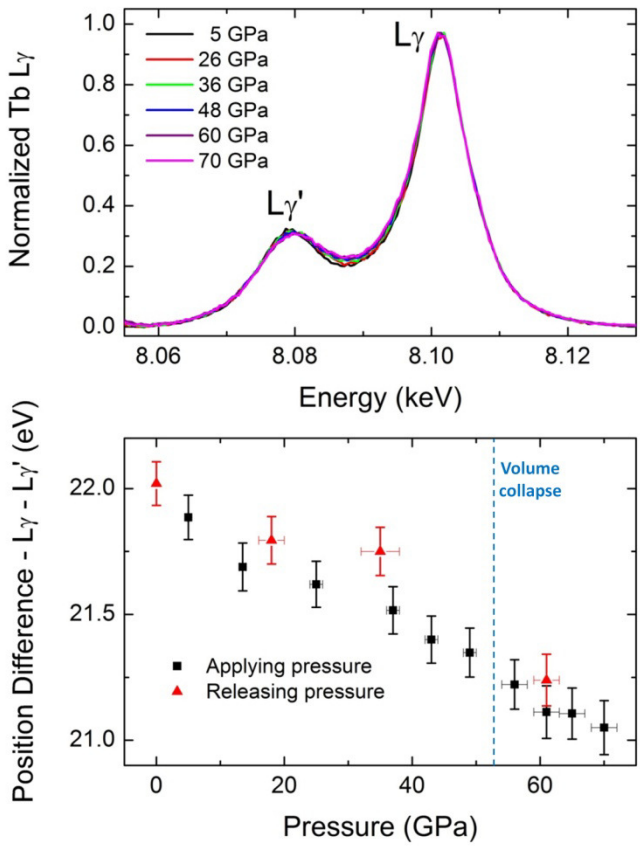

Figure 4.12: Top: pressure dependence of Tb Lγ. Bottom: position difference between Lγ and Lγ' as a function pressure.

In the Mott model, the volume collapse is driven by a transition into a 4*f* band (see section 2.2.2). The nature of the localized 4*f* moment can be probed by non-resonant Lγ x-ray emission spectroscopy [120,125]. The splitting of the Lγ line is related to the exchange interaction between the 4*f* and excited 4*d* states. A Mott transition, which delocalizes the 4*f* states, would lead to a much reduced 4*f*-4*d* overlap and exchange interaction, mostly suppressing the splitting. Fig. 4.12 displays the pressure dependence of the Tb Lγ emission. Similar data for Gd has been published [125]. The results for Tb and Gd clearly show a persistent Lγ splitting across their volume collapses (at 53 and 59 GPa, respectively), demonstrating that the 4*f* level in Gd and Tb

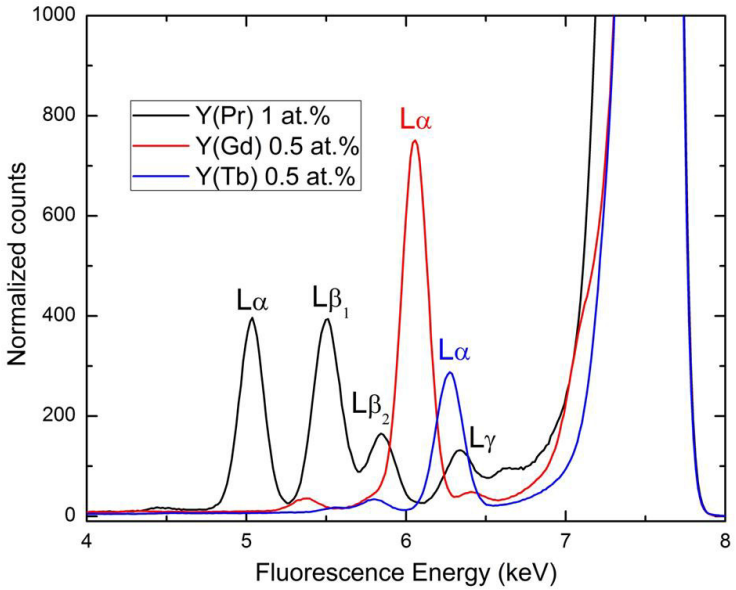

Figure 4.13: Fluorescence spectra of Y(Pr), Y(Gd), and Y(Tb) at ambient pressure and room temperature. The labels display the nominal concentrations.

remains localized, and invalidating the Mott model. However, the high-quality data obtained for Tb shows a small and continuous shift in of the Lγ' shoulder towards larger energy (~ 5% of the total splitting) (Fig. 4.12). Unfortunately, the noise level in the Gd data incapacitates a detailed comparison, hampering the ability to understand this phenomenon. Interestingly, recent high-pressure Lγ experiments in Eu collected by Dr. Wenli Bi do not display such shift [223]. Therefore, we speculate that the observed shift occurs due to pressure enhancement of crystal fields, which would slightly reduce the strength of the local $4f^8$ moment of Tb, but would not affect the half-filled Eu $4f^7$ [210].

4.2.2 T_c(P) in Y(RE) Alloys and the Kondo Model

As discussed in section 2.2.1, the emergence of Kondo interactions in magnetic impurities alloyed into superconducting hosts is expected to strongly suppress the superconducting

transition. Therefore, further insight into the volume collapse transition of Gd and Tb was obtained from resistivity measurements of the superconducting T_c on Y(0.5 at.% Gd) and Y(0.5 at.% Tb) at high pressures.

4.2.2.1 - Y(RE) Alloys Characterization

To ensure the quality of the alloys produced, x-ray fluorescence and EXAFS measurements were performed. Fig. 4.13 displays the fluorescence spectra from the three alloys used in this thesis. The incident photon was set to 7.55 keV, which lies between the L_3 ($2p_{3/2} \rightarrow 5d$ excitation)

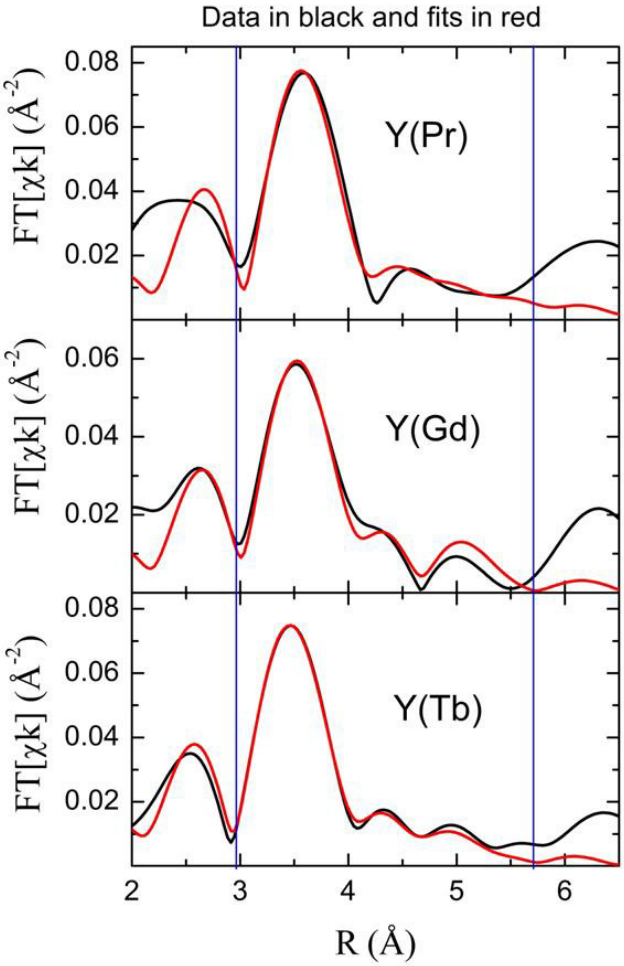

Figure 4.14: Fourier transform of the EXAFS L_3 edge spectra Pr, Gd, and Tb dopants in Y(Pr), Y(Gd), and Y(Tb) alloys.

and L_2 ($2p_{1/2} \rightarrow 5d$) edges for Gd and Tb, but above both edges for Pr. The $2p_{1/2}$ excitation leads to the extra $L\beta_1$ and $L\gamma$ lines observed, and the absence of the $L\beta_2$ emission line in Gd and Tb is due to its overlap with the strong elastic scattering peak (E = 7.55 keV). The presence of dopants in the alloys is evident by the element specific emission lines observed.

The element specificity of EXAFS turns it into a great tool to investigate the local structural around dopants [195]. The Fourier transformed EXAFS spectra for the Y(RE) alloys are shown in Fig. 4.14. Attempts to model the data with first neighbor RE-Y and RE-RE bonds were performed. The results indicate that the RE-RE fraction was zero within the experimental error (~ 5%), demonstrating the absence of RE clusters in the alloy. Furthermore, the measured RE-Y distances indicate that the RE impurity distorts the local environment to retain its atomic size (see Table 4-1).

Table 4.1: Y-RE distances measured with EXAFS are compared to RE-RE distances obtained by diffraction in pure RE metals [224]. Y-Y distance in pure Y metal is 3.6474 Å [224].

RE	XAFS (Å)	Diffraction (Å)
Pr	3.65(2)	3.6725(7)
Gd	3.62(2)	3.6360(9)
Tb	3.59(1)	3.6010(3)

4.2.2.2 – Conduction Band Equivalency between the Alloys and Pure Lanthanides

Mapping the results obtained in RE alloys into the pure lanthanides is a potential challenge due to the different structural and electronic environment that the lanthanide ion experiences in the dilute or concentrated cases. In order to minimize the effect of the environment the choice of superconducting host is critical.

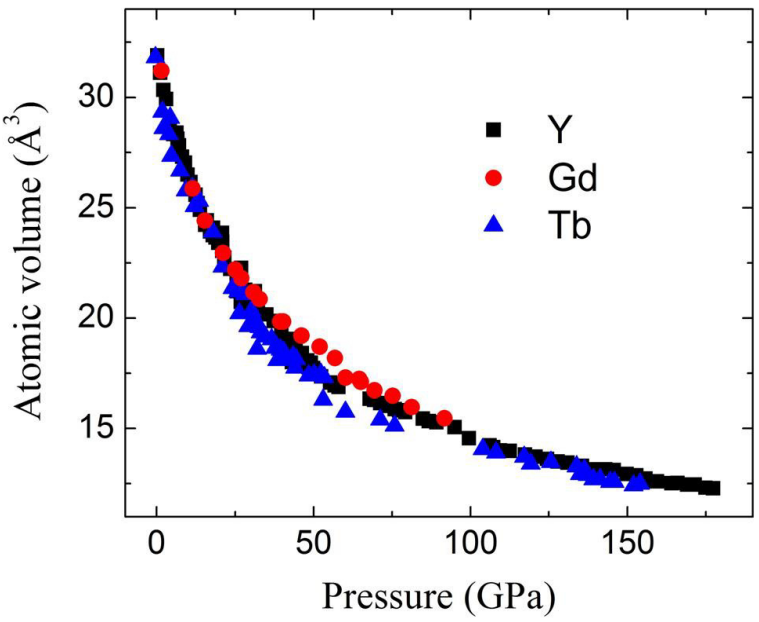

Figure 4.15: Atomic volume pressure dependence of Y [127,227], Gd [221], and Tb [123].

Yttrium is a light rare earth that superconducts above 30 GPa [135,225,226]. That T_c monotonically increases with pressure, reaching a maximum ~ 20 K at ~ 110 GPa [226], greatly facilitates the comparison with results from the alloys. Y also displays a strikingly similar atomic volume at ambient and high pressures (Fig. 4.15), therefore facilitating homogenous mixing in the alloys. Furthermore, Y displays the same set of pressure induced phase transitions as Gd and Tb, except for the presence of an fcc phase in Gd [221]. Finally, Y has three valence electrons ($5s^2 4d^1$), displaying a very similar conduction band to the heavy lanthanides, a fact that is corroborated by the observed $s \rightarrow d$ transfer driven phase transitions at high pressure [127,227].

That Y is indeed a great choice of superconducting host is evidenced by the results from the EXAFS measurements at ambient pressure (Table 4.1). A clear lanthanide contraction is observed in the RE-Y distances of the Y(RE) alloys with increasing atomic number. This contraction occurs because the additional 4*f* electron in heavier lanthanides poorly screens the extra nucleus charge, leading to an increased attraction between the nucleus and the outer *spd*

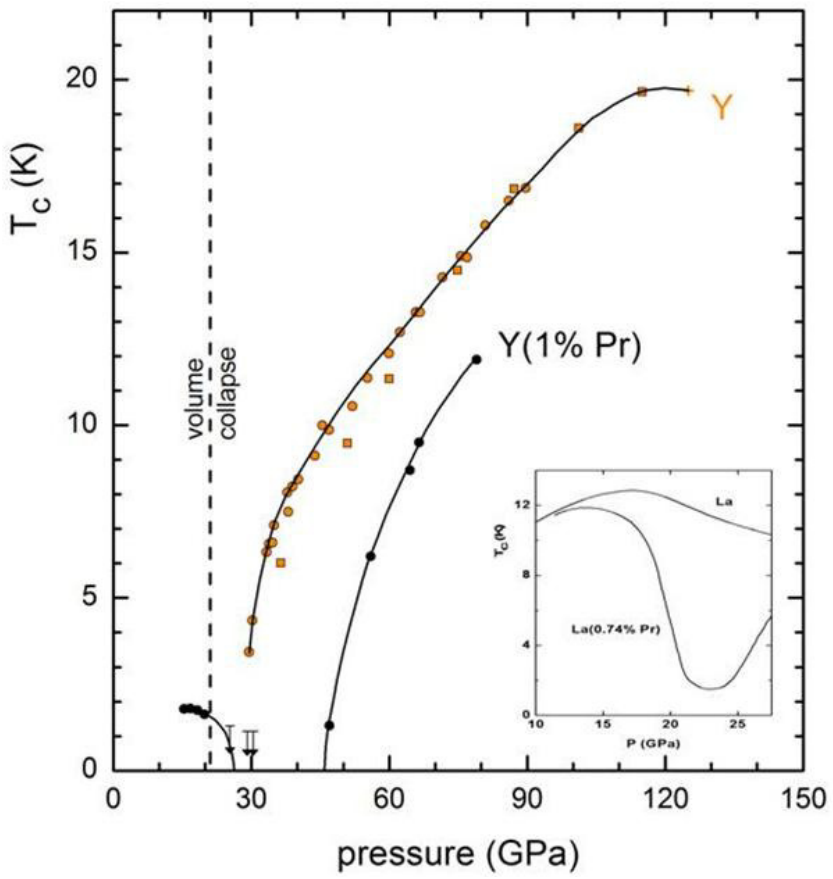

Figure 4.16: Pressure dependence of T_c in Y(1 at. % Pr). Inset: La(Pr) T_c pressure dependence extracted from [228].

valence electrons. The remarkably similar lanthanide contraction observed in Y(RE) and the pure metals (see Table 4-1) is strong evidence of their similar conduction band, thus justifying the mapping of results on the interaction between conduction electrons and local moments obtained from electrical resistivity measurements in the Y(RE) alloys to their pure RE metal counterparts.

4.2.2.3 – Y(RE) T_c(P) and the Kondo model

In order to validate the method to be employed in the study of Gd and Tb, resistivity measurements were performed in Y(1 at.% Pr) by Prof. Takahiro Matsuoka from Gifu University in Japan while visiting Prof. Schilling's group. The effect of Pr doping on the T_c(P) of La(Pr) and

Y(Pr) alloys has been previously investigated [228]. However, these experiments did not achieve high enough pressures (~ 25 GPa) for T_c fully recover (see inset of Fig. 4.16). The present data are displayed in Fig. 4.16. Pr's volume collapse triggers a strong suppression of T_c, driving it below 1.5 K at 27.5 GPa. Remarkably, superconductivity is strongly recovered starting at ~ 58 GPa, exactly the behavior expected as the Kondo temperature (T_k) achieves high enough values to trigger the spin shielding of the local moment.

A positive 4*f*-conduction band exchange interaction is expected to occur in heavy lanthanides at low pressures due to the strongly localized nature of 4*f* electrons. Therefore, a reduction in Y's T_c is expected within AG theory (see section 2.2.1). This is precisely the behavior observed for

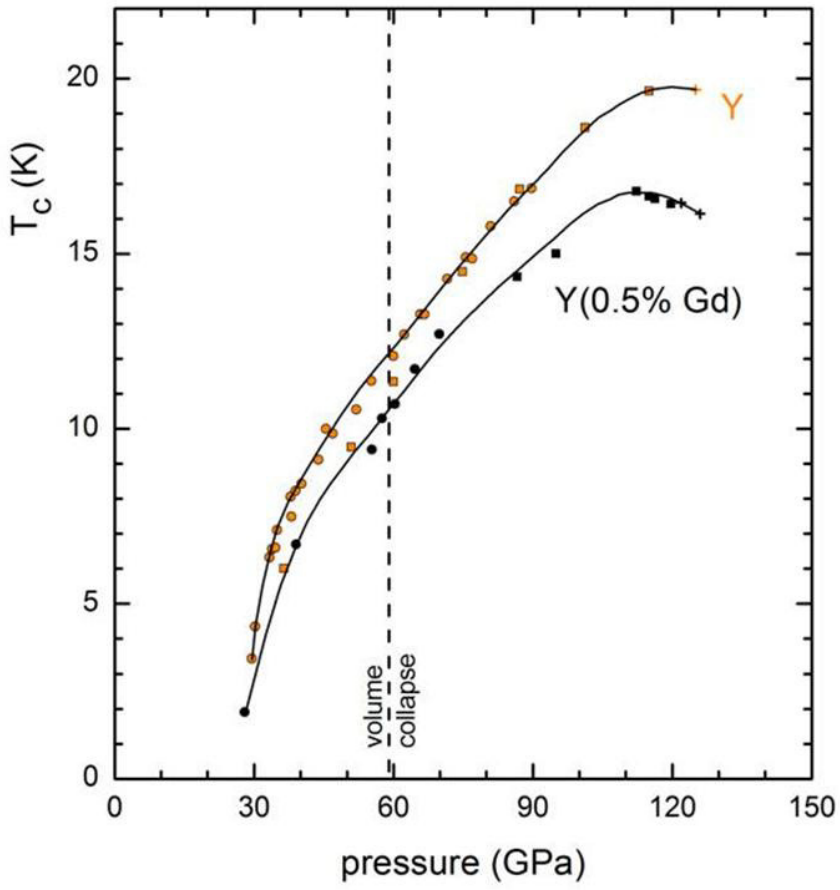

Figure 4.17: Pressure dependence of T_c in Y(0.5 at. % Gd) alloy.

the Y(Gd) sample throughout the measured pressure range (Fig. 4.17). Particularly, no discontinuity is observed across Gd's volume collapse, demonstrating that its 4*f* level is unperturbed across this transition.

In contrast, T_c(P) for Y(Tb) drastically deviates from that of pure Y across Tb's volume collapse pressure (Fig. 4.18). The non-hydrostaticity inherent to this resistance setup leads to a pressure gradient across the sample. At a given pressure, a large $dT_c(P)/dP$ will broaden the superconducting transition in the resistance temperature dependence, while if $dT_c(P)/dP \sim 0$, the transition will be sharp. Therefore, the much sharper transition observed at higher pressures (inset Fig. 4.18) confirms the remarkably constant T_c(P) behavior above ~ 55 GPa (Fig. 4.18).

The Lγ XES experiment demonstrated that Tb's local moment is preserved to at least 70 GPa. Therefore, the suppression of T_c in Y(Tb) across Tb's volume collapse is strong evidence that the magnitude of the 4*f*-conduction band exchange interaction (J) in Tb is increasing around its volume collapse. An enhanced positive J (J_+) would lead to a stronger suppression of T_c through the AG mechanism [102]. Such increase could occur through enhanced spatial overlap between the 4*f* and conduction band wavefunctions. However, it is very unlikely that such enhanced overlap would occur in Tb and not in Gd as their conduction bands and 4*f* radial distributions are very similar [77]. On the other hand, an enhanced negative J (J_-) would suppress T_c within the MHZ mechanism [106–108] (see section 2.2.1). J_- is controlled by the 4*f*-conduction band hybridization. The closer proximity of Tb's $4f^8$ state to the Fermi level compared to Gd's $4f^7$ (~ 3 eV vs. ~9 eV, respectively) makes the former much more likely to exhibit 4*f*-conduction band hybridization, thus explaining the suppression observed in Tb but not in Gd. Furthermore, the extensive work on Ce and Pr, points to a tendency of pressure driving 4*f* levels into instability within a Kondo picture.

Unfortunately, no evidence of Kondo minima was observed in any experiment performed here. This is likely due to the typically small minima size coupled to the largely non-hydrostatic measurement. Furthermore, the emergence of superconductivity hampers the ability to observe the Kondo minima. Despite the existence of robust circumstantial evidence pointing to the emergence of Kondo interaction in Tb above its volume collapse, further experiments are necessary to verify this result.

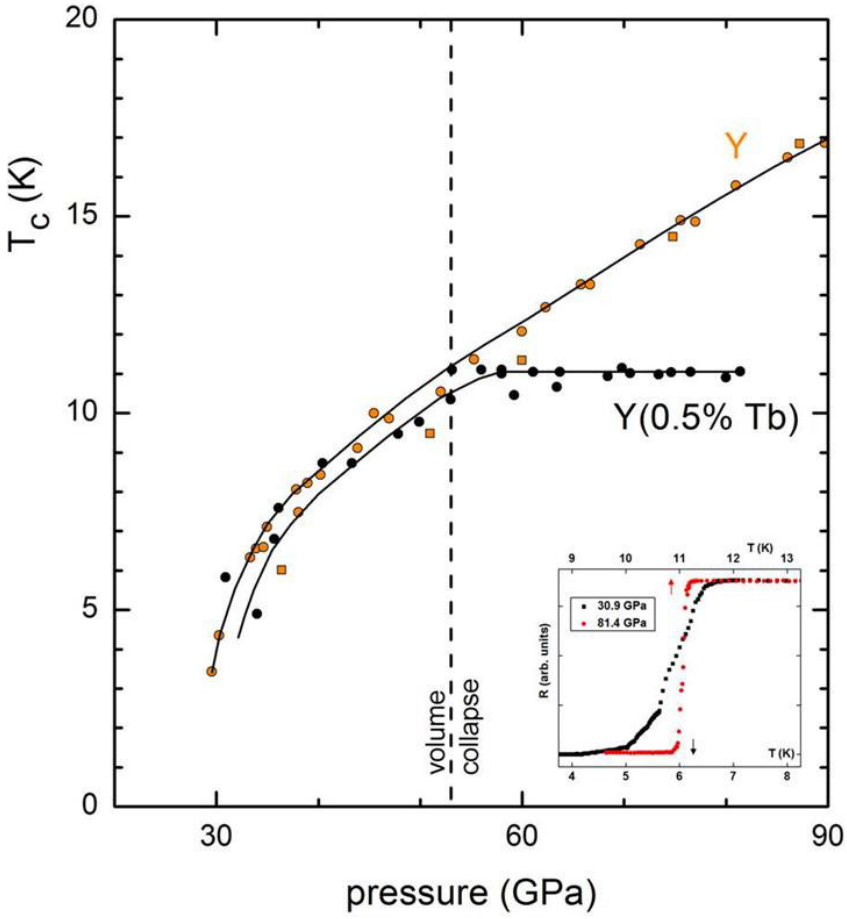

Figure 4.18: Pressure dependence of Tc in Y(0.5 at.% Tb). Inset: Resistance temperature dependence at 30.9 and 81.4 GPa.

4.2.3 Final remarks

The emergence of Kondo interactions across Tb's volume collapse is evidence that the Kondo model at least in part explains this transition, while in Gd this transition is independent of the 4*f* state. However, it is unlikely that such similar volume collapse transitions in these neighboring lanthanides in the periodic table would have very distinct origins. Noticeably, the trend observed in Fig. 4.19 points to a larger transition pressure but smaller volume collapse size the heavier the lanthanide. This trend is only broken in Tb. Therefore, we speculate that an *s*→*d* volume collapse in Tb is further aided by the onset of Kondo interactions.

Although the details of the mechanism driving the volume collapse transition remains to be solved, this work pioneers in demonstrating the presence of electronic instabilities in Tb's 4*f*

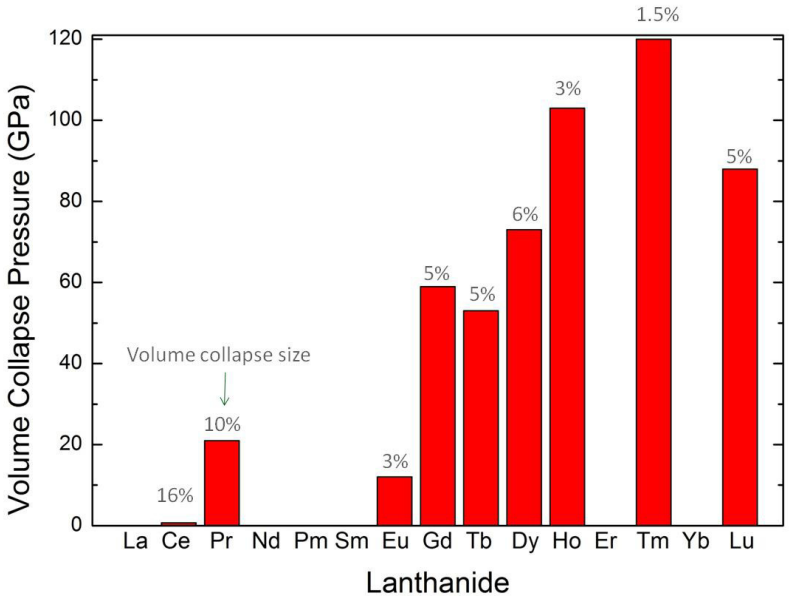

Figure 4.19: Diagram of the volume collapse observed in lanthanides [111,112,123,221,222,240–245].

state above its volume collapse. Later experiments by Ph.D. candidate Jinhyuk Lim demonstrated the presence of similar instabilities in Dy across its volume collapse [229]. The departure of the very robust 4*f* level in heavy lanthanides from the atomic-like picture with pressure presents a great opportunity to investigate the consequences of mixing such localized states into the conduction band. In fact, J. Lim has started such investigations by probing the magnetic ordering of heavy lanthanides at high pressures [128]. A remarkable increase in the magnetic ordering temperature (T_o) was observed in Tb and Dy above ~ 70 GPa. In Dy T_o lies above room temperature for pressures above ~ 120 GPa, being the largest transition temperature ever observed in a pure lanthanide. It is argued that the enhanced magnetic ordering occurs through the conversion of Tb and Dy into Kondo lattice systems at extreme pressures [128]. Within this model, the strengthening of J_- should initially enhance magnetic ordering, scaling as $|J_-|^2$. A further increase in J_- is expected to lead to a competition between magnetic ordering and the ever growing Kondo screening that scales as $e^{\frac{-1}{N(E_F)|J-|}}$, leading to the collapse of magnetic ordering and screening of the local moment [88,90]. This quantum phase transition has been argued to favor exotic ground states such as unconventional superconductivity [100,220].

4.3 Alkali Metals

The nearly free electron model that describes the alkali metals very well at ambient pressure has been argued to break down at moderate pressures [23–25]. Despite great interest in understanding the emerging electronic correlations, little experimental work has been done to investigate their ground state, and those were mostly focused on Li's superconductivity [138,139,144]. Motivated by the recent theoretical prediction of a high-

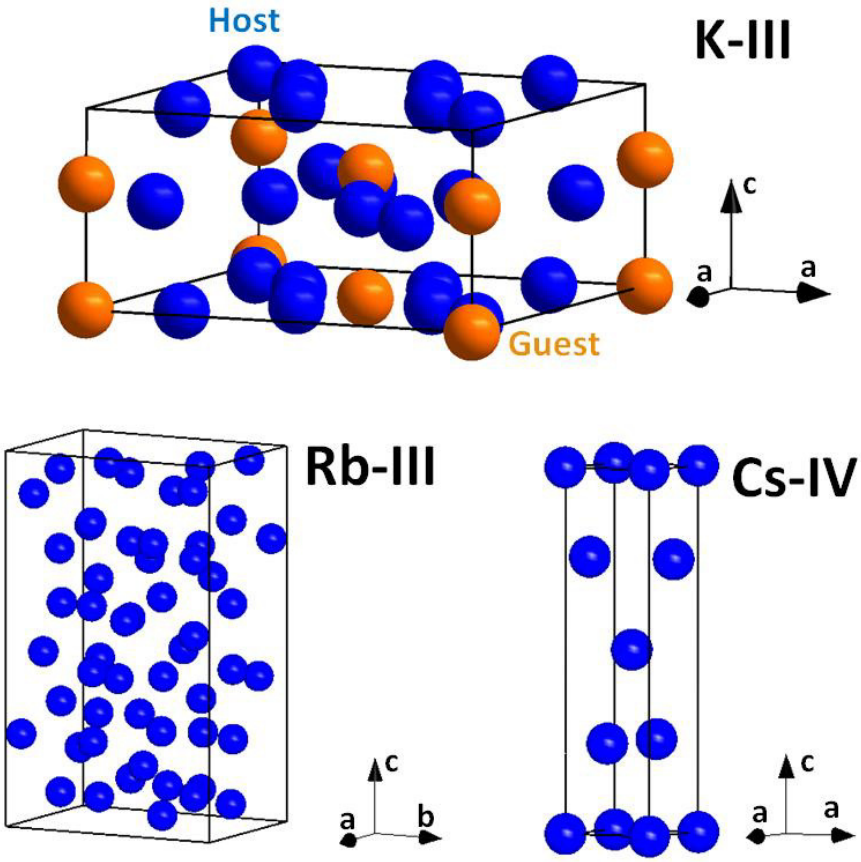

Figure 4.20: K, Rb, and Cs Post-fcc structures at 10 K

pressure magnetic ground state in K [148], we studied the structural and electronic ground state of K, Rb, and Cs with x-ray powder diffraction and XANES.

4.3.1 Low Temperature Structures

4.3.1.1 – Potassium

Potassium's structural phase transitions are clearly observed by the appearance/suppression of diffraction peaks (Fig. 4.21). The bcc to fcc transition is observed at 13±1 GPa, while K-III phase is stable above 21±2 GPa. No bcc/fcc coexistence was observed; at 20.8 GPa the fcc/K-III phases were observed to coexist.

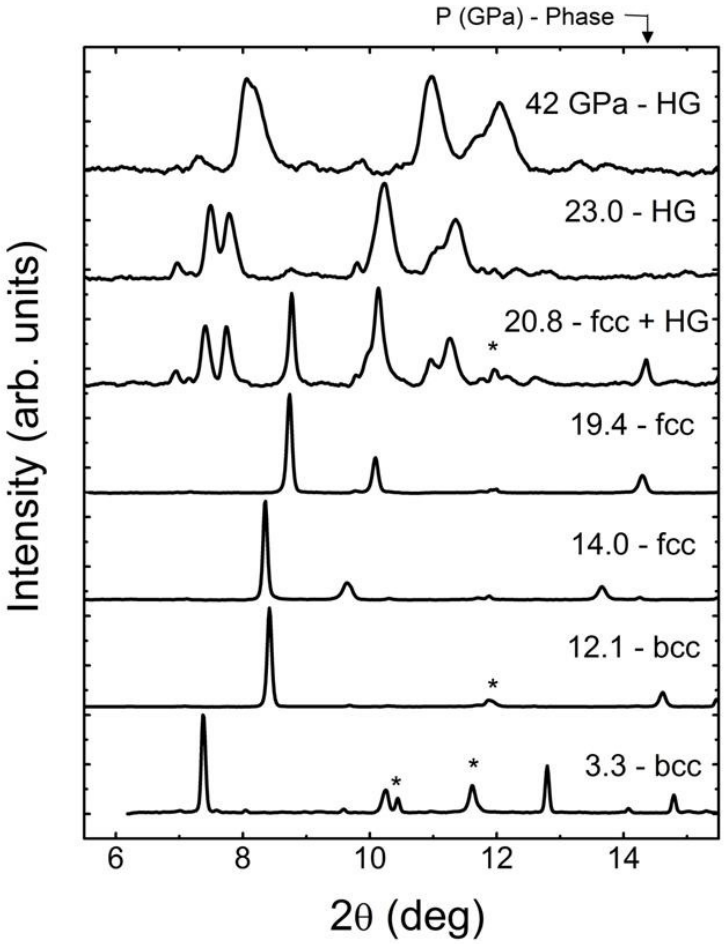

Figure 4.21: K diffractogram pressure dependence.

K-III phase is a complex host/guest structure (Fig. 4.20) [156]. Host structure (*I4/mcm* space group) reflections are observed at low temperature, but only one reflection from the guest phase (C-centered tetragonal) is seen at $2\theta \approx 8.7°$. The much weaker guest phase peaks is consistent with room temperature data [156,160], likely occurring due to the smaller number of atoms in this phase (~ x5 less than the host phase) and the larger disorder in this sublattice [156]. Attempts to reproduce the diffractogram with other known alkali phases failed, further indicating that the observed phase is the incommensurate K-III.

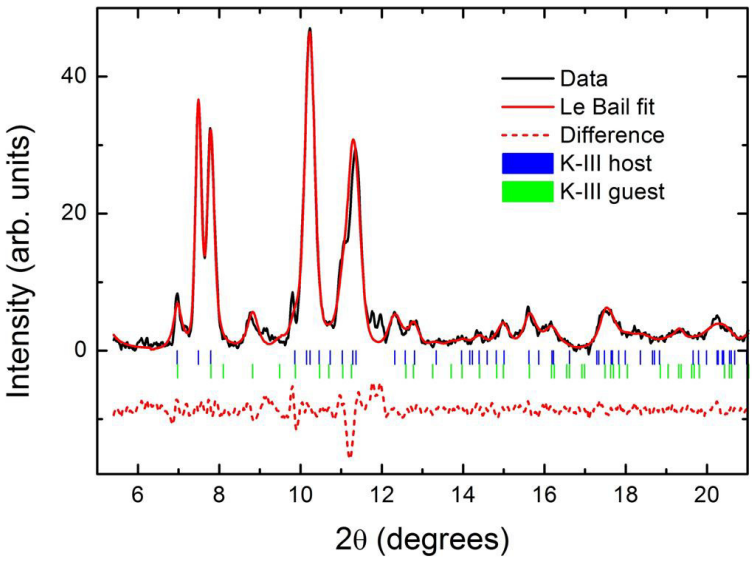

Figure 4.22: Le bail fit of the 23 GPa data of K.

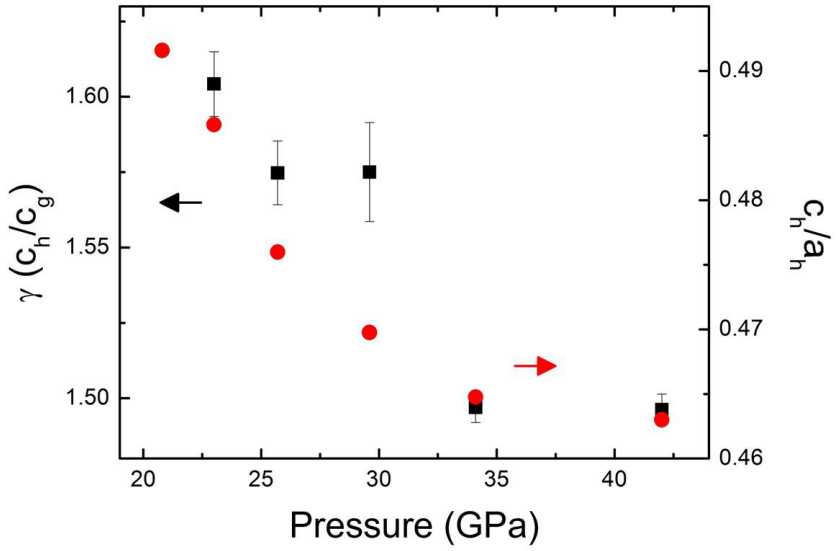

Figure 4.23: Pressure dependence of γ and c/a ratio of the Host/Guest K-III phase.

Although the current data quality is insufficient to verify the guest structure transitions observed at room temperature [160], c_h/a ratio and γ (= c_h/c_g) display a minima above 35 GPa

(Fig. 4.22) consistent with the behavior observed at room temperature at the onset of K-IIIb phase, indicating that the same transition may occur at low temperature.

The crystal structures predicted to be magnetic in K between 18.5-22 GPa are different from those observed at room temperature [22,148]. These phases were also not observed in this experiment at 10 K (Fig. 4.24). Nevertheless, if the predicted magnetic phases are ignored, DFT correctly finds K-III as the ground state above 20 GPa [148].

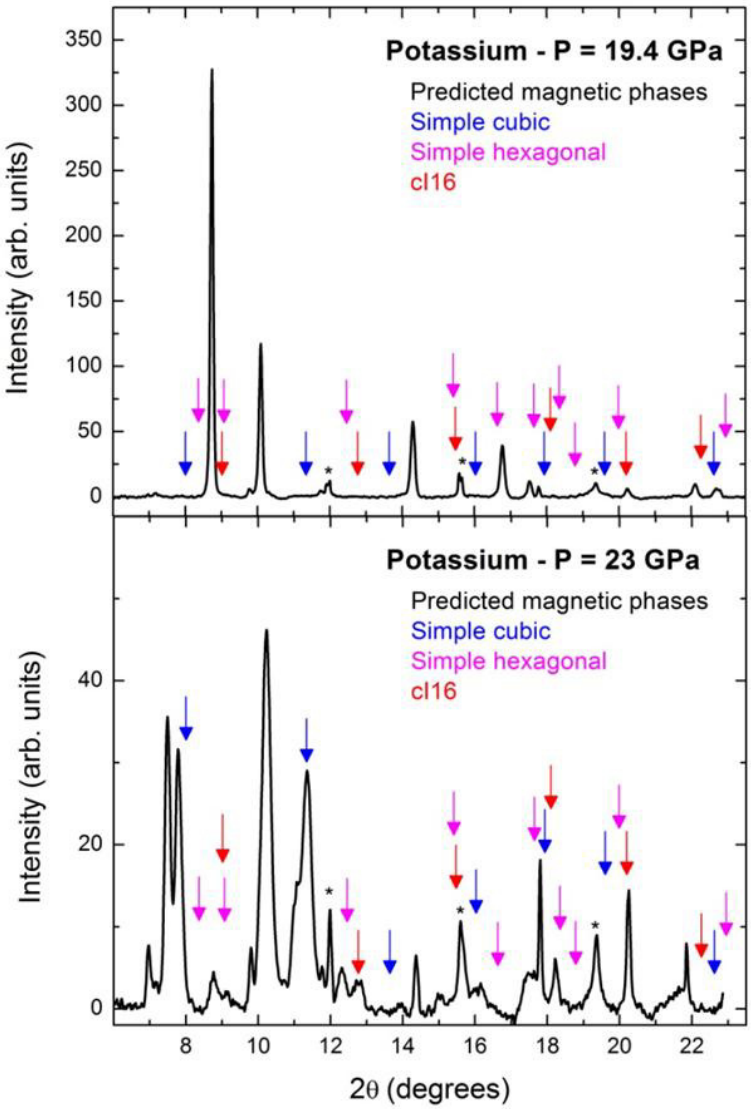

Figure 4.24: K diffractogram at 19.5 and 23 GPa compared to the predicted magnetic structures [148].

4.3.1.2 - Rubidium

The bcc to fcc transition in rubidium at low temperature occurs at 8.9±1 GPa. Rb-III (*oC*52) phase is stable above 15.7±1 GPa, with fcc/Rb-III coexistence seen at 15.7 GPa (Fig. 4.25). Rb-III is observed to the highest pressure measured of 24.5 GPa, surpassing the stability range of Rb-IV and Rb-V observed at room temperature [22] (see Fig. 4.30).

The *oC*52 structure ($C222_1$ space group) is remarkably complex; its 52 unit cell atoms are distributed between seven inequivalent sites, and the structural refinement at room temperature was only possible through single crystal diffraction [156]. Such low symmetry allows an

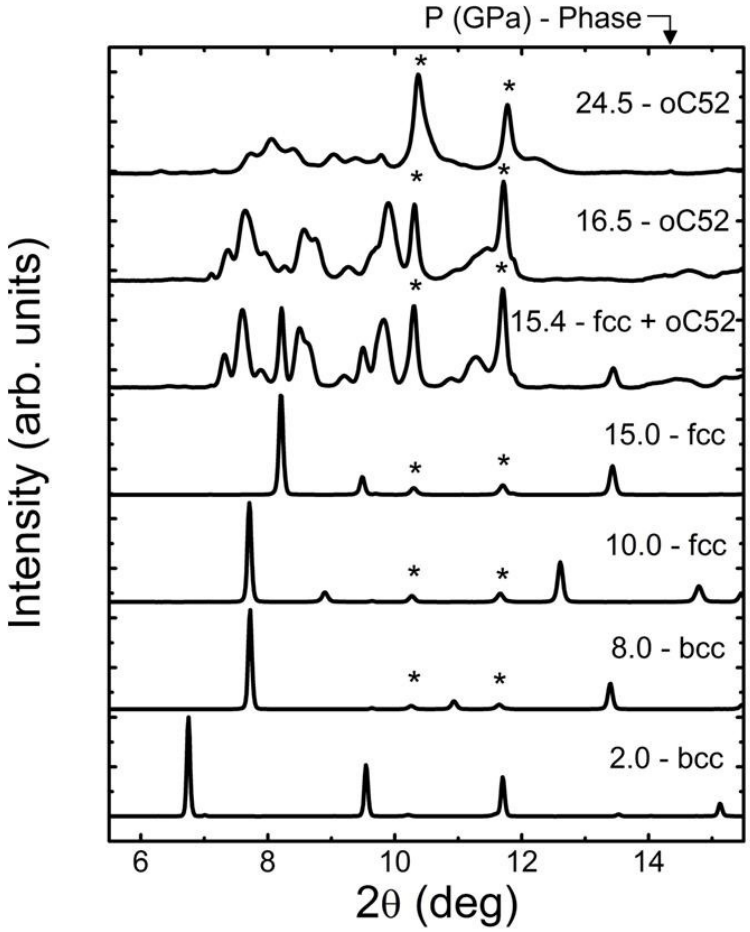

Figure 4.25: Rb diffractogram pressure dependence.

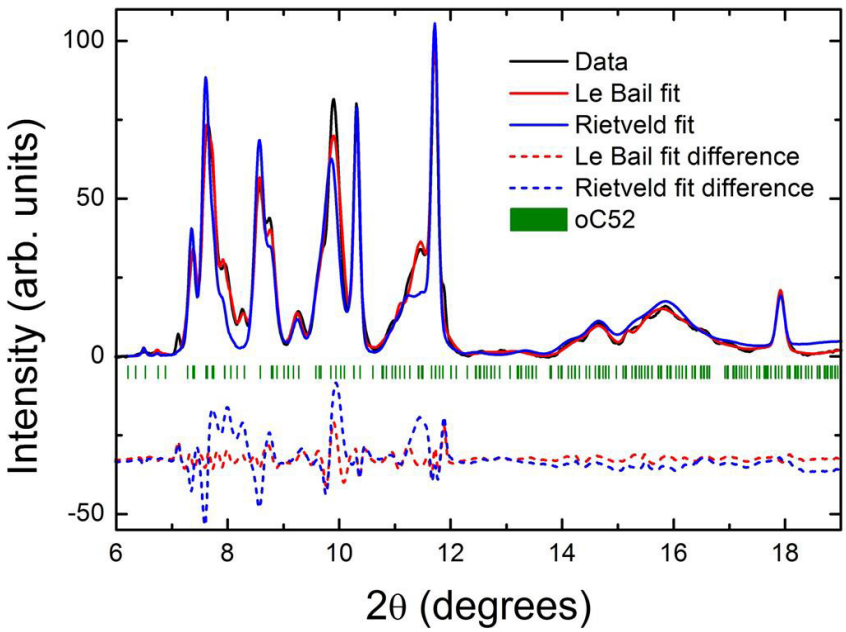

Figure 4.26: Rb difractogram at 17 GPa fit using Le Bail and Rietveld methods.

enormous number of reflections spanning most of the measured 2θ range (Fig. 4.26), making the indexing of peaks less reliable. Therefore, in order to verify the validity of this structure, Rietveld refinements were performed by fixing the fractional atomic positions to those found at room temperature [156]. Although this method is not expected to yield good fitting to the current data, a reasonable agreement between model and data is observed (Fig. 4.26). Differences in amplitudes remain, these are likely related to different fractional atomic positions in the unit cell and/or poor powder averaging.

4.3.1.3 - Cesium

The bcc to fcc transition in Cs occurs at 3.4±0.3 GPa at low temperature (Fig. 4.27). Further compression leads to fcc/Cs-IV (*tI*4) coexistence between 5.4±0.1 GPa and 6.1±0.3 GPa, after which the Cs-IV becomes stable to at least 13.4 GPa. No sign of the very low symmetry Cs-III (*oC*84) phase, stable only between 4.2 GPa and 4.3 GPa [153], are seen at low temperature. Even

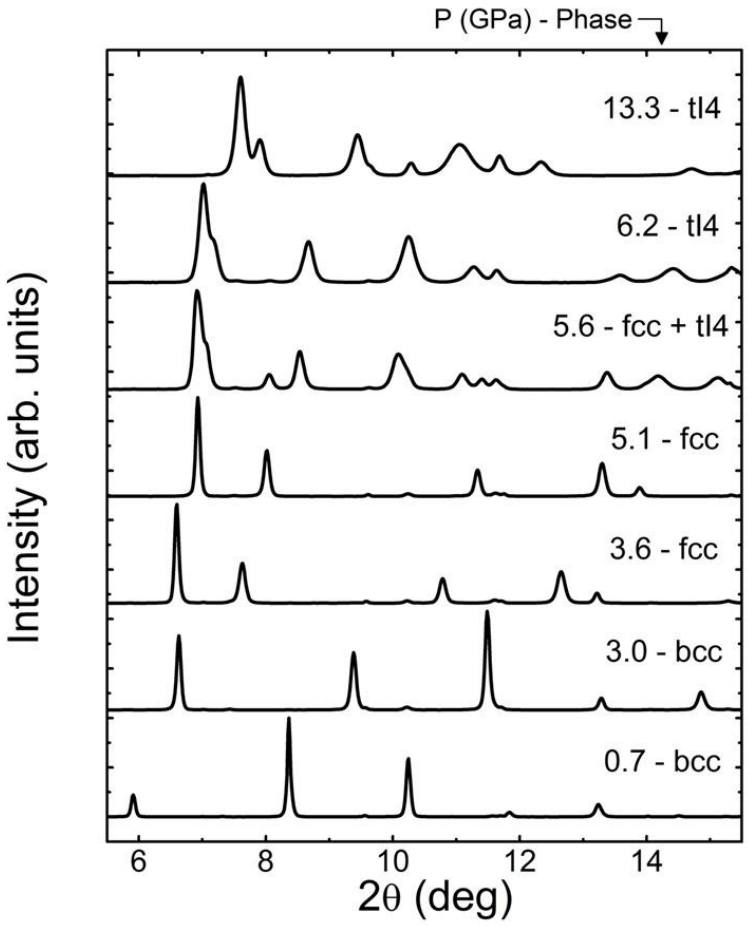

Figure 4.27: Cs diffractogram pressure dependence.

though the pressure step sized (0.3 GPa) used here prevents a definitive conclusion, the observed fcc-*tI*4 coexistence at 5.5 and 5.8 GPa is evidence that the Cs-III phase is not a possible ground state. This conclusion is also reached by DFT [148].

4.3.1.4 - Atomic Volumes

The pressure dependence of the atomic volume (unit cell volume divided by the number of atoms in it) of K, Rb, and Cs is displayed in Fig. 4.28, and agrees very well with the observed at ambient pressure [151,160,230]. The remarkable softness of the alkalis observed at room

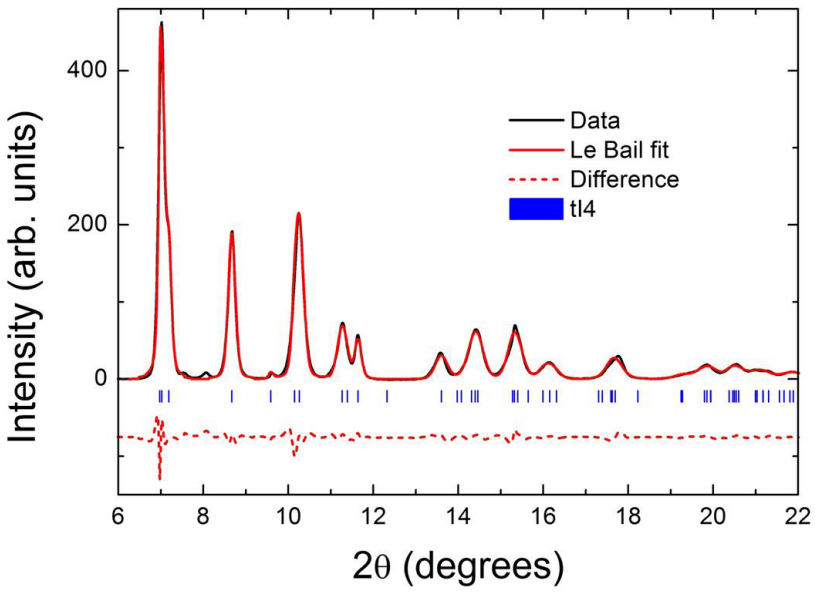

Figure 4.29: Cs 7 GPa diffractogram Le Bail fit.

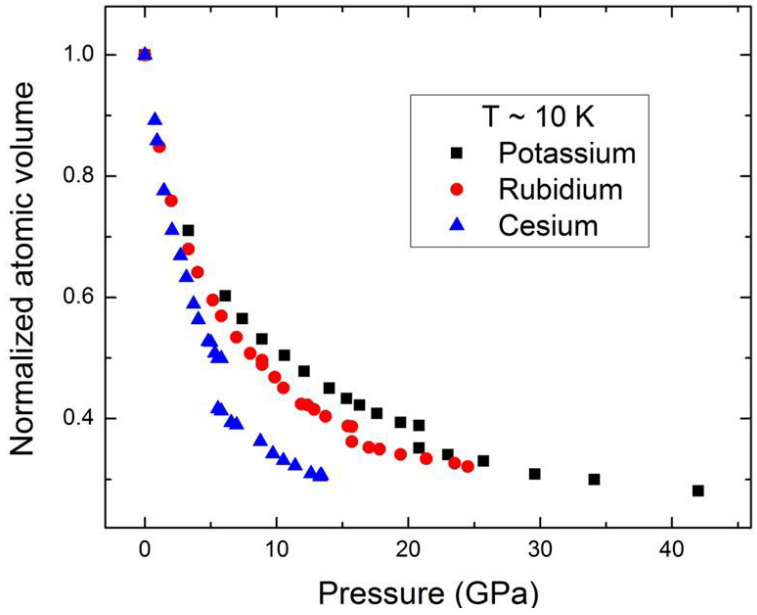

Figure 4.28: Volume pressure dependence of K, Rb, and Cs at 10 K.

temperature is reproduced at low T, Cs atomic volume for instance is reduced by a factor of 2 with the application of ~ 5 GPa. This behavior is understood as a combined effect of the weak metallic bonding and increasing *d* character of the conduction band with pressure. While no

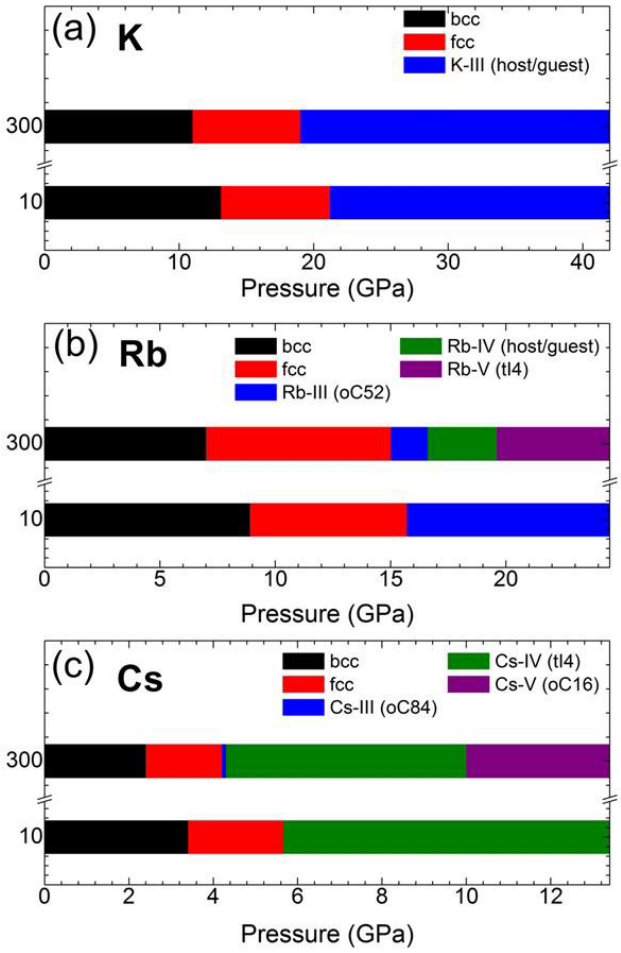

Figure 4.30: Phase transitions of K, Rb, and Cs at room temperature [22,160] and 10 K.

volume discontinuity is observed across the bcc to fcc transition, a sizeable volume collapse is seen at the emergence of the post-fcc phase.

4.3.2 Temperature Dependence of Structural Phases

While K displays the same phases at low and room temperatures to 42 GPa, albeit shifted towards higher transitions pressures, Rb and Cs display larger differences in their phase diagrams (Fig. 4.30). In the former, the Rb-III phase is stable to at least 24.5 GPa, ~ 9 GPa higher than seen at room temperature, overcoming the pressure range where Rb-IV and -V phases were expected to be stable [22]. In Cs, the low symmetry Cs-III phase is not observed. The Rb- and

Cs- III phases are complex layered structure, which display the same type of in plane order, but with different layer stacking [231]. The mismatching of these layers is believed to be unstable since the sliding of layers is prevented by a small energy barrier, which would explain their short range of stability (~ 0.1 GPa in Cs, and ~ 1.6 GPa in Rb at room temperature) [22]. The extended extended range for the Rb-III phase at low temperature supports this argument. Even though the absence of Cs-III seems to contradict this proposal, it is likely that Cs-III just becomes energetically unstable at low temperature, as suggested by DFT [148].

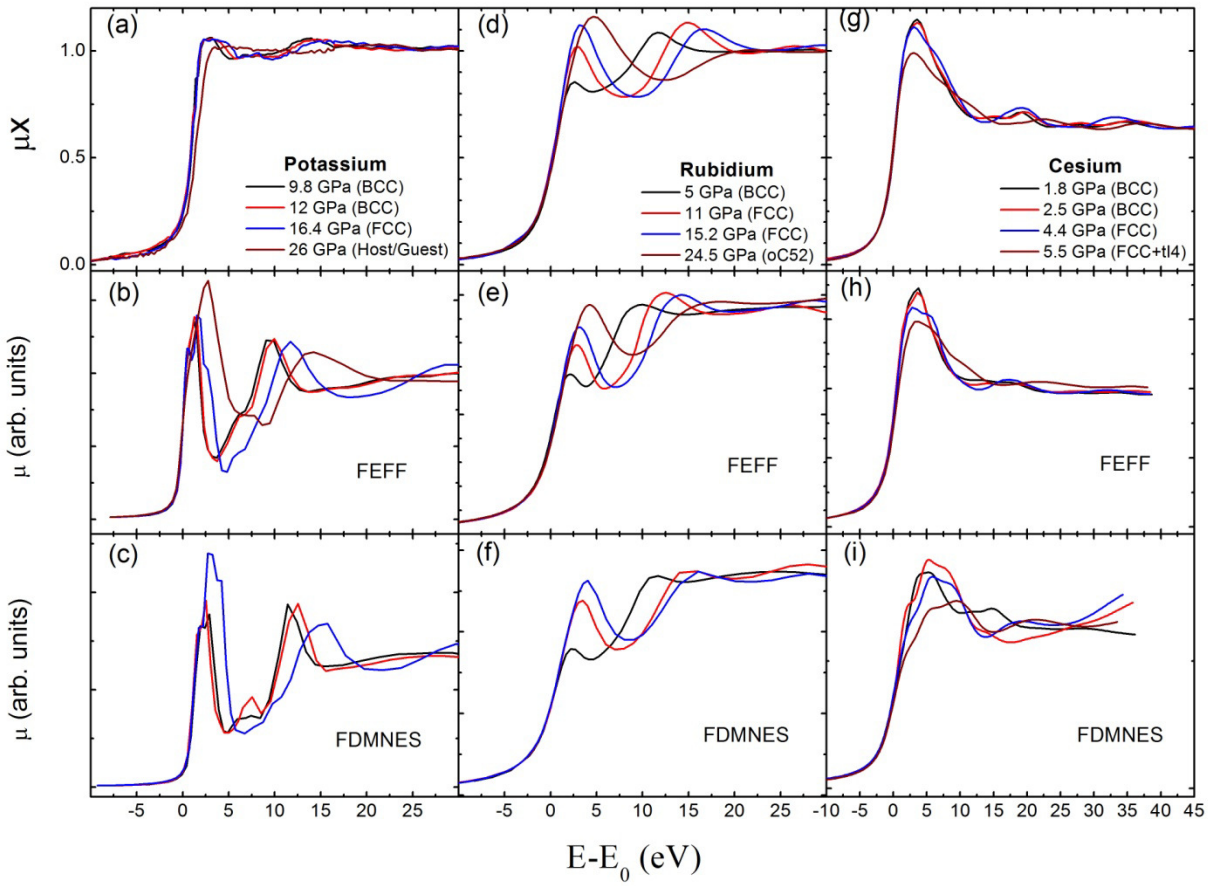

Figure 4.31: XANES pressure dependence of K, Rb K-edge and Cs L_3-edge together with the respective FEFF and FDMNES simulations.

4.3.3 XANES

The pressure dependence of XANES at the K-edges of K and Rb and L_3-edge of Cs is displayed in Fig. 4.31 together with its simulations using FEFF8 [197] and FDMNES [205]. The absorption cross section is dominated by the dipolar contribution, thus at the K-edge (1*s* core excitation) the photoelectron is mostly sensitive to the density of empty *p* states, and at the L_3-edge ($2p_{3/2}$ core excitation) to the empty *d* states. Strong pressure dependence is observed in Rb and Cs data. In the former, an increase in the lowest energy peak is observed, indicating an increase in the number of empty *p* states, while in the later the white line is suppressed, pointing to a reduction in the empty *d* states. These qualitative observations are consistent with an enhancement in *d* occupation at the expense of *sp* electrons.

Contrary to Rb and Cs, the K data are of much lower quality. For K's K-edge (3.608 keV) the two partially perforated anvils (200 μm of diamond) and the beamline's Be x-ray windows attenuate the beam by ~ 3000x. Although it yielded enough x-ray intensity to collect data, the spectrum was largely contaminated by the presence of high energy harmonics in the nominally monochromatic x-ray beam. Both undulator and monochromator used at 4-ID-D allow the x-ray third harmonic, i.e. Si(333) reflection at E = 3 x E[Si(111)] = 10.824 keV photons. At the higher third harmonic energy, the beamline/diamonds attenuates the beam by only ~1.4x. Attempts to reduce harmonic contamination were performed by using the reflection cutoff of a Si flat mirror and by detunning the double crystal monochromator, yet the data is still largely distorted. Given that the two approaches to calculate K's XANES agree, and that both approaches describe the Rb and Cs data very well, we argue that the lack of agreement between experiment and theory seen in Fig. 4.31 is due to harmonic contamination. Note that harmonics are expected to reduce the amplitude of the oscillations, as observed [195]. Furthermore, the EXAFS analysis used to

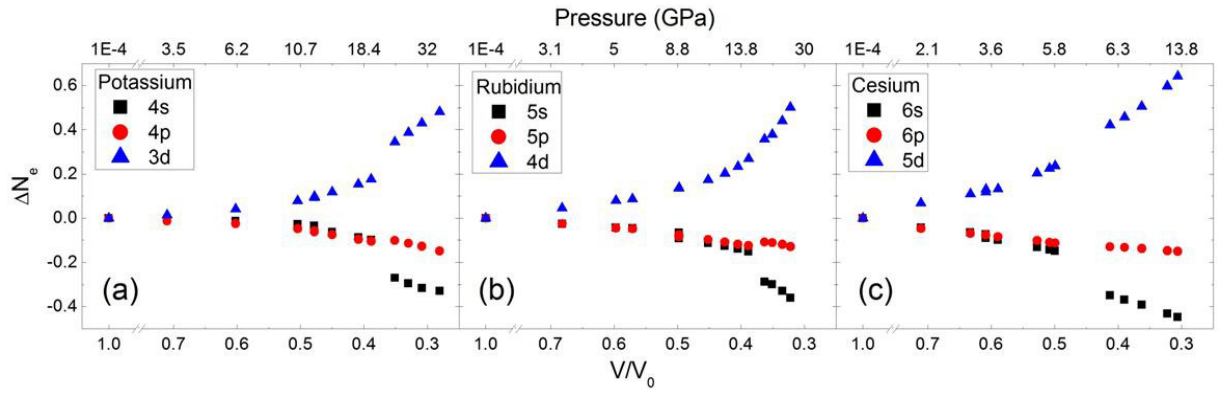

Figure 4.32: Orbital specific electron count for K, Rb, and Cs calculated with FEFF.

calibrate pressure in K's K-edge measurements also points to a strong suppression of the EXAFS oscillations amplitudes. Despite these issues, the pressure dependence of the XANES data for K appears to be consistent with the calculations, as pressure mostly broadens the first peak in the spectra.

4.3.4 Electronic Structure

The agreement between experiment and simulation (Fig. 4.31) provides validation of the calculated electronic structure. In the FEFF approach, the interatomic potential is approximated by overlapping muffin-tins. Although this imposes a severe limitation to the potential shape, the calculated partial density of states (*pDOS*) contains all valence electrons. On the other hand, FDMNES uses full potentials calculated using DFT. However, here the interstitial electrons are treated as plane waves, thus their angular momentum information is lost. Consequently, DFT yields only angular momentum specific local DOS (*lDOS*). Nevertheless, the total *DOS* calculated with both methods is similar, being further evidence that the calculated electronic structure is correct.

The increase in the *d* character of the conduction band occurs even for the lowest calculated pressures (Fig. 4.32). The very large volume reduction observed in the bcc phase (see Fig. 4.28) leads to only modest increases in *d* occupation (N_d). No significant discontinuity in orbital occupation is observed across the bcc-fcc transition. A faster increase in N_d is seen within the fcc phase at the expense of a similar decrease in both of *s* and *p* electron occupancy. The onset of the low symmetry phases is accompanied by a sudden reduction in the number of *s* electrons.

The *spd lDOS* obtained by DFT is displayed in Fig. 4.33. Clearly pressure does not shift the *spd* states, instead strong *spd* hybridization is observed as the *lDOS* for each orbital becomes

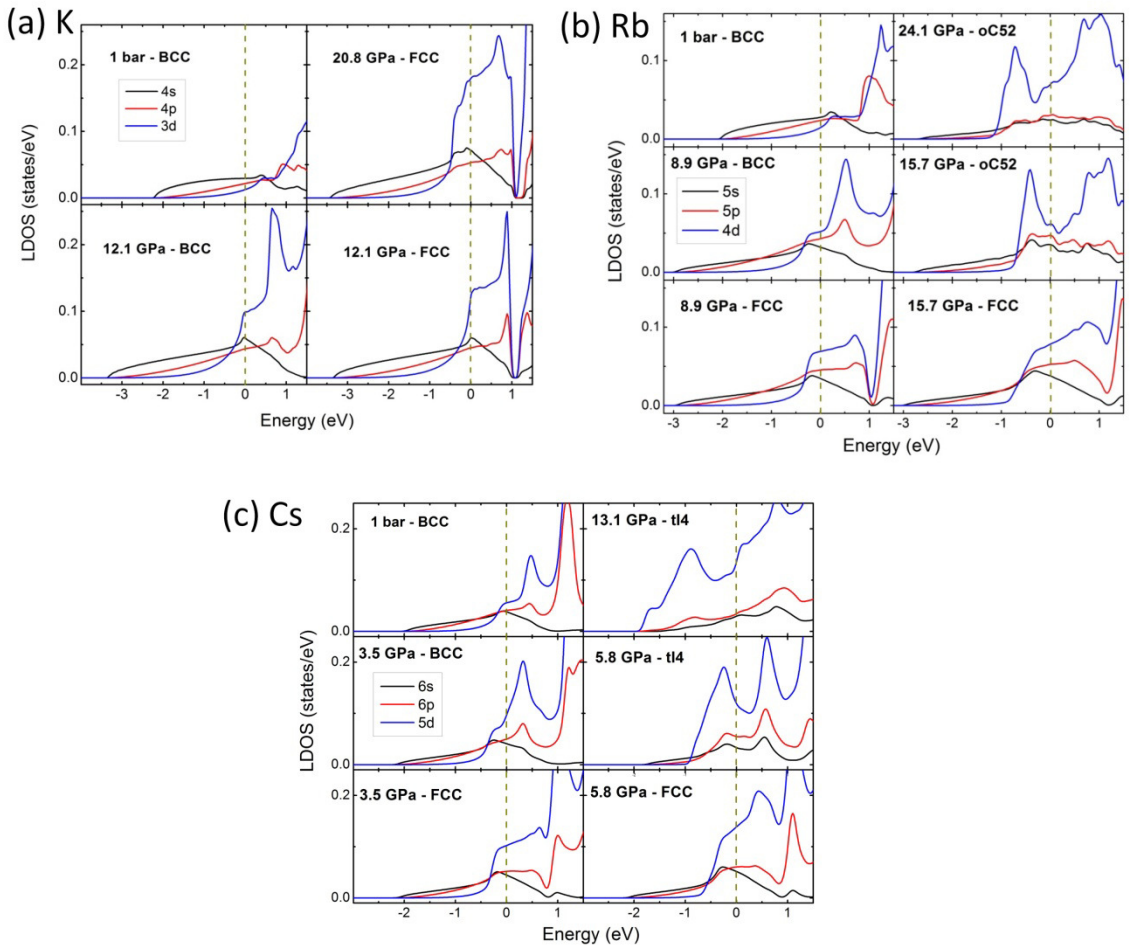

Figure 4.33: K (a), Rb (b), and Cs (c) lDOS pressure dependence calculated using DFT.

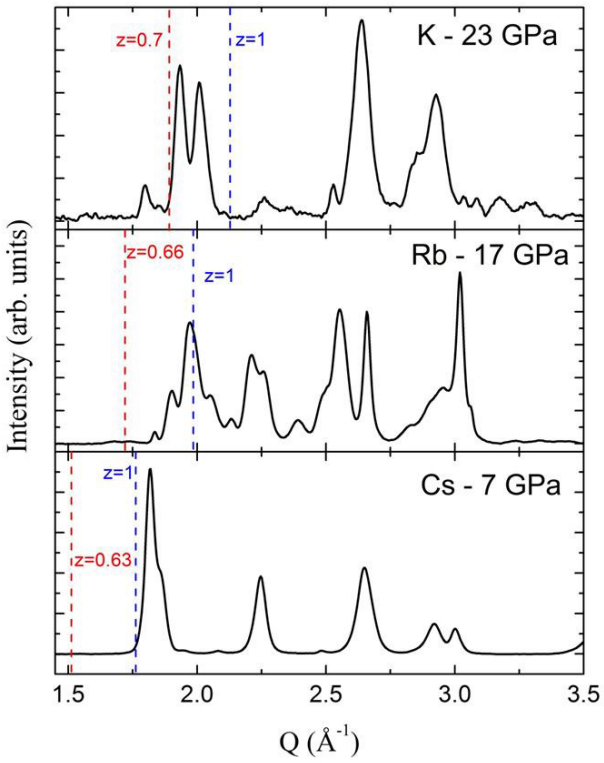

Figure 4.34: Diffractogram of the post-fcc phases of K, Rb, and Cs compared to the free electron Fermi wavevector for full *sp* occupation (blue), and for the occupation calculated by FEFF (red).

more and more alike. Across the fcc→post-fcc transition, a clear splitting of the DOS at the Fermi energy is observed, being consistent with an electronically driven symmetry reduction. Furthermore, the more localized character of the occupied valence states at the highest pressures indicate the accumulation of valence charges in the interstitial sites as discussed in section 4.3.6.

4.3.5 Correlation between Structural and Electronic Order

Perhaps the most prevalent explanation for the phase transitions observed in the alkalis is the FS-BZ mechanism [163,170–172]. A relevant feature of this mechanism is the emergence of strong Bragg peaks in close proximity to $2k_F$, where k_F is the free-electron Fermi surface radius, which opens a pseudo-gap at the Fermi level. Such pseudo-gap is consistent with the present

DFT calculations for Rb and Cs (Fig. 4.33). Therefore, experimental validation of this process can be addressed by evaluating the "closeness" factor $\eta = 2k_F/q$, where q is the reciprocal lattice vector of a Bragg reflection. If $1.0 < \eta < 1.05$, the FS-BZ mechanism is argued to be operational. The number of valence electrons used for the calculation of k_F is usually taken as the number of *sp* electrons (z) only, since *d* states tend to strongly deform the Fermi sphere [163]. Fig. 4.34 displays the diffractograms of K, Rb, and Cs within their post-fcc phases together with the position of the η calculated for a conduction band formed only by *sp* electrons (z = 1) and using the *sp* occupation calculated by FEFF (see Fig. 4.32). Only Rb in the z = 1 case is consistent with the FS-BZ mechanism. However, the remarkable similarity between the experimental and simulated XANES is strong evidence that $z \neq 1$. Furthermore, it has also been proposed that the Host/Guest structure of K is stabilized through a FS-BZ mechanism involving 2.6 valence electrons per atom due hybridization with the inner *p* state [172], which is in strong disagreement with the current data. Therefore, the ground state phase transitions of heavy alkalis cannot be explained within the FS-BZ mechanism.

The structural behavior across the actinide series is remarkably similar to the behavior of pressure in alkalis under pressure [169] (see section 2.3.2). It has been argued that the structures of metals could be explained by a competition of a Madelung contribution, which favors high symmetry phases, and Peierls distortion, favoring low symmetry [175]. While high symmetry is achieved in systems with delocalized conduction bands, low symmetry is favored when the localized character is enhanced. The three alkali metals studied here display conduction bandwidths of about 1.5 eV in the fcc phase (Fig. 4.33), in excellent agreement with the predicted ~1.2 eV maximum bandwidth necessary for the a Peierls distortion to occur in Fe [175]. Note that the comparison between Fe and the heavy alkalis at high pressure is

reasonable as, at the fcc→post-fcc boundary, the conduction band already has a significant *d* electron character (Fig. 4.34), bringing these alkalis closer to the properties of transition metals [232]. Finally, it is noticeable that the minima depth, hence the "degree of localization" of the conduction band, correlate with the complexity of the high-pressure structure of these alkalis, in agreement with the expectation from this theory.

The emergence of low symmetry phases can also be understood as a consequence of electronic localization [23–25] (see section 2.3.2). According to the FEFF calculations, the bcc→fcc transtition happens at N_s = 0.535±0.010 electrons, and the fcc→post-fcc at N_s = 0.46±0.01 electrons. Such remarkable similarity in *s* orbital occupation is evidence that the occupation of each orbital play a significant role in this transition.

4.3.6 Electronic Ordering and Superconductivity

The emergence of magnetic order in alkalis arising from the high-pressure electronic localization is an exciting possibility [148]. Although the observed crystal structures suggest lack of magnetic ordering in K at 10 K (Fig. 4.24), only magnetic measurements are able to definitely address this question. Attempts at using the x-ray magnetic circular dicroism (XMCD) technique in K, Rb, and Cs lead to inconclusive results. Even in the absence of magnetic ordering, the increase in electron localization should lead to a larger paramagnetic response (increased local moment) which might also be of interest. Nevertheless, if the magnetically ordered phases in K are ignored, DFT successfully predicts the fcc→post-fcc transition for K, Rb and Cs [148].

Among the alkalis, only Li and Cs are known to superconduct [138,139]. The T_c in Cs reaches only 1.4 K and is observed only in the ~11-15 GPa range, right at the boundary between the *tI*4 and *oC*16 phases [19]. Attempts to theoretically reproduce the observed superconductivity

using BCS theory have failed [140,233]. Furthermore, the theoretically predicted superconductivity in K and Rb has not been experimentally detected [140,141,145,234].

The relatively high-symmetry post-fcc phase observed in Cs allows an easier identification of the pressure induced electronic localization (Fig. 4.35). A "stripe-like" charge order is observed in the Cs-IV phase. These stripes are along the *b* and *c* directions, rotating 90° between consecutive planes and translating half of a unit cell between two consecutive planes with same orientation (Fig. 4.35). Little contact between the in-plane stripes occur due to the presence of close ionic cores, but a stronger interaction between stripes is observed between two planes at the

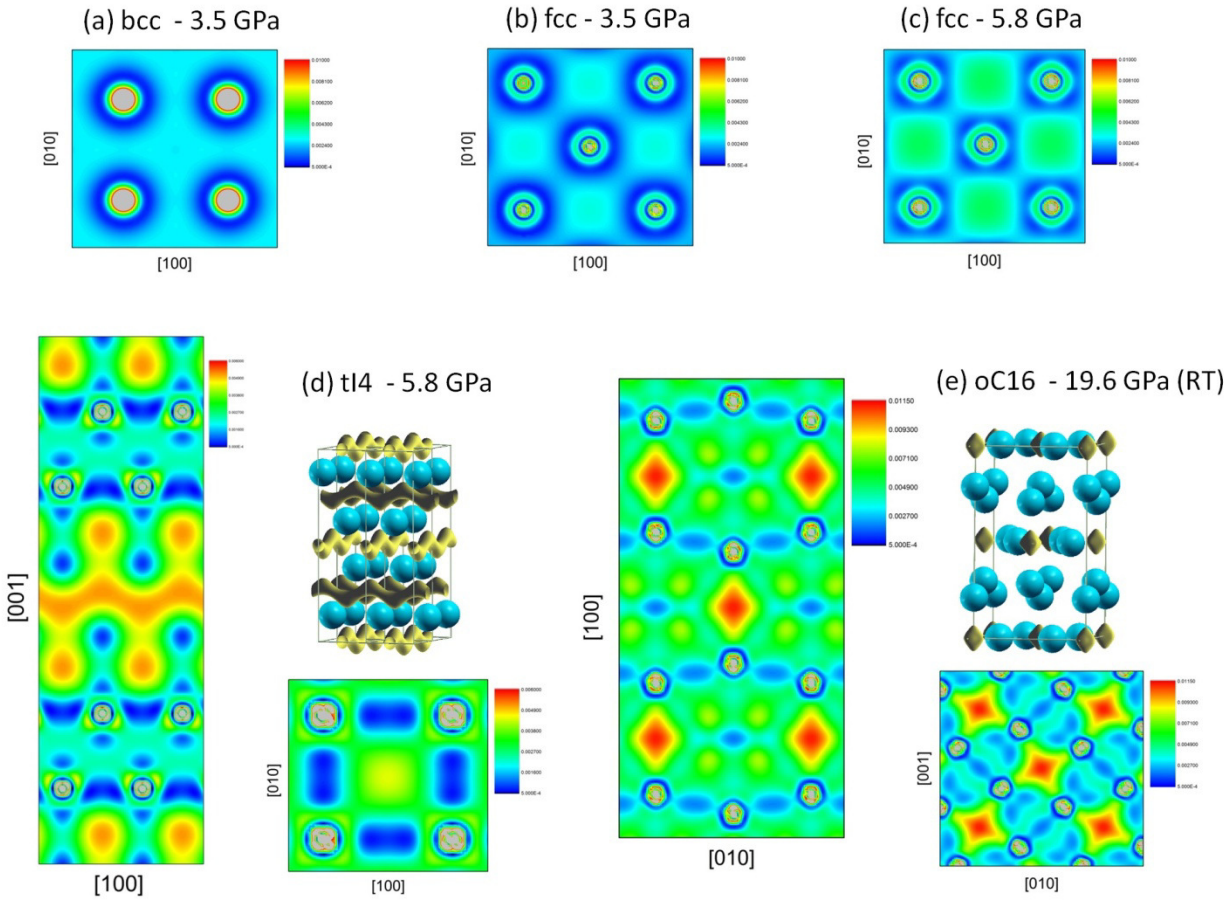

Figure 4.35: Valence electron spatial distribution in the observed phases of Cs.

crossing points (see Fig. 4.35). This charge order is remarkably similar to that observed in the $La_{1.875}Ba_{0.125}CuO_4$ studied in this thesis and described in section 2.1.1, including the same 90° rotation between planes and translation by half of unit cell between consecutive stripes with same orientation. The only difference is the periodicity within the plane, which is understood by the different number of valence (1) and doped (0.125) electrons. The Cs-V phase was not observed to 13.4 GPa at low temperature. This phase displays the localization of electrons into octahedral pockets [235], which has been reproduced in calculations here using the room temperature structure and lattice parameters for 19.6 GPa (Fig. 4.35) [149]. This structure displays Cs-only and Cs/electron pockets layers, these pockets substitute Cs atoms and attract the neighbors, distorting the Cs-only layer. This localization process is clearly observed by an increase in resistivity [19]. However, we note that a significant *DOS* at the Fermi level is observed in these phases; hence this localization process does not lead to insulating behavior.

4.3.7 Final Remarks

In this thesis, the electronic and structural ground state of heavy alkalis were investigated. Low symmetry phases are shown to emerge at 10 K at approximately same pressure as at room temperature (Fig. 4.30). Understanding the mechanism of such low symmetry phases in metals is of interest. At ambient pressure, low symmetry phases in metals are only observed in some actinides [169] and Hume-Rothery alloys [236], and are explained to be due a Peierls distortion in the former [175] and the Fermi surface – Brillouin zone interaction in the later [237]. The emergence of a pseudo-gap in the low symmetry phases, a property of both mechanisms, is observed. The FS-BZ mechanism is unable of describing the low symmetry phases for K and Cs, but it cannot be discarded for Rb. However, the current results points to a strong increase in *d* character in the conduction band that localizes states at the Fermi level, pointing to a Peierls

scenario. Furthermore, such deviation from a spherical Fermi surface is inconsistent with the FS-BZ mechanism.

The consequences of such electronic localization to the alkali properties are still largely unverified. The suggested emergence of magnetic ordering in K seems to disagree with the structural data. On the other hand, stripe-like charge ordering is theoretically suggested in Cs. Remarkably, superconductivity in Cs appears at the boundary between Cs-IV and -V phases [19], where the charge ordering is being suppressed, bearing strong resemblance to results on $LBCO_{1/8}$ where T_c increases as charge order is suppressed. There is mounting experimental evidence that charge order is an intrinsic property of high-T_c cuprates and iron pnictides [51,53,238,239]. However, the role of stripes in superconductivity is a matter of intense debate, with arguments ranging from these being competing ground states to being part of the same mechanism [1,34]. Consequently, the presence of superconductivity and stripes in close proximity in a monoatomic metal is quite exciting and demands further experimental and theoretical verification.

Chapter 5

Summary

The behavior of strongly correlated electrons is of general interest due to exotic and unexplained ground states observed in these systems. In this thesis high-pressure was used to tune different systems in/out of the strongly correlated state, while x-ray and transport techniques probed their properties.

In $La_{1.875}Ba_{0.125}CuO_4$ pressure suppresses the macroscopic CuO_6 tilt angle, leading to suppression of long range LTT order. Persistent charge order in the macroscopic HTT phase has been previously used to argue that charge order does not necessitate the CuO_6 tilt. This scenario has proved to be inaccurate as local LTT tilts persist even in the absence of long range LTT order, being intrinsically coupled to charge order domains. Furthermore, the pressure-enhanced superconducting T_c appears to only correlate with the local CuO_6 tilt angle, suggesting that very short ranged LTT tilts are sufficient to pin charge order.

The localized 4*f* state in Gd and Tb was investigated at extreme pressure to probe for deviations from its atomic-like character. While Gd's $4f^7$ configuration proved to be remarkably stable (up to at least 120 GPa), the $4f^8$ level of Tb becomes unstable above ~ 55 GPa. Such instability emerges through 4*f*-conduction band hybridization detected by the onset of Kondo interactions in measurements of the superconducting T_c of Y(RE) alloys. Therefore, Tb appears to become a dense Kondo lattice system at high pressure. Kondo lattices are of significant interest as they are host to many exotic phenomena, such as unconventional superconductivity [100,220]. Similar results have been obtained in Dy [229], and the

consequences of the suggested Kondo lattice state for magnetic ordering are under current investigation [128].

Finally, the structural and electronic ground state of K, Rb, and Cs was investigated at high-pressure. The present experimental evidence points to the emergence of remarkable low symmetry phases due to the suggested pressure-induced electronic localization. Furthermore, pressure strongly enhances the *d* character of the conduction band. Localized *d* states are prone to magnetic ordering as recently suggested [148], however our results imply that magnetic ordering is not achieved in these alkalis in the measured pressure range. Nevertheless, the electronic localization in Cs leads to a remarkable charge ordered state that strongly resembles that observed in $La_{1.875}Ba_{0.125}CuO_4$, including the presence of superconductivity in Cs coupled to the suppression of such charge ordered phase. Experimental validation of such a state and its relationship with superconductivity could provide important clues into the mechanism of high-T_c superconductivity in cuprates and pnictides.

Bibliography

[1] D. J. Scalapino, Rev. Mod. Phys. **84**, 1383 (2012).

[2] M. N. Baibich, J. M. Broto, A. Fert, F. N. Van Dau, and F. Petroff, Phys. Rev. Lett. **61**, 2472 (1988).

[3] G. Binasch, P. Grünberg, F. Saurenbach, and W. Zinn, Phys. Rev. B **39**, 4828 (1989).

[4] J. J. Sakurai, *Modern Quantum Mechanics* (Addison-Wesley Pub. Co., 2010).

[5] R. M. Martin, *Electronic Structure: Basic Theory and Practical Methods* (Cambridge University Press, Cambridge, 2004).

[6] Z. Yin and W. Pickett, Phys. Rev. B **74**, 205106 (2006).

[7] E. Wigner and F. Seitz, Phys. Rev. **43**, 804 (1933).

[8] E. Wigner and F. Seitz, Phys. Rev. **46**, 509 (1934).

[9] W. Kohn and L. J. Sham, Phys. Rev. **140**, A1133 (1965).

[10] E. Dagotto and Y. Tokura, MRS Bulletin **33**, 1037 (2011).

[11] V. N. Antonov, L. V. Bekenov, and a. N. Yaresko, Adv. Condens. Matter Phys. **2011**, 1 (2011).

[12] J. Tranquada, J. Axe, N. Ichikawa, Y. Nakamura, S. Uchida, and B. Nachumi, Phys. Rev. B. Condens. Matter **54**, 7489 (1996).

[13] M. Hücker, M. v. Zimmermann, G. D. Gu, Z. J. Xu, J. S. Wen, G. Xu, H. J. Kang, a. Zheludev, and J. M. Tranquada, Phys. Rev. B **83**, 104506 (2011).

[14] J. M. Tranquada, B. J. Sternlieb, J. D. Axe, Y. Nakamura, and S. Uchida, Nature **375**, 561 (1995).

[15] Q. Li, M. Hücker, G. Gu, A. Tsvelik, and J. Tranquada, Phys. Rev. Lett. **99**, 067001 (2007).

[16] E. Berg, E. Fradkin, E.-A. Kim, S. A. Kivelson, V. Oganesyan, J. M. Tranquada, and S. C. Zhang, Phys. Rev. Lett. **99**, 127003 (2007).

[17] G. Fabbris, M. Hücker, G. D. Gu, J. M. Tranquada, and D. Haskel, Phys. Rev. B **88**, 060507 (2013).

[18] G. Fabbris, T. Matsuoka, J. Lim, J. Mardegan, K. Shimizu, D. Haskel, and J. Schilling, Phys. Rev. B **88**, 245103 (2013).

[19] J. Wittig, in *Superconductivity in D- F- Band Metals*, edited by W. Buckel and W. Weber (Kernforschungszentrum, Karlsruhe, 1982), pp. 321–329.

[20] T. Matsuoka and K. Shimizu, Nature **458**, 186 (2009).

[21] Y. Ma, M. Eremets, A. R. Oganov, Y. Xie, I. Trojan, S. Medvedev, A. O. Lyakhov, M. Valle, and V. Prakapenka, Nature **458**, 182 (2009).

[22] M. I. McMahon and R. J. Nelmes, Chem. Soc. Rev. **35**, 943 (2006).

[23] J. B. Neaton and N. W. Ashcroft, Nature **400**, 141 (1999).

[24] J. Neaton and N. Ashcroft, Phys. Rev. Lett. **86**, 2830 (2001).

[25] B. Rousseau and N. Ashcroft, Phys. Rev. Lett. **101**, 046407 (2008).

[26] H. K. Onnes, Commun. Phys. Lab. Univ. Leiden **120b**, (1911).

[27] H. K. Onnes, Commun. Phys. Lab. Univ. Leiden **122b**, (1911).

[28] D. van Delft and P. Kes, Phys. Today **63**, 38 (2010).

[29] S. A. Kivelson, I. P. Bindloss, V. Oganesyan, J. M. Tranquada, A. Kapitulnik, and C. Howald, Rev. Mod. Phys. **75**, 1201 (2003).

[30] P. a. Lee and X.-G. Wen, Rev. Mod. Phys. **78**, 17 (2006).

[31] K. H. Bennemann and J. B. Ketterson, editors, *Superconductivity* (Springer Berlin Heidelberg, Berlin, Heidelberg, 2008).

[32] J. M. Tranquada, Science **337**, 811 (2012).

[33] E. Fradkin and S. A. Kivelson, Nat. Phys. **8**, 864 (2012).

[34] B. Keimer, S. A. Kivelson, M. R. Norman, S. Uchida, and J. Zaanen, arXiv:1409.4673 [cond-mat.supr-con] (2014).

[35] L. Cooper, Phys. Rev. **104**, 1189 (1956).

[36] J. Bardeen, L. Cooper, and J. Schrieffer, Phys. Rev. **106**, 162 (1957).

[37] J. Bardeen, L. N. Cooper, and J. R. Schrieffer, Phys. Rev. **108**, 1175 (1957).

[38] L. N. Cooper and D. Feldman, *BCS: 50 Years* (World Scientific, Singapore, 2010).

[39] F. Steglich, J. Aarts, C. Bredl, W. Lieke, D. Meschede, W. Franz, and H. Schäfer, Phys. Rev. Lett. **43**, 1892 (1979).

[40] C. Pfleiderer, Rev. Mod. Phys. **81**, 1551 (2009).

[41] Q. Si and F. Steglich, Science **329**, 1161 (2010).

[42] J. G. Bednorz and K. A. Müller, Zeitschrift Für Phys. B Condens. Matter **64**, 189 (1986).

[43] R. M. Hazen, *The Breakthrough: The Race for the Superconductor* (Summit Books/Simon & Schuster, 1988).

[44] M. Wu, J. Ashburn, C. Torng, P. Hor, R. Meng, L. Gao, Z. Huang, Y. Wang, and C. Chu, Phys. Rev. Lett. **58**, 908 (1987).

[45] C. W. Chu, L. Gao, F. Chen, Z. J. Huang, R. L. Meng, and Y. Y. Xue, Nature **365**, 323 (1993).

[46] J. Paglione and R. L. Greene, Nat. Phys. **6**, 645 (2010).

[47] C. L. Smallwood, J. P. Hinton, C. Jozwiak, W. Zhang, J. D. Koralek, H. Eisaki, D.-H. Lee, J. Orenstein, and A. Lanzara, Science **336**, 1137 (2012).

[48] M. Hücker, Phys. C: Supercond. **481**, 3 (2012).

[49] G. Ghiringhelli, M. Le Tacon, M. Minola, S. Blanco-Canosa, C. Mazzoli, N. B. Brookes, G. M. De Luca, a Frano, D. G. Hawthorn, F. He, T. Loew, M. Moretti Sala, D. C. Peets, M. Salluzzo, E. Schierle, R. Sutarto, G. a Sawatzky, E. Weschke, B. Keimer, and L. Braicovich, Science **337**, 821 (2012).

[50] S. Dal Conte, C. Giannetti, G. Coslovich, F. Cilento, D. Bossini, T. Abebaw, F. Banfi, G. Ferrini, H. Eisaki, M. Greven, A. Damascelli, D. van der Marel, and F. Parmigiani, Science **335**, 1600 (2012).

[51] R. Comin, A. Frano, M. M. Yee, Y. Yoshida, H. Eisaki, E. Schierle, E. Weschke, R. Sutarto, F. He, A. Soumyanarayanan, Y. He, M. Le Tacon, I. S. Elfimov, J. E. Hoffman, G. A. Sawatzky, B. Keimer, and a Damascelli, Science **343**, 390 (2013).

[52] S. E. Sebastian, N. Harrison, F. F. Balakirev, M. M. Altarawneh, P. A. Goddard, R. Liang, D. A. Bonn, W. N. Hardy, and G. G. Lonzarich, Nature **511**, 61 (2014).

[53] E. H. da Silva Neto, P. Aynajian, A. Frano, R. Comin, E. Schierle, E. Weschke, A. Gyenis, J. Wen, J. Schneeloch, Z. Xu, S. Ono, G. Gu, M. Le Tacon, and A. Yazdani, Science **343**, 393 (2014).

[54] R. Comin, A. Frano, M. M. Yee, Y. Yoshida, H. Eisaki, E. Schierle, E. Weschke, R. Sutarto, F. He, A. Soumyanarayanan, Y. He, M. Le Tacon, I. S. Elfimov, J. E. Hoffman, G. Sawatzky, B. Keimer, and A. Damascelli, Science **343**, 390 (2014).

[55] N. P. Armitage, Nat. Mater. **13**, 665 (2014).

[56] S. Kivelson, E. Fradkin, and V. Emery, Nature **393**, (1998).

[57] E. Berg, E. Fradkin, and S. Kivelson, Phys. Rev. B **79**, (2009).

[58] J. Chang, E. Blackburn, A. T. Holmes, N. B. Christensen, J. Larsen, J. Mesot, R. Liang, D. A. Bonn, W. N. Hardy, A. Watenphul, M. v. Zimmermann, E. M. Forgan, and S. M. Hayden, Nat. Phys. **8**, 871 (2012).

[59] A. J. Achkar, R. Sutarto, X. Mao, F. He, A. Frano, S. Blanco-Canosa, M. Le Tacon, G. Ghiringhelli, L. Braicovich, M. Minola, M. Moretti Sala, C. Mazzoli, R. Liang, D. A. Bonn, W. N. Hardy, B. Keimer, G. A. Sawatzky, and D. G. Hawthorn, Phys. Rev. Lett. **109**, 167001 (2012).

[60] E. Fradkin, S. A. Kivelson, and J. M. Tranquada, arXiv:1407.4480v1 [cond-mat.supr-con] (2014).

[61] N. Yamada and M. Ido, Phys. C: Supercond. **203**, 240 (1992).

[62] A. R. Moodenbaugh, Y. Xu, M. Suenaga, T. Folkerts, and R. Shelton, Phys. Rev. B **38**, 4596 (1988).

[63] S. Billinge, G. Kwei, and H. Takagi, Phys. Rev. Lett. **72**, 2282 (1994).

[64] D. Haskel, E. Stern, D. Hinks, A. Mitchell, J. Jorgensen, and J. Budnick, Phys. Rev. Lett. **76**, 439 (1996).

[65] D. Haskel, E. Stern, F. Dogan, and A. Moodenbaugh, Phys. Rev. B **61**, 7055 (2000).

[66] W. E. Pickett, R. E. Cohen, and H. Krakauer, Phys. Rev. Lett. **67**, 228 (1991).

[67] T. Adachi, T. Noji, and Y. Koike, Phys. Rev. B **64**, 144524 (2001).

[68] M. Crawford, R. Harlow, E. McCarron, W. Farneth, J. Axe, H. Chou, and Q. Huang, Phys. Rev. B **44**, 7749 (1991).

[69] M. Norman, G. McMullan, D. Novikov, and A. Freeman, Phys. Rev. B **48**, 9935 (1993).

[70] M. Hücker, M. v. Zimmermann, M. Debessai, J. S. Schilling, J. M. Tranquada, and G. D. Gu, Phys. Rev. Lett. **104**, 057004 (2010).

[71] J. Jensen and A. R. Mackintosh, *Rare Earth Magnetism: Structures and Excitations* (Oxford Univeristy Press, 1991).

[72] M. B. Maple, J. Phys. Soc. Japan **74**, 222 (2005).

[73] B. Dunlap, Phys. Rev. B **34**, 1496 (1986).

[74] A. Amici, P. Thalmeier, and P. Fulde, Phys. Rev. Lett. **84**, 1800 (2000).

[75] J. Houmann, B. Rainford, J. Jensen, and A. Mackintosh, Phys. Rev. B **20**, 1105 (1979).

[76] H. Møller, J. Jensen, M. Wulff, A. Mackintosh, O. McMasters, and K. Gschneidner, Phys. Rev. Lett. **49**, 482 (1982).

[77] A. Freeman and R. Watson, Phys. Rev. **127**, 2058 (1962).

[78] A. D. McLean and R. S. McLean, At. Data Nucl. Data Tables **26**, 197 (1981).

[79] J. Duthie and D. Pettifor, Phys. Rev. Lett. **38**, 564 (1977).

[80] W. Grosshans and W. Holzapfel, Phys. Rev. B **45**, 5171 (1992).

[81] M. A. Ruderman and C. Kittel, Phys. Rev. **96**, 99 (1954).

[82] T. Kasuya, Prog. Theor. Phys. **16**, 45 (1956).

[83] K. Yosida, Phys. Rev. **106**, 893 (1957).

[84] J. Kondo, Prog. Theor. Phys. **28**, 846 (1962).

[85] J. Kondo, Prog. Theor. Phys. **32**, 37 (1964).

[86] N. Andrei, K. Furuya, and J. Lowenstein, Rev. Mod. Phys. **55**, 331 (1983).

[87] H. Prüser, M. Wenderoth, P. E. Dargel, A. Weismann, R. Peters, T. Pruschke, and R. G. Ulbrich, Nat. Phys. **7**, 203 (2011).

[88] S. Doniach, Phys. B+C **91**, 231 (1977).

[89] J. H. Shim, K. Haule, and G. Kotliar, Nature **446**, 513 (2007).

[90] Y. Yang, Z. Fisk, H.-O. Lee, J. D. Thompson, and D. Pines, Nature **454**, 611 (2008).

[91] S. Ernst, S. Kirchner, C. Krellner, C. Geibel, G. Zwicknagl, F. Steglich, and S. Wirth, Nature **474**, 362 (2011).

[92] A. A. Abrikosov, Physics **2**, 5 (1965).

[93] A. A. Abrikosov, Sov. Phys. Uspekhi **12**, 168 (1969).

[94] K. Fischer, Zeitschrift Für Phys. **225**, 444 (1969).

[95] C. V Parker, P. Aynajian, E. H. da Silva Neto, A. Pushp, S. Ono, J. Wen, Z. Xu, G. Gu, and A. Yazdani, Nature **468**, 677 (2010).

[96] L. Chotorlishvili, A. Ernst, V. K. Dugaev, a. Komnik, M. G. Vergniory, E. V. Chulkov, and J. Berakdar, Phys. Rev. B **89**, 075103 (2014).

[97] H. Beidenkopf, P. Roushan, J. Seo, L. Gorman, I. Drozdov, Y. S. Hor, R. J. Cava, and A. Yazdani, Nat. Phys. **7**, 939 (2011).

[98] P. Aynajian, E. H. da Silva Neto, A. Gyenis, R. E. Baumbach, J. D. Thompson, Z. Fisk, E. D. Bauer, and A. Yazdani, Nature **486**, 201 (2012).

[99] M. Z. Asadzadeh, M. Fabrizio, and F. Becca, arXiv:1403.2631 [cond-mat.str-el] (2014).

[100] O. Bodensiek, R. Žitko, M. Vojta, M. Jarrell, and T. Pruschke, Phys. Rev. Lett. **110**, 146406 (2013).

[101] B. Matthias, H. Suhl, and E. Corenzwit, Phys. Rev. Lett. **1**, 92 (1958).

[102] A. A. Abrikosov and L. P. Gor'kov, Sov. Phys. JETP **12**, 1243 (1961).

[103] M. B. Maple, Appl. Catal. B Environ. **9**, 179 (1976).

[104] M. B. Maple, Phys. Lett. A **26**, 513 (1968).

[105] M. Maple, Phys. Lett. A **42**, 247 (1972).

[106] J. Zittartz and E. Müller-Hartmann, Zeitschrift Für Phys. **232**, 11 (1970).

[107] E. Müller-Hartmann and J. Zittartz, Zeitschrift Für Phys. **234**, 58 (1970).

[108] E. Müller-Hartmann and J. Zittartz, Phys. Rev. Lett. **26**, 428 (1971).

[109] M. B. Maple, W. A. Fertig, A. C. Mota, L. E. DeLong, D. Wohlleben, and R. Fitzgerald, Solid State Commun. **11**, 829 (1972).

[110] P. Bridgman, Proc. Am. Acad. Arts Sci. **76**, 55 (1948).

[111] A. Lawson and T.-Y. Tang, Phys. Rev. **76**, 301 (1949).

[112] M. Lipp, D. Jackson, H. Cynn, C. Aracne, W. Evans, and A. McMahan, Phys. Rev. Lett. **101**, 165703 (2008).

[113] M. MacPherson and G. Everett, Phys. Rev. Lett. **26**, 20 (1971).

[114] R. Ramirez and L. M. Falicov, Phys. Rev. B **3**, 2425 (1971).

[115] B. Johansson, Philos. Mag. **30**, 469 (1974).

[116] J. W. Allen and R. M. Martin, Phys. Rev. Lett. **49**, 1106 (1982).

[117] J. Schilling, Adv. Phys. **28**, 657 (1979).

[118] M. Krisch, D. L. Farber, R. Xu, D. Antonangeli, C. M. Aracne, A. Beraud, T.-C. Chiang, J. Zarestky, D. Y. Kim, E. I. Isaev, R. Ahuja, and B. Johansson, Proc. Natl. Acad. Sci. U. S. A. **108**, 9342 (2011).

[119] U. Kornstädt, R. Lässer, and B. Lengeler, Phys. Rev. B **21**, 1898 (1980).

[120] M. Lipp, A. P. Sorini, J. Bradley, B. Maddox, K. Moore, H. Cynn, T. Devereaux, Y. Xiao, P. Chow, and W. Evans, Phys. Rev. Lett. **109**, 195705 (2012).

[121] N. Lanatà, Y.-X. Yao, C.-Z. Wang, K.-M. Ho, J. Schmalian, K. Haule, and G. Kotliar, Phys. Rev. Lett. **111**, 196801 (2013).

[122] H. Hua, Y. Vohra, J. Akella, S. Weir, R. Ahuja, and B. Johansson, Rev. High Press. Sci. Technol. **7**, 233 (1998).

[123] N. Cunningham, W. Qiu, K. Hope, H.-P. Liermann, and Y. Vohra, Phys. Rev. B **76**, 212101 (2007).

[124] C.-S. Yoo, B. Maddox, and V. Iota, Mater. Res. Soc. Symp. Proc. **1104**, NN01 (2011).

[125] B. Maddox, A. Lazicki, C. Yoo, V. Iota, M. Chen, A. McMahan, M. Hu, P. Chow, R. Scalettar, and W. Pickett, Phys. Rev. Lett. **96**, 215701 (2006).

[126] Y. Akahama, H. Fujihisa, and H. Kawamura, Phys. Rev. Lett. **94**, 195503 (2005).

[127] G. K. Samudrala, G. M. Tsoi, and Y. K. Vohra, J. Phys. Condens. Matter **24**, 362201 (2012).

[128] J. Lim, G. Fabbris, D. Haskel, and J. S. Schilling, *in preparation* (2014).

[129] N. W. Ashcroft and N. D. Mermin, *Solid State Physics* (Saunders College, 1976).

[130] I. Loa, K. Syassen, G. Monaco, G. Vankó, M. Krisch, and M. Hanfland, Phys. Rev. Lett. **107**, 086402 (2011).

[131] T. Matsuoka, M. Sakata, Y. Nakamoto, K. Takahama, K. Ichimaru, K. Mukai, K. Ohta, N. Hirao, Y. Ohishi, and K. Shimizu, Phys. Rev. B **89**, 144103 (2014).

[132] R. Stager and H. Drickamer, Phys. Rev. Lett. **12**, 19 (1964).

[133] A. Jayaraman, R. Newton, and J. McDonough, Phys. Rev. **159**, 527 (1967).

[134] D. B. McWhan and A. L. Stevens, Solid State Commun. **7**, 301 (1969).

[135] J. Wittig, Phys. Rev. Lett. **24**, 812 (1970).

[136] J. Wittig, Mat. Res. Soc. Symp. Proc. **22**, 17 (1984).

[137] M. Abd-Elmeguid, H. Pattyn, and S. Bukshpan, Phys. Rev. Lett. **72**, 502 (1994).

[138] K. Shimizu, H. Ishikawa, D. Takao, T. Yagi, and K. Amaya, Nature **419**, 597 (2002).

[139] S. Deemyad and J. Schilling, Phys. Rev. Lett. **91**, 14 (2003).

[140] L. Shi and D. Papaconstantopoulos, Phys. Rev. B **73**, 184516 (2006).

[141] G. Profeta, C. Franchini, N. Lathiotakis, A. Floris, A. Sanna, M. Marques, M. Lüders, S. Massidda, E. Gross, and A. Continenza, Phys. Rev. Lett. **96**, 047003 (2006).

[142] D. Kasinathan, J. Kuneš, A. Lazicki, H. Rosner, C. Yoo, R. Scalettar, and W. Pickett, Phys. Rev. Lett. **96**, 047004 (2006).

[143] R. Akashi and R. Arita, Phys. Rev. Lett. **111**, 057006 (2013).

[144] A. M. J. Schaeffer, S. R. Temple, J. K. Bishop, and S. Deemyad, arXiv:1406.4565 [cond-mat.supr-con] (2014).

[145] A. Sanna, C. Franchini, A. Floris, G. Profeta, N. Lathiotakis, M. Lüders, M. Marques, E. Gross, A. Continenza, and S. Massidda, Phys. Rev. B **73**, 144512 (2006).

[146] T. Tomita, S. Deemyad, J. J. Hamlin, J. S. Schilling, V. G. Tissen, B. W. Veal, L. Chen, and H. Claus, J. Phys. Condens. Matter **17**, S921 (2005).

[147] N. Hillier, High Pressure Studies of Superconductivity, Washington University in Saint Louis, 2013.

[148] C. J. Pickard and R. J. Needs, Phys. Rev. Lett. **107**, 087201 (2011).

[149] U. Schwarz, K. Takemura, M. Hanfland, and K. Syassen, Phys. Rev. Lett. 2711 (1998).

[150] U. Schwarz, a. Grzechnik, K. Syassen, I. Loa, and M. Hanfland, Phys. Rev. Lett. **83**, 4085 (1999).

[151] U. Schwarz and K. Syassen, Solid State Commun. **112**, 319 (1999).

[152] M. McMahon, S. Rekhi, and R. Nelmes, Phys. Rev. Lett. **87**, 055501 (2001).

[153] M. McMahon, R. Nelmes, and S. Rekhi, Phys. Rev. Lett. **87**, 255502 (2001).

[154] R. Nelmes, M. McMahon, J. Loveday, and S. Rekhi, Phys. Rev. Lett. **88**, 155503 (2002).

[155] M. Hanfland, I. Loa, and K. Syassen, Phys. Rev. B **65**, 184109 (2002).

[156] M. McMahon, R. Nelmes, U. Schwarz, and K. Syassen, Phys. Rev. B **74**, 140102 (2006).

[157] M. I. McMahon, E. Gregoryanz, L. F. Lundegaard, I. Loa, C. Guillaume, R. J. Nelmes, a K. Kleppe, M. Amboage, H. Wilhelm, and a P. Jephcoat, Proc. Natl. Acad. Sci. U. S. A. **104**, 17297 (2007).

[158] L. Lundegaard, M. Marqués, G. Stinton, G. Ackland, R. Nelmes, and M. McMahon, Phys. Rev. B **80**, 020101 (2009).

[159] C. L. Guillaume, E. Gregoryanz, O. Degtyareva, M. I. McMahon, M. Hanfland, S. Evans, M. Guthrie, S. V. Sinogeikin, and H.-K. Mao, Nat. Phys. **7**, 211 (2011).

[160] L. F. Lundegaard, G. W. Stinton, M. Zelazny, C. L. Guillaume, J. E. Proctor, I. Loa, E. Gregoryanz, R. J. Nelmes, and M. I. McMahon, Phys. Rev. B **88**, 054106 (2013).

[161] A. M. J. Schaeffer, W. B. Talmadge, S. R. Temple, and S. Deemyad, Phys. Rev. Lett. **109**, 185702 (2012).

[162] J. Xie, S. Chen, J. Tse, D. Klug, Z. Li, K. Uehara, and L. Wang, Phys. Rev. B **62**, 3624 (2000).

[163] G. J. Ackland and I. R. Macleod, New J. Phys. **6**, 138 (2004).

[164] A. Rodriguez-Prieto, A. Bergara, V. Silkin, and P. Echenique, Phys. Rev. B **74**, 172104 (2006).

[165] Y. Xie, J. Tse, T. Cui, A. Oganov, Z. He, Y. Ma, and G. Zou, Phys. Rev. B **75**, 064102 (2007).

[166] Y. Xie, Y. M. Ma, T. Cui, Y. Li, J. Qiu, and G. T. Zou, New J. Phys. **10**, 063022 (2008).

[167] V. F. Degtyareva and O. Degtyareva, New J. Phys. **11**, 063037 (2009).

[168] A. McMahan, Phys. Rev. B **29**, 5982 (1984).

[169] K. Moore and G. van der Laan, Rev. Mod. Phys. **81**, 235 (2009).

[170] V. F. Degtyareva, High Press. Res. **23**, 253 (2003).

[171] V. Degtyareva, Physics-Uspekhi **49**, 369 (2006).

[172] V. F. Degtyareva, Solid State Sci. **36**, 62 (2014).

[173] E. Gregoryanz, O. Degtyareva, M. Somayazulu, R. Hemley, and H. Mao, Phys. Rev. Lett. **94**, 185502 (2005).

[174] R. Boehler and C.-S. Zha, Phys. B+C **139-140**, 233 (1986).

[175] P. Söderlind, O. Eriksson, B. Johansson, J. M. Wills, and A. M. Boring, Nature **374**, 524 (1995).

[176] A. Jayaraman, Rev. Mod. Phys. **55**, 65 (1983).

[177] M. Eremets, *High Pressure Experimental Methods* (Oxford Univeristy Press, New York, 1996.

[178] M. Rivers, V. Prakapenka, A. Kubo, C. Pullins, C. Holl, and S. Jacobsen, High Press. Res. **28**, 273 (2008).

[179] A. Dadashev, M. P. Pasternak, G. K. Rozenberg, and R. D. Taylor, Rev. Sci. Instrum. **72**, 2633 (2001).

[180] R. Boehler and K. De Hantsetters, High Press. Res. **24**, 391 (2004).

[181] K. Syassen, High Press. Res. **28**, 75 (2008).

[182] A. D. Chijioke, W. J. Nellis, a. Soldatov, and I. F. Silvera, J. Appl. Phys. **98**, 114905 (2005).

[183] M. Hanfland and K. Syassen, J. Appl. Phys. **57**, 2752 (1985).

[184] L. A. Lyon, C. D. Keating, A. P. Fox, B. E. Baker, L. He, S. R. Nicewarner, S. P. Mulvaney, and M. J. Natan, Anal. Chem. **70**, 341 (1998).

[185] W. B. Holzapfel, M. Hartwig, and W. Sievers, J. Phys. Chem. Ref. Data **30**, 515 (2001).

[186] A. Guinier, *X-Ray Diffraction: In Crystals, Imperfect Crystals, and Amorphous Bodies* (W.H. Freeman and Company, San Francisco, 1963).

[187] M. Zimmermann, A. Vigliante, T. Niemoller, N. Ichikawa, T. Frello, J. Madsen, P. Wochner, S. Uchida, N. H. Andersen, J. M. Tranquada, D. Gibbs, and J. R. Schneider, Europhysics Lett. **41**, 629 (1998).

[188] B. E. Warren, *X-Ray Diffraction* (Addison-Wesley Pub. Co., 1990).

[189] H. M. Rietveld, J. Appl. Crystallogr. **2**, 65 (1969).

[190] A. Le Bail, Powder Diffr. **20**, 316 (2005).

[191] A. P. Hammersley, S. O. Svensson, M. Hanfland, A. N. Fitch, and D. Hausermann, High Press. Res. **14**, 235 (1996).

[192] A. C. Larson and R. B. Von Dreele, *General Structure Analysis System (GSAS)* (2000), pp. 86–748.

[193] B. H. Toby, J. Appl. Crystallogr. **34**, 210 (2001).

[194] B. K. Teo, *EXAFS: Basic Principles and Data Analysis* (Springer-Verlag, 1986).

[195] P. Lee, P. Citrin, P. Eisenberger, and B. Kincaid, Rev. Mod. Phys. **53**, 769 (1981).

[196] J. J. Rehr and R. C. Albers, Rev. Mod. Phys. **72**, 621 (2000).

[197] A. L. Ankudinov, B. Ravel, J. J. Rehr, and S. D. Conradson, Phys. Rev. B **58**, 7565 (1998).

[198] D. Sayers, E. Stern, and F. Lytle, Phys. Rev. Lett. **27**, 1204 (1971).

[199] P. Lee and J. Pendry, Phys. Rev. B **11**, 2795 (1975).

[200] M. Baldini, W. Yang, G. Aquilanti, L. Zhang, Y. Ding, S. Pascarelli, and W. L. Mao, Phys. Rev. B **84**, 014111 (2011).

[201] J. Rehr and R. Albers, Phys. Rev. B **41**, 8139 (1990).

[202] A. L. Ankudinov, J. J. Rehr, and S. D. Conradson, Phys. Rev. B **58**, 7565 (1998).

[203] M. Newville, J. Synchrotron Radiat. **8**, 322 (2001).

[204] B. Ravel and M. Newville, J. Synchrotron Radiat. **12**, 537 (2005).

[205] Y. Joly, Phys. Rev. B **63**, 125120 (2001).

[206] P. Blaha, K. Schwarz, G. J. H. Madsen, D. Kvasnicka, and J. Luitz, *WIEN2k: An Augmented Plane Wave + Local Orbitals Program for Calculating Crystal Properties* (Techn. Universitat, Wien, Austria, 2001).

[207] J. M. Esteva, R. C. Karnatak, H. Dexpert, M. Gasgnier, P. E. Caro, and L. Albert, Le J. Phys. Colloq. **47**, C8 (1986).

[208] G. Kalkowski, G. Kaindl, G. Wortmann, D. Lentz, and S. Krause, Phys. Rev. B **37**, 1376 (1988).

[209] Z. Hu, E.-J. Cho, G. Kaindl, and B. Müller, Phys. Rev. B **51**, 7514 (1995).

[210] W. Bi, N. Souza-Neto, D. Haskel, G. Fabbris, E. Alp, J. Zhao, R. Hennig, M. Abd-Elmeguid, Y. Meng, R. McCallum, K. Dennis, and J. Schilling, Phys. Rev. B **85**, 1 (2012).

[211] F. de Groot, Chem. Rev. **101**, 1779 (2001).

[212] J.-P. Rueff, C.-C. Kao, V. Struzhkin, J. Badro, J. Shu, R. Hemley, and H. Mao, Phys. Rev. Lett. **82**, 3284 (1999).

[213] J. Badro, V. Struzhkin, J. Shu, R. Hemley, H. Mao, C. Kao, J.-P. Rueff, and G. Shen, Phys. Rev. Lett. **83**, 4101 (1999).

[214] M. Hücker, M. v. Zimmermann, M. Debessai, J. S. Schilling, J. M. Tranquada, and G. D. Gu, Phys. Rev. Lett. **104**, 057004 (2010).

[215] J. J. Rehr, Radiat. Phys. Chem. **75**, 1547 (2006).

[216] M. Crawford, R. Harlow, S. Deemyad, V. Tissen, J. Schilling, E. McCarron, S. Tozer, D. Cox, N. Ichikawa, S. Uchida, and Q. Huang, Phys. Rev. B **71**, 104513 (2005).

[217] W. Ting, K. Fossheim, and T. Lægreid, Solid State Commun. **80**, 47 (1991).

[218] B. Buchner, M. Breuer, A. Freimuth, and A. P. Kampf, Phys. Rev. Lett. **73**, 1841 (1994).

[219] J. Tranquada, G. Gu, M. Hücker, Q. Jie, H.-J. Kang, R. Klingeler, Q. Li, N. Tristan, J. Wen, G. Xu, Z. Xu, J. Zhou, and M. v. Zimmermann, Phys. Rev. B **78**, (2008).

[220] T. Park, V. A. Sidorov, F. Ronning, J.-X. Zhu, Y. Tokiwa, H. Lee, E. D. Bauer, R. Movshovich, J. L. Sarrao, and J. D. Thompson, Nature **456**, 366 (2008).

[221] H. Hua, V. K. Vohra, J. Akella, S. T. Weir, R. Ahuja, and B. Johansson, Rev. High Press. Sci. Technol. **7**, 233 (1998).

[222] D. Errandonea, R. Boehler, B. Schwager, and M. Mezouar, Phys. Rev. B **75**, 014103 (2007).

[223] W. Bi, J. Lim, G. Fabbris, J. Zhao, D. Haskel, E. E. Alp, and J. S. Schilling, *in preparation* (2014).

[224] F. H. Spedding, A. H. Daane, and K. W. Herrmann, Acta Crystallogr. **9**, 559 (1956).

[225] J. Hamlin, V. Tissen, and J. Schilling, Phys. Rev. B **73**, 094522 (2006).

[226] J. J. Hamlin, V. G. Tissen, and J. S. Schilling, Phys. C Supercond. **451**, 82 (2007).

[227] W. Grosshans and W. Holzapfel, Phys. Rev. B **45**, 5171 (1992).

[228] J. Wittig, Phys. Rev. Lett. **46**, 1431 (1981).

[229] J. Lim, G. Fabbris, D. Haskel, and J. S. Schilling, J. Phys. Conf. Ser. **500**, 192009 (2014).

[230] K. Takemura, N. Christensen, D. Novikov, K. Syassen, U. Schwarz, and M. Hanfland, Phys. Rev. B **61**, 14399 (2000).

[231] J. Perez-Mato, L. Elcoro, V. Petříček, H. Katzke, and P. Blaha, Phys. Rev. Lett. **99**, 025502 (2007).

[232] L. Parker, T. Atou, and J. Badding, Science **273**, 95 (1996).

[233] G. M. Stocks, G. D. Gaspari, and B. L. Gyorffy, J. Phys. F Met. Phys. **2**, L123 (1972).

[234] J. S. Schilling, High Press. Res. **26**, 145 (2006).

[235] U. Schwarz, O. Jepsen, and K. Syassen, Solid State Commun. **113**, 643 (2000).

[236] W. Hume-Rothery, J. Inst. Met. **35**, 319 (1926).

[237] N. F. Mott and H. Jones, *The Theory of the Properties of Metals and Alloys* (Oxford Univeristy Press, London, 1936).

[238] S. White and D. Scalapino, Phys. Rev. Lett. **80**, 1272 (1998).

[239] G. Ghiringhelli, M. Le Tacon, M. Minola, S. Blanco-Canosa, C. Mazzoli, N. B. Brookes, G. M. De Luca, A. Frano, D. G. Hawthorn, F. He, T. Loew, M. Moretti Sala, D. C. Peets, M. Salluzzo, E. Schierle, R. Sutarto, G. A. Sawatzky, E. Weschke, B. Keimer, and L. Braicovich, Science **337**, 821 (2012).

[240] N. Cunningham, N. Velisavljevic, and Y. Vohra, Phys. Rev. B **71**, 012108 (2005).

[241] K. Takemura and K. Syassen, J. Phys. F Met. Phys. **15**, 543 (1985).

[242] W. Bi, Y. Meng, R. S. Kumar, A. L. Cornelius, W. W. Tipton, R. G. Hennig, Y. Zhang, C. Chen, and J. S. Schilling, Phys. Rev. B **83**, 104106 (2011).

[243] R. Patterson, J. Appl. Phys. **95**, 5443 (2004).

[244] J. M. Montgomery, G. K. Samudrala, G. M. Tsoi, and Y. K. Vohra, J. Phys. Condens. Matter **23**, 155701 (2011).

[245] G. Chesnut and Y. Vohra, Phys. Rev. B **57**, 10221 (1998).